Guidance for time efficient path following of under-actuated differential thrust AUVs

Xue Jin

The University of Adelaide
South Australia 5005
Australia

A thesis submitted in fulfilment of the requirements for the degree of Master of Philosophy in Engineering on the 15th April 2016.

Summary

Autonomous Underwater Vehicles (AUVs) are relatively new underwater devices developed to execute missions in water without human operators. The advancements made in AUV technology have significant implications for a wide range of underwater applications. Guidance and control of AUVs plays an important role in many applications, and it is a challenging research topic, not only because of the significant nonlinearities and couplings in the AUV's dynamics, but the under-actuation found in typical AUVs.

This thesis presents new work contributing to time efficient path following of under-actuated AUVs. Different from the conventional fin-manoeuvred AUVs, the prototype vehicle considered in this thesis is a differential thrust manoeuvred AUV devoid of fins or rudders. Such a manoeuvring feature makes the vehicle very agile, but brings challenges in guidance and control.

A model of the prototype AUV is constructed based on the vehicle dynamics and manoeuvring features. In order to achieve time efficient path following, the AUV should operate at its motion limits. To derive the motion limits, a Monte Carlo analysis is conducted using the AUV model, which provides a numerical solution to derive the maximum admissible motion of the vehicle with respect to the curvatures along given paths. Thus, a curvature-based guidance system is developed. The strategy alters the AUV path following speed according to the path curvature, hence increasing the overall time efficiency. The effectiveness of the proposed method is demonstrated through simulations of the AUV following a range of different paths.

Declarations

The work presented in this thesis contains no material which has been accepted for the award of any other degree of diploma in any university or other tertiary institution. To the best of the author's knowledge and belief, this work contains no material previously published or written by another person, except where due reference has been made in the text.

I give consent to this copy of my thesis, when deposited in the University Library, being made available for loan and photocopying, subject to the provisions of the Copyright Act 1968.

I also give permission for the digital version of the thesis to be made available on the web, via the University's digital research repository, the Library catalogue, the Australasian Digital Theses Program (ADTP) and also through web search engines, unless permission has been granted by the University to restrict access for a period of time.

Xue Jin

Acknowledgements

First and foremost, I would like to thank my supervisors, Dr Steven Grainger and Professor Ben Cazzolato for their support and guidance. This thesis would never have been completed without their effort. I would also like to thank Associate Professor Colin Kestell for his time and input to this project. Not only the knowledge but also the experience I gained is an invaluable asset in my life.

In addition, I am grateful to all the staff in the School of Mechanical Engineering. In particular, I would like to express my gratitude to the head of school, Associate Professor Anthony Zander for his continuous support. Also I would like to thank Dr Lei Chen, Mr Gareth Bridges, Dr Zebb Prime and Dr Zhaofeng Tian for their advice on my study, and Miss Alison Jan-Hunter for her help in my thesis editing, as well as all the staff from the workshop who have assisted me with the experiments.

For all my friends and school mates, I will always remember and be thankful for their encouragement and help. In particular, I would like to thank Sophie Chen, Lancy Xie, Chenxi Li, Dr Boying Ding, Zahra Bagheri, Shi Zhao, Xiao Chen, Nikan Rostamzdeh and Erwin Hamminga, who have motivated and supported me during my difficult times.

I would also like to thank my partner, Dr Tao Zhu, for his endless encouragement, understanding and support during this long journey.

Finally, I would like to thank my parents, Xiaoying Chu and Wenxi Jin, for their unconditional love and trust. In every stage of my life, they have supported me in every way that a daughter can expect.

Contents

List of figures

List of tables

Nomenclature

AUV	Autonomous Underwater Vehicle
DOF	Degree of Freedom
CoG	Centre of Gravity
CoB	Centre of Buoyancy
G-frame $\{G\}$	Global frame
B-frame $\{B\}$	Body frame
SF-frame $\{SF\}$	Serret-Frenet frame
$[x \quad y \quad z]$	AUV position w.r.t. X, Y and Z - axis in G-frame
α	Angle of attack
β	Sideslip angle
ψ	AUV heading angle
χ	Course angle
$[\emptyset \quad \theta \quad \psi]$	AUV orientation angle w.r.t. X, Y and Z-axis in G-frame
$[p \quad q \quad r]$	Angular velocity w.r.t. X, Y and Z – axis in B-frame (roll, pitch and yaw)
$[\dot{x} \quad \dot{y} \quad \dot{z}]$	Velocity w.r.t. X, Y and Z - axis in G-frame
$[u \quad v \quad w]$	Velocity w.r.t. X, Y and Z - axis in B-frame
V	Total velocity
R	Radius of curvature
R_e	Reynolds number
C_D	Drag coefficient

C_L	Lift coefficient
D	Drag force
L	Lift force
C_r	Yaw resistance coefficient
$[M_x \quad M_y \quad M_z]$	Moments using differential thrust
$[M_p \quad M_q \quad M_r]$	Rolling, pitching and yawing drag moment
m	Mass
ρ	Fluid density
$[I_{xx} \quad I_{yy} \quad I_{zz}]$	Moment of inertia vector
T	Total (collective) thrust
ΔT	Differential thrust
$\boldsymbol{e}_p$	Deviation vector
Δ	Lookahead distance
K_P	Proportional gain of a PI controller
K_I	Integral gain of a PI controller
k_e	Modulation factor of the steering rate for convergence
MCA	Monte Carlo Analysis
GNC	Guidance, Navigation and Control
LOS	Line of sight
LTA	Line to arc transition
ATL	Arc to line transition

Chapter 1

Introduction

1.1 Background and motivation

Throughout human history, the exploration of the ocean has fascinated researchers and curiosity towards the underwater world motivates the development of ever more complex marine devices (Fossen, 1994). Meanwhile the advancements made in terms of the functionality and intelligence of these devices has significantly accelerated the process of exploration and exploitation of the unknown underwater world (Blidberg *et al.*, 2001). These underwater devices have shown their significance by contributing to a variety of tasks in many fields. Some of these applications are summarized as, but not limited to:

- Science applications
    - Monitoring and surveying (e.g. water quality, underwater biology etc.)
    - Mapping (e.g. terrain, geological features and underwater structures)
- Defence applications
    - Intelligence gathering and reconnaissance
    - Explosive placement

  - Retrieval of lost weapons
- Civilian, commercial and industrial applications
  - Installation, inspection and maintenance of underwater equipment (e.g. oil rigs, pipelines, cabling etc.)
  - Search and rescue (e.g. wreckage of missing ships or aircrafts)
  - Recovery and reparation (e.g. pipe leakage and tidal power/turbine station etc.)
  - Surveying (e.g. energy resources)

The underwater devices utilised in these applications can be categorized in many ways. A typical categorization is shown in Figure 1.1. It can be seen that the types of underwater devices can generally be broken down into manned and unmanned vehicles. Further down the categorization tree, the unmanned vehicles are divided into AUVs (Autonomous Underwater Vehicles) and ROVs (Remotely Operated Vehicles).

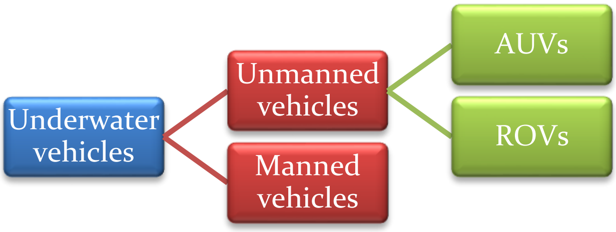

Figure 1.1: Underwater vehicles can be categorized according to their operation features (Based on Christ and Wernli, 2007).

ROVs are normally bulky in shape and equipped with robotic arms, such as the CURV II shown in Figure 1.2. Such designs allow ROVs to carry out underwater assignments involving complicated manipulations at low operating speed. For example in Figure 1.3, the ROV developed by Oceaneering (a world class manufacture of ROVs for the oil and gas industry) is carrying out connecting and repairing tasks on underwater pipelines. ROVs are normally tethered by umbilicals to the operator from shore, which results in limited operating range.

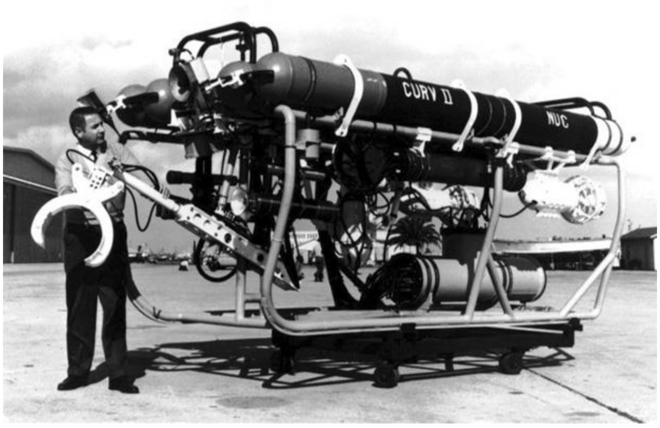

Figure 1.2: CURV II ROV (Christ and Wernli, 2007)

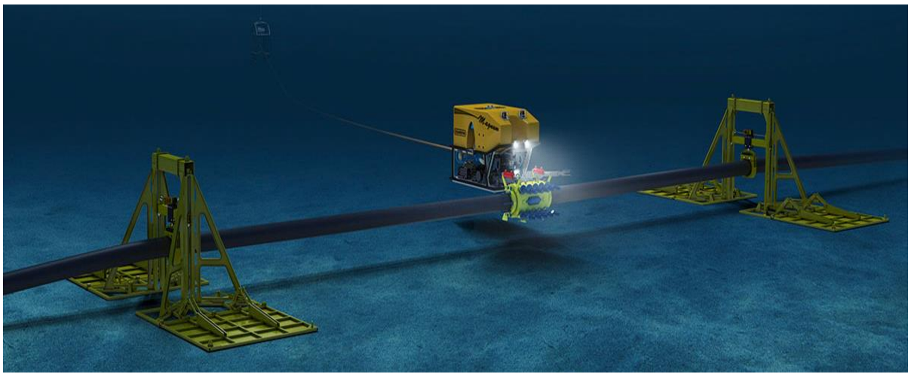

Figure 1.3: ROV undertaking tasks (Oceaneering, 2013). A ROV conducts connecting and repairing tasks on underwater pipelines.

Conventional AUVs are often more streamlined than ROVs in shape. For example, the REMUS 100, as shown in Figure 1.4, illustrates a conventional AUV design (WHOI). Such a torpedo shape is hydrodynamically efficient and therefore very commonly used in AUV designs. Compared with ROVs, AUVs are non-tethered, and commonly utilised in mapping, searching and surveying missions. During these missions, the AUVs are deployed to the required depth in the area and often follow a predefined path over the region. As demonstrated in Figure 1.5, several AUVs are set at different depths to scan the seafloor by following planar lawn mower search paths.

Figure 1.4: REMUS 100 AUV (WHOI, 2009). The vehicle is equipped with a rudder and stern planes for maneuvering, a vertical thruster for depth control and a propeller for speed control.

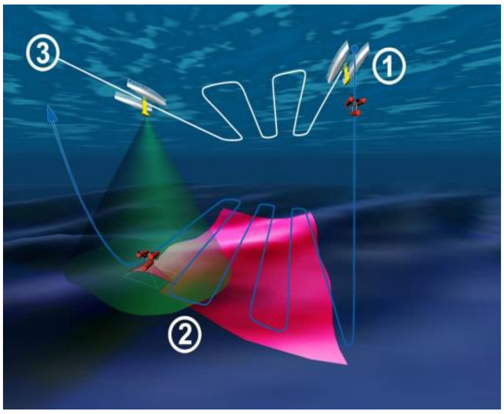

Figure 1.5: AUVs conducting underwater scanning (Sanz *et al.*, 2010). AUVs are sent to different depths to scan the sea floor using sonar and they are following a planar lawn mower path.

However, guidance and control is challenging for conventional AUVs as they are typically under-actuated. By definition, a system is termed under-actuated if the degrees of its actuations are less than its degrees of freedom (Aguiar and Pascoal, 2002; Kim, 2009). It can be seen from Figure 1.4 that the AUV alters its orientation in space by the deflection of its control surfaces (the rudder and stern planes), while the propeller in the aft pushes the vehicle forward. A vertical thruster is used for decoupled depth control. Being underactuated, the motion in the cross-body direction is constrained as there is no actuation. Another drawback for conventional fin-manoeuvred AUVs is that they can only carry out manoeuvres when the vehicle is in motion (Cavallo *et al.*, 2004). This is because the torque for manoeuvring only exists when there is relative motion between the control surfaces and the surrounding fluid.

In this research, a differential thrust AUV was developed by the University of Adelaide in 2008. As shown in Figure 1.6, the vehicle is similar in shape to most conventional AUVs. The torpedo-shaped pressure hull was manufactured as a one-piece cylindrical tube with two sealed end caps. The vehicle weighs 42 kg, is 1.1 m in length and 0.35 m in diameter.

Figure 1.6: Rendered CAD model of the prototype AUV. The vehicle is equipped with three bi-directional thrusters, which sit on three wing-profiled bases attached to the hull.

The vehicle is highly agile with the differential-thrust propulsion system. Compared to the conventional fin-manoeuvred AUVs with independent propulsion unit and control surfaces, the differential thrust can generate equivalent manoeuvrings to the control surfaces, but the vehicle is also underactuated in the cross body direction, like most AUVs, which results in a challenging guidance and control problem. Additionally, the differential thrust configuration results in coupling between the actuation saturation in translational and rotational motion. Intuitively, there will not be any differential thrust available for steering when the vehicle is operated on full thrust for propulsion. Between the propulsion and the moment, the maximum availability of one is dependent on the instantaneous value of the other.

This prototype AUV is developed to perform underwater searches and surveys, and a critical performance factor considered in these missions is time efficiency. This research aims to develop a solution for an under-actuated differential thrust AUV to follow arbitrary planar paths time efficiently.

1.2 Scope of this work

In response to the aforementioned challenges in AUV guidance and control system design, the scope of this research includes the following aspects:

1. **Derivation of AUV motion limits**

   Through studying the dynamics of the prototype under-actuated differential thrust AUV, the motion limits of the vehicle will be derived. The results will be used in the guidance system for the AUV to operate at its maximum speed, as well as to guarantee that the motion references generated are physically feasible.
2. **Development of a guidance law for time efficient path following on arbitrary paths**

   Once the motion limits of the AUV are determined, a guidance system will be developed to generate motion references for the AUV to traverse along arbitrary planar paths time efficiently. Also motion controllers will be developed to execute the motion commands from the guidance system.
3. **Evaluation of the proposed algorithm**

   The proposed guidance and control algorithm will be examined through simulations. The performance of the proposed algorithm will be discussed in detail, and the advantages of the proposed algorithm will be demonstrated by comparing with traditional path following strategies.

1.3 Thesis outline

The thesis is structured into seven chapters. This chapter has introduced the general background and motivation. Chapter 2 presents a review of the literature on different aspects of the research scope, based upon which the research gap will be clarified.

In Chapter 3, modelling of the prototype AUV is introduced in terms of the kinematics and the dynamics of the AUV. Due to the research focus, the model is simplified for planar motion through modification of the configuration of the differential thrust system. Nevertheless, the model contains all principle characteristics of an under-actuated differential thrust AUV and hydrodynamic features.

For the purpose of time efficient path following, analysis of the AUV motion limits is presented in Chapter 4. A Monte Carlo numerical analysis is performed, and its results highlight the relationship between the path curvature and the maximum admissible speed of the AUV.

Based on the motion analysis, a curvature-based guidance algorithm is proposed in Chapter 5, where the methodology of the guidance and control is presented in detail.

To demonstrate the performance of the proposed path following algorithm, simulations using the AUV model are performed and results are presented in Chapter 6. Lastly, the conclusions and proposals for future work are introduced in Chapter 7.

1.4 Publication

There is one conference paper (in Appendix E) arising from the research work presented in this thesis based on the modelling of the prototype AUV:

X. Jin, C. Kestell, S. Grainger, G. Bridges "Agile Motion of a Differential Thrust Autonomous Underwater Vehicle", In: *ICMT International Conference of Mechatronics Technology, Melbourne, 2011.*

Chapter 2

Literature review

This chapter presents a literature review based on the research scope. Due to the variations in the terminologies in the existing literature, those used in this thesis and their definitions are also clarified in this chapter. The literature review covers the following aspects:

- **Fundamentals of under-actuated underwater vehicles**
  Fundamentals of conventional AUVs, differential thrust ROVs and the prototype AUV will be introduced, highlighting the significance and challenges in guidance and control of under-actuated AUVs.
- **Review of AUV modelling**
  AUV modelling is commonly used for guidance and control development as it allows the performance of the AUV to be predicted and evaluated through simulations. AUV modelling will be reviewed in this section.
- **Guidance and control fundamentals**
  In regard to the guidance and control of the AUV, fundamentals will be introduced, including the hierarchy of a typical motion control system and the role of each key component.

- **Review of guidance techniques**

  As for the research focus, existing guidance techniques will be reviewed, providing a foundation for the proposed methodology.

2.1 Under-actuated AUV fundamentals

Most AUVs are designed to be under-actuated, motivated by the need for cost and weight reductions (Aguiar and Pascoal, 2002; Kim, 2009). As mentioned in Chapter 1, conventional fin-manoeuvred AUVs are equipped with a rudder and stern planes for manoeuvring and a propulsion unit (propeller) at the aft of the vehicle for speed control. A top view of the actuation system of a fin-manoeuvred AUV is shown in Figure 2.1.

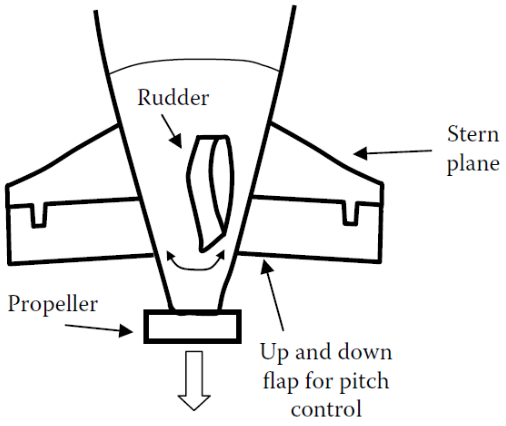

Figure 2.1: A detailed view of the main control surfaces and propeller. The system includes a rudder and stern planes for AUV maneuvering, as well as the propulsion unit (Wadoo and Kachroo, 2011).

The main challenges of under-actuated systems are due to their nonholonomic nature. A system is nonholonomic if its kinematic constraints cannot be integrated into geometric constraints. The kinematic constraints limit the motion and the geometric constraints refer to the limitations on position resulting in a reduction of the degrees of freedom of a system (Bloch, 2003). For example, fin-manoeuvred AUVs have no direct control in the cross-body direction, resulting in a kinematic constraint. The position of the vehicle in space is not constrained but the path to achieve the target position is limited. As fin-manoeuvred AUVs can only carry out manoeuvrings in motion, they often have limited manoeuvrability. As a result, there are constraints on the path to be followed (Antonelli *et al.*, 2008). As illustrated in Figure 2.2, fin-manoeuvred AUVs cannot follow the path exactly if the path has sharp corners (shown by the black solid lines). The possible resultant paths are represented by the blue dotted curve and red dash curve, with large turning radius. In addition to paths with sharp corners, conventional fin-manoeuvred AUVs are also incapable of following paths with arc sections smaller than the minimum turning radius of the vehicle without significant deviations.

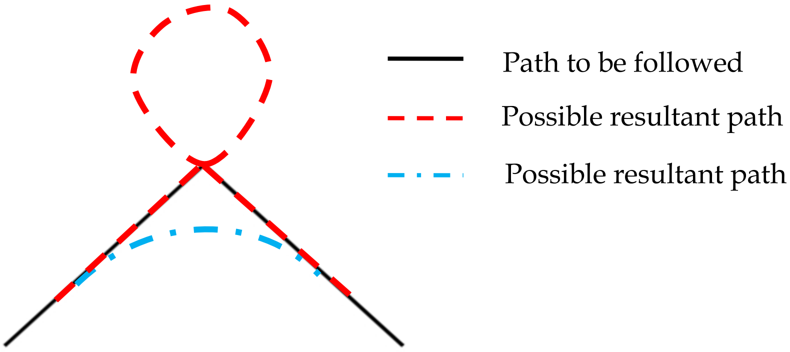

Figure 2.2: Possible resultant paths when conventional fin-manoeuvred AUVs follow a path with a sharp corner. The path to be followed is in black, the blue dotted and red dash curves are the possible resultant paths.

Differential thrust can enhance the agility of underwater vehicles and effective manoeuvrings at both high and low speeds, and even when stationary, therefore it has been used in most ROVs. For example, as shown in Figure 2.3, the micro ROV VideoRay Pro III, is equipped with three thrusters: two of which are horizontally orientated and the other sits vertically on the top of the vehicle. By applying differential thrust, the vehicle can be steered on the horizontal plane, while its motion on the vertical plane is decoupled and controlled by the vertical thruster (Wang, 2007).

Figure 2.3: Micro ROV – VideoRay Pro III (Wang, 2007). The micro tethered ROV has two horizontal thrusters and a vertical thruster.

The prototype AUV used in this research is manoeuvred by a differential thrust system. As demonstrated in Figure 2.4, it is manoeuvred using three bi-directional thrusters. The three thrusters are denoted respectively as T_1, T_2 and T_3.

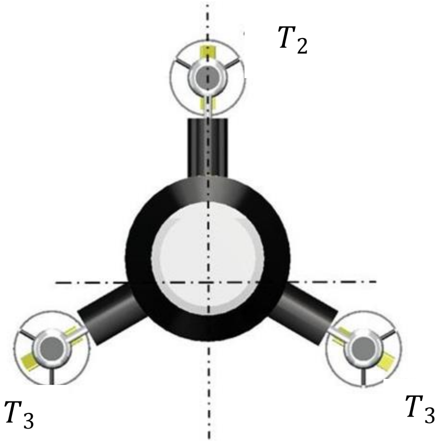

Figure 2.4: Frontal view of the prototype AUV. The differential-thrust propulsion system consists of three thrusters located 120 degrees apart.

During searching or mapping, AUVs are deployed to the required depth and guided to follow a predefined path. To simplify the couplings in control, AUVs often separate the depth control from the planar motion control (Antonelli *et al.,* 2008). Effective following of planar paths by an under-actuated differential thrust AUV remains an open research topic.

2.2 Review of AUV modelling

Modelling and simulation of AUVs is recognized as a cost and time efficient method when compared with the alternatives such as experiments, not to mention its advantages in eliminating the risks of losing the vehicles (Chen *et al.,* 2013). To conduct effective simulations, the mathematical models used in the simulations need to be sufficiently accurate. Models developed at the kinematic level are more limited than those incorporating AUV dynamics; however, a full dynamic model is extremely challenging due to the significant nonlinearities in the hydrodynamics (Caldwell, 2011). Also, none of the existing AUV models fit all vehicles and there is no standard modelling procedure. Each AUV model represents a new problem (Evans and Nohan, 2004). An AUV is a complex system consisting of many subsystems. Detailed modelling of every component is complicated and not always necessary for all research, therefore simplifications are made to retain the critical characteristics required for different missions. For example, the dynamics of the thrusters is modelled as a constant thrust and torque source for the REMUS AUV (Prestero, 2001).

The motion of an AUV is heavily reliant on hydrodynamics as it characterizes the external forces on the vehicle (Evans, 2003). The hydrodynamic coefficients in an AUV model can be derived by a range of analytical, experimental and computational methods, as well as combinations thereof (Chen *et al.,* 2013).

Experiments can be used in both modelling and system identification. The system identification method is data-based and the experiments provide a number of input-output data to estimate the dynamics of the given system for an implicit expression of the AUV model. Generally, the data from experiments contains disturbances/noise in underwater environments. Moreover, the data needs to be sufficiently large in size and range to capture the system performance in all aspects, which is often impractical (Ostafichuk, 1997). Hence the reliability of the implicit model developed through system identification cannot be guaranteed. On the other hand, experiments are performed to derive and validate the AUV parameters. The derivation of a full model is relatively costly due to the facilities required and operational costs; therefore it is usually used for validations of the model parameters, estimated by other methods.

Computational methods are suitable for AUVs with simple configurations, or when experimental facilities are not available. For example, Computational Fluid Dynamics (CFD), is a predictive method based on the vehicle geometry, and the modelling accuracy degrades with increasing geometric complexity. Moreover, computational methods can be extremely time consuming requiring significant computational effort and modelling experience. Even for simple geometric bodies, the dynamics problem of the surrounding fluid itself is complicated and very demanding in terms of computational effort (Evans, 2003).

In practice, analytical methods are popular, using fundamental first principles to derive the hydrodynamic coefficients (Solberg, 1992). The estimations of the hydrodynamics are based on popular shapes and most shapes are simplified to a basic form, such as airfoil and torpedo shapes. AUVs can be treated as streamlined bodies and many empirical formulas have been derived to estimate the hydrodynamic coefficients (Geisbert, 2007). Some are based on the small angle assumption, where the operational angle range is constrained within ±12 degrees (Nohan, 1996). The small angle assumption is valid for conventional fin-manoeuvred AUVs as their actuation feature limits the vehicles to small angle of attack.

The hydrodynamics model can be significantly simplified as the coefficients used in the model are constants.

In fact, these coefficients are nonlinear and vary with respect to the operation angle, which has been addressed in some AUV models. Jorgensen (1973) investigated the hydrodynamics of submersibles with a high aspect ratio (calculated as the length over diameter) and derived formulas for axial and normal coefficients. These coefficients can be used to calculate the forces in the body axial and perpendicular directions. In addition, the analytical methods are often used in conjunction with the experimental methods for more reliable results. Jorgensen's formulas were adopted and extended by Evans and Nahon (2004) for modelling the dynamics of the C-SCOUT AUV. In Evans' model (2004), the forces parallel and normal to the hull of the AUV were determined using the formulas, which were justified by comparison with the experiment results. On the other hand, Allen and Perkins (1951) presented theoretical formulas to calculate drag and lift coefficients for a streamlined body instead of the axial and normal coefficients. These formulas were verified empirically and proved to be an effective analytical solution to calculate the drag and lift forces for given speeds and angle of attack/sideslip angle.

Overall, a combination of the analytical and experimental method is efficient for the development of guidance and control systems (Prestero, 2001). As will be presented in Chapter 3, Allen and Perkins' formulas are chosen to determine the hydrodynamic coefficients, which are then verified using experimental data. Simulations are performed to evaluate the AUV model.

2.3 Guidance and control fundamentals

A complete AUV motion control system consists of three key components, which are Guidance (**G**), Navigation (**N**) and Control (**C**), known as a

GNC system (Antonelli *et al.*, 2008). The definitions of the three components adopted in this thesis are:

'**G**': Guidance encompasses the process of determining the path/trajectory, orientation and speed to be followed by the vehicle.

'**N**': The navigation system provides information regarding the current location and the target position of the vehicle, sometimes the velocity and acceleration as well.

'**C**': Control determines actions/actuations (forces and moments) necessary to ensure the system behaves as it is instructed. It executes based on the commands produced and passed from the guidance system and the feedback from the navigation system.

The relationship among the three components of a GNC system is illustrated by a block diagram in Figure 2.5.

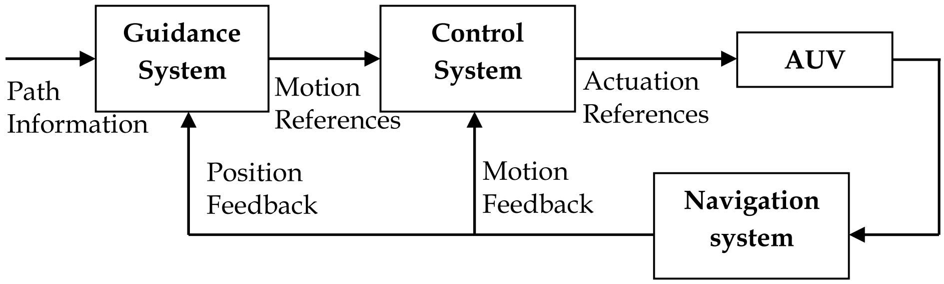

Figure 2.5: Block diagram of a Guidance, Navigation and Control (GNC) system.

Navigation is not the research focus here but is outlined to demonstrate a complete GNC system. Guidance and control are separated in such an inner – outer loop motion control system. Alternatively, an integrated form is used in some cases, where the guidance and control are designed simultaneously and many nonlinear control laws have been developed in the literature. Nonlinear controllers are capable of dealing with systems with nonlinear dynamics, such as sliding mode, adaptive and H-infinity controllers, as well as Lyapunov based control methods (Antonelli 2007, Healey and Lienard, 1993, Jiang and Nijmeijer, 1997, Kaminer *et al*., 1998, Lapierre and Jouvencel, 2008). Some relatively new control methods, such as neural networks and fuzzy logic, have also been applied to AUVs (Shi *et al*., 2006). These methods require little knowledge about the system dynamics but their reliability cannot be guaranteed (Lea *et al*., 1999).

In comparison with the integrated design, the separate structure is preferred in most applications due to its simplicity (Park *et al*., 2004). Linear controllers (such as PID controllers) can be used for the inner control loop. Compared with the nonlinear controllers, PID controllers are much simpler and hence have been commonly used for industrial applications for a wide range of robotic systems including ground, aerial and marine vehicles with satisfactory performance (Park *et al*., 2004).

Therefore, the research presented in this thesis adopted the separate structure due to the research focus on the guidance algorithm development in the outer loop. An intelligent guidance system is desirable to make the most appropriate decisions for the system, and guidance strategies are dependent on different mission goals (Naeem, 2004). Those aiming for obstacle avoidance would have different guidance laws from those focusing on reducing fuel consumption. For the research problem of following a given planar path, a review of existing guidance algorithms is presented in the subsequent section.

2.4 Review of AUV guidance techniques

The motion control problem of following a predefined planar path can be generally categorized according to the following objectives: trajectory tracking, path following and path manoeuvring (Fossen, 1994).

Trajectory tracking focuses on tracking target position with temporal constraints – arriving at a certain position at a certain time. A planar path can be seen as a manifold of reference positions (waypoints). In Figure 2.6, waypoints are represented by the black dots.

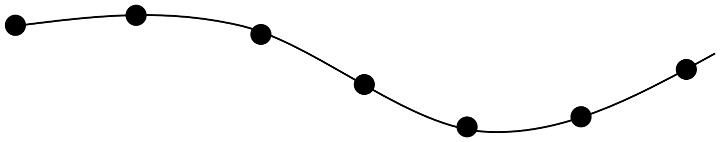

Figure 2.6: Diagram of waypoints along a path. The waypoints (black dots) are the reference positions on the path (solid curve).

A path consisting of n waypoints can be represented by locations in earth coordinates (Skjetne, 2005),

$$\{\boldsymbol{p}_i \in \mathbb{R}^2,\ i = 1, \cdots, n\}. \tag{2.1}$$

For trajectory tracking, the reference positions on a planar path can be parameterized in relation to time as

$$\boldsymbol{p}(t) = [x(t), y(t)]. \tag{2.2}$$

The guidance laws generate motion references to track these waypoints along the path, which are

$$V(t) = \sqrt{\dot{x}(t)^2 + \dot{y}(t)^2}, \tag{2.3}$$

$$\chi(t) = \operatorname{atan2}(\dot{y}(t), \dot{x}(t)), \tag{2.4}$$

where motion references, the velocity V and course angle χ, are both functions of time (Breivik, 2010). The function atan2 is used so that

$$-\pi \leq \chi(t) = \operatorname{atan2}(\dot{y}(t), \dot{x}(t)) \leq \pi. \tag{2.5}$$

Trajectory tracking has shown its value in a variety of applications, however not only spatial constraints (to track the waypoints), but also the temporal constraints (arrive at waypoints on planned time) need to be satisfied. Such temporal constraints are not always necessary in following a given path and the tracking performance can be degraded significantly once the vehicle is unable to physically manage the commanded motions.

This is considered a challenge for under-actuated AUVs, where motion in some directions is constrained (Skjetne, 2005).

In contrast, path following is less restrictive as it removes the temporal constraints and focuses on following and converging to the given path. Therefore, it is considered a more flexible and robust option than trajectory tracking (Breivik and Fossen, 2005).

For path following, the path to be followed is parameterized by the reference positions (waypoints) with respect to a scalar variable θ instead of time:

$$\boldsymbol{p}(\theta) = [x(\theta), y(\theta)]. \tag{2.6}$$

These functions of the reference positions can be represented by polynomials,

$$\begin{cases} x_i = a_{k,i}\theta^k + a_{k-1,i}\theta^{k-1} + \cdots + a_{1,i}\theta^1 + a_{0,i} \\ y_i = b_{k,i}\theta^k + b_{k-1,i}\theta^{k-1} + \cdots + b_{1,i}\theta^1 + b_{0,i}, \end{cases} \tag{2.7}$$

where (x_i, y_i) is the position of the i-th waypoint. When the path is parameterized as polynomials, the order of the polynomials k represents the path continuity, specifically geometric continuity. An introduction to path continuity can be found in Appendix D. Path continuity is an important path property and has a significant role in path following. As will be discussed later in this section, some guidance algorithms were developed based on the assumption that the paths are at least two times differentiable.

A common guidance strategy for path following is to assign a constant speed for the system to follow and to develop a steering law, which generates reference directions for the vehicle to converge or remain on the path (Do *et al.,* 2004; Lapierre *et al.,* 2008; Breivik, 2010).

There are a variety of steering laws available in the literature. The Line of Sight (LOS) guidance scheme is the most widely used method, which was initially developed for missile applications (Fossen *et al.,* 2015). By definition, the line-of-sight is a vector that points from a fixed reference position to the target way-point. The steering law is based on three points: the actual position of the vehicle, a target and a reference position. In Figure 2.7, these positions are represented by the red markers.

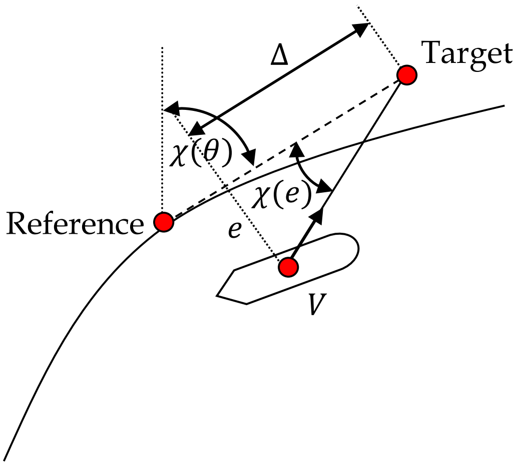

Figure 2.7: Schematic of the LOS guidance principle. The algorithm is based on three positions represented by the red dots. The reference position is on the path, and a tangential line of the path at the reference point is represented by the dashed line. The cross-track error e is the distance from the actual vehicle position to its projection on the path tangential line. The target position is determined relative to the projection position at a chosen lookahead distance Δ along the path tangential direction. $\chi(\theta)$ represents the angle of the path tangential line, and $\chi(e)$ is the relative angle between the velocity and path.

As shown in Figure 2.7, the reference position on the path can be represented by Equation (2.6). The direction of the path can be found by constructing a tangential line of the path through this reference position, which can be calculated by the differentiation of the reference position with respect to the path variable θ as

$$\chi(\theta) = \text{atan2}(y(\theta)', x(\theta)'). \tag{2.8}$$

The direction of the velocity of the AUV relative to the path is represented by $\chi(e)$, which can be calculated as

$$\chi(e) = \mathrm{atan2}(e, \Delta), \tag{2.9}$$

where e is the distance from the actual vehicle position to the path tangential line – describing the deviation of the AUV, and Δ is the lookahead distance from the AUV projection on the path tangential line to the target position. The lookahead distance Δ is a constant, and hence the larger e is, the larger the deviation is, the larger angle the AUV needs to steer towards the path for convergence.

The steering law is to determine the course angle (angle of the velocity in the global coordinate system). The course angle can be calculated as

$$\chi(\theta, e) = \chi(\theta) + \chi(e). \tag{2.10}$$

Such a steering law ensures that the velocity is directed to the target therefore the AUV will converge to the path.

However, constant speed path following focuses on the geometric constraint with no concern for time efficiency. For many applications including racing cars and profiling robotic arms, the system is desired to move along a path as fast as possible, which is defined as a path manoeuvring problem (Breivik, 2010).

Path manoeuvring represents a special form of path following, which can be divided into geometric and dynamic tasks. The geometric task is to develop steering laws to converge and stay on the path, while the focus of the dynamic task is to assign the speed for traversing along the path (Breivik, 2010). For the purpose of time efficient path following, the speed is desired to be as large as possible without necessitating significant deviation from the path.

There have been many time optimal path following algorithms proposed for robotic manipulators (Shin and McKay, 1985; Bobrow *et al.*, 1985; Lam, 2012). In these works, the speed reference for following a path was determined within a feasible region. The region is constructed using the speed limit - the maximum speed along the path. The speed limit was derived from the system dynamics subject to the path geometric constraints. However, the dynamics of the end point of the robotic manipulator only include translational motion. Neither the rotational motion nor the coupling between the translational and rotational motion is involved. Additionally, the manipulator is fully actuated in all directions of interest and the motion constraints of an under-actuated system were not considered. For under-actuated systems, the curvature along the path is critical in determining the reference speed (Velenis *et al.*, 2005). For example, for an under-actuated land vehicle with no direct actuation in the cross body direction, the centripetal force required for following a curved path can only be sourced from the friction force between the tyre and road. A free body diagram of the tyre during a turn is illustrated in Figure 2.8.

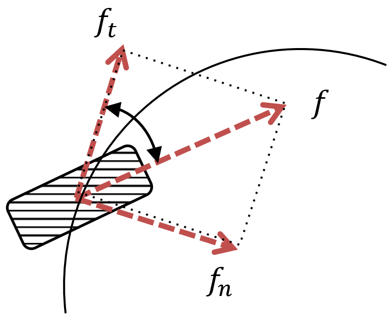

Figure 2.8: Free body diagram of a tyre during a turn. The wheel/tyre turns at an angle to the path and the total friction force f can be resolved into two components in the path tangential and normal directions, represented by f_t and f_n.

As shown, when the vehicle is manoeuvring around a curve (the solid curve), the tyre is steered at an angle relative to the path, so the total friction force f can be resolved into two components, f_t and f_n in the path tangential and normal directions. The normal component f_n provides the centripetal force required for the turn. The maximum centripetal force available is limited by the maximum friction force between the ground and tyre. Therefore the greater the curvature of the path, the lower the traversing speed the vehicle can manage. From heuristic driving behaviour, drivers slow down the vehicle when the curvature of the path increases. The curvature constraints on the motion also apply to marine vehicles and have been considered in some guidance algorithms.

In 2009, Bibuli *et al*. developed a heuristic speed adaption algorithm for a surface vessel to adjust the speed reference command according to the curvature along the given path k. Figure 2.9 illustrates the architecture of the motion control system.

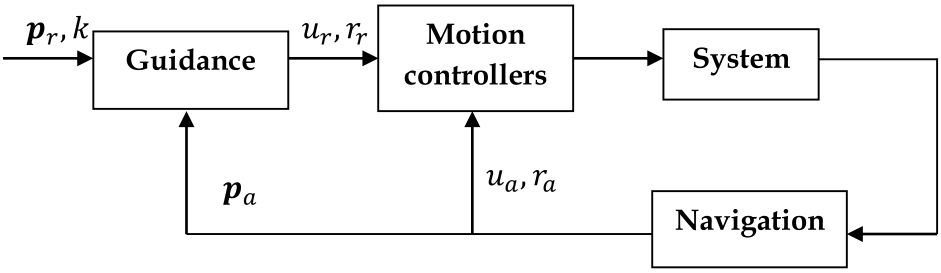

Figure 2.9: Architecture of the motion control system with speed adaption algorithm. This is an inner-outer loop structure, the guidance generates speed commands u_r, r_r according to the position error between the actual $\boldsymbol{p}_a$ and reference $\boldsymbol{p}_r$ position, as well as the curvature k. (Based on Bibuli *et al*., 2009)

As shown, the guidance in the outer loop determines speed and yaw rate references (u_r, r_r) to compensate the position error (deviation), and the inner control loop compensates the errors between the actual (u_a, r_a) and commanded motion. It was demonstrated that the actual vessel exhibits a large turning radius, even sliding away from the path for sharp curves, when operating at constant speed. The speed adaption reduces the speed when the actual heading of the vehicle is significantly different from the target heading, for example, when the vehicle is approaching a curve from a straight section on the path (Bibuli *et al*., 2009). The guidance law though, is developed at the kinematic level only, and thus the feasibility of the commanded reference cannot be guaranteed when not considering the system dynamics.

In 2010, Haugen developed a LOS based guidance algorithm for planar path-based motion control, employing the dynamics constraints of a surface vessel. As illustrated in Figure 2.10, the guidance consists of a speed assignment law to traverse along the path, and a steering algorithm for path convergence.

Figure 2.10: Diagram of a guidance system for path following. The traversing law determines the speed while steering is determined by the convergence law.

For path traversing, the reference speed is determined within a selected lookahead distance Δ according to the current and target position, the LOS parameters are given in Figure 2.7. The course angle is decided based on a LOS method. Simulations were performed to verify the method for different paths including a straight path, a circular path, a curved path and a lawn mower path. However, as Haugen stated in his work, assumptions made to simplify the model dynamics were not realistic - the acceleration limits in lateral direction were neglected in the model. Also in the case of following the lawn mower path, constant speed was used and it was pointed out that the speed needs further optimization. Moreover, the guidance method is limited by the path continuity. This is due to the fact that the guidance system generates motion references by taking the derivatives of the path like many other guidance laws, as demonstrated in Equation (2.8). Let the path variable θ be time, the first derivative of the path represents the speed and the second derivative is the acceleration. Therefore, a common assumption applied for existing guidance systems is that the given path needs to be at least two times differentiable (Repoulias, 2007). In other words, paths to be followed must be curvature continuous (Tsourdos *et al.,* 2011). In this case, lawn mower paths are considered "infeasible" due to the curvature discontinuities at the intersections between the straight lines and the U-turn (arc segment). As will be demonstrated in Appendix D, the lawn mower path needs to be modified into a curvature continuous path otherwise the guidance algorithm developed cannot be applied (Haugen, 2010).

2.5 Summary and research objectives

In summary, the guidance and control of the under-actuated AUV is still an open research topic despite the considerable progress made in previous work. None of the work reviewed above has considered the time efficient path following of under-actuated differential thrust AUVs. Although many guidance algorithms have been developed for AUV path following, most focus on the convergence to reference paths by guiding the vehicle with constant traversing speed. Therefore these methods are conservative in terms of the time efficiency for applications aiming for fast path traversing. In addition, there have been time efficient path following methods developed for different robotic systems (such as robotic arms and land vehicles), however, they are often limited to paths with certain continuity - the path needs to be at least twice differentiable (Repoulias, 2007). Paths with curvature discontinuities (such as the lawn mower paths – a common search path pattern), are considered not "followable" without path modifications. Moreover, many guidance methods are developed with regard to kinematics, with no concern for the system dynamics. Consequently, the path following performance can be significantly degraded when commands generated by the guidance system are physically impossible for the AUV.

The limitations of the existing guidance algorithms signify the need for a guidance method for under-actuated differential thrust AUVs to follow arbitrary paths (including curvature discontinuous ones) efficiently with respect to time. In order to achieve this, a new guidance solution is proposed to assign motion references for following arbitrary predefined planar paths using the motion limit of the AUV. The motion limit indicates the physical limit of the AUV based on the dynamics and the path curvature. As will be demonstrated in Chapter 4, a numerical method is applied in this thesis to derive the motion limits of the prototype AUV.

For the development of the proposed guidance method, a new model based on the prototype AUV will be established as a different model is needed for each different AUV (Evans and Nohan, 2004). As there is no standard modelling procedure, a combination of analytical and experimental approaches are used to derive a valid model. Moreover, the model presented in Chapter 3 is simplified for planar motion (the focus of this research), but retains the hydrodynamics and the actuation features of the differential thrust drive.

Chapter 3

AUV modelling

In this chapter, the AUV modelling will be presented in terms of the kinematics and dynamics respectively. The model is based on the prototype AUV and the original prototype AUV configuration is subsequently modified for planar motion. Hydrodynamics coefficients used in the model are derived analytically, and are compared with the experimental results for validation. The complete Simulink model is validated through simulations.

3.1 Modelling of the prototype AUV

Modelling of the prototype AUV involves both kinematics and dynamics. The AUV kinematics focuses purely on the motion of the AUV without considering the driving mechanism behind the motion, whereas the dynamics addresses the forces and moments on the AUV.

3.1.1 AUV kinematics model

The kinematics of the AUV involve three coordinate systems, namely the global frame (G-frame), body frame (B-frame) and Serret-Frenet frame (SF-frame). The three coordinates are illustrated in Figure 3.1, where the reference frames are shown as solid lines and the blue dashed line represents the path of the AUV. The acronyms of the three frames are used in this figure, $\{G\}$ for the G-frame, $\{B\}$ for the B-frame, and $\{SF\}$ for the SF-frame. In the following subsections, details of the three coordinate systems and the kinematics of the AUV are introduced.

3.1.1.1 Global frame (G-frame)

The global frame is commonly known as the earth-fixed coordinate system, and it has frequently been used for positioning applications, such as vehicle navigation.

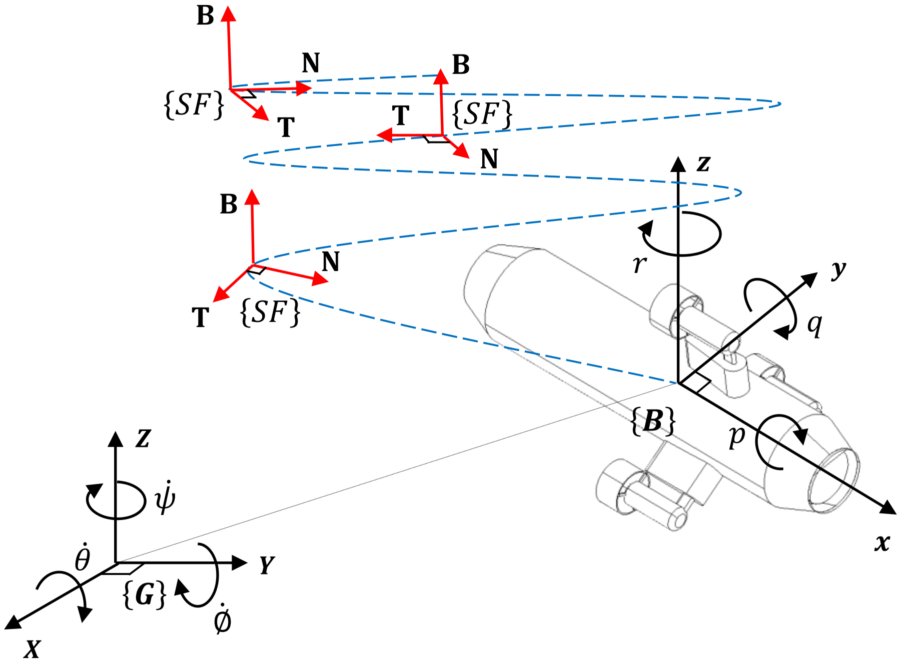

Figure 3.1: The G-frame $\{G\}$, the B-frame $\{B\}$ and the SF-frame $\{SF\}$. The AUV and its path (the blue dotted curve) are illustrated. The Serret-Frenet coordinate system in red evolves along the curved path in 3-Dimensional space. Rotational motion of the AUV with respect of the three axes of the G-frame and B-frame.

As shown in Figure 3.1, the G-frame consists of three axes, the global X, Y and Z axes. The AUV motions about these axes, including both translational and rotational motions, are summarized in Table 3.1. In Figure 3.1, the rotational motion with respect to the three axes of the G-frame and B-frame are respectively illustrated.

Table 3.1: AUV motions in G-frame, which include the position and orientation, and the translational and rotational velocity of the vehicle

Translational motion	
$[x, y, z]^T$	Position/coordinates of the vehicle
$[\dot{x}, \dot{y}, \dot{z}]^T$	Translational velocity of the vehicle
Rotational motion	
$\emptyset, \theta, \psi]^T$	Orientation of the vehicle
$[\dot{\emptyset}, \dot{\theta}, \dot{\psi}]^T$	Angular velocity of the vehicle

3.1.1.2 Body frame (B-frame)

The body coordinate systems are often used to describe the AUV motions within a three dimensional configuration space. Generally, there are six independent motions, respectively named as surge, sway, heave, yaw, pitch and roll (Fossen, 1995). Descriptions of each and the motion vectors for the body frame are summarised in Table 3.2.

Table 3.2: AUV motions in B-frame and their description

Motion (velocity) Vectors	Motion	Description (in B-frame)
$\begin{bmatrix} u \\ v \\ w \end{bmatrix}$	Surge	Translational motion along the *x*-axis
	Sway	Translational motion along the *y*-axis
	Heave	Translational motion along the *z*-axis
$\begin{bmatrix} p \\ q \\ r \end{bmatrix}$	Roll	Rotational motion around the *x*-axis
	Pitch	Rotational motion around the *y*-axis
	Yaw	Rotational motion around the *z*-axis

3.1.1.3 Serret-Frenet frame (SF-frame)

The SF-frame is a coordinate system that is directly associated with the path and motion of the AUV. It has three axes, denoted respectively as the *T*-axis, *N*-axis and *B*-axis, as indicated in Figure 3.1. The *T*-axis is tangential to the path pointing in the direction of motion, represented by the tangential unit vector $\mathbf{T}$. The *N*-axis is normal to the path and represented by unit vector **N**. The *B*-axis is in the direction defined by a bi-normal unit vector $\mathbf{B}$, which is the cross product of $\mathbf{T}$ and $\mathbf{N}$ as expressed as

$$\mathbf{B} = \mathbf{T} \times \mathbf{N}\,. \tag{3.1}$$

Additionally, the SF-frame is also known as the tangential-normal coordinate system for 2D/planar motions. It has been used for the control of a mobile robot and the path following of ships (Samson, 1995; Skjetne and Fossen, 2001; Do and Pan, 2004), and in this case it was adopted to guide the AUV to follow predefined paths.

The SF-frame is also tightly related to the vehicle hydrodynamics, since the angle of attack, α, and sideslip angle, β, are determined by the angles between the vector **T** and the direction that the vehicle is heading. A graphical explanation of these two angles is given in Figure 3.4.

3.1.1.4 Kinematics model

In the AUV model, the real time states of the system are expressed in the G-frame, whereas the actuations are in the B-frame, and the angles to determine the hydrodynamics is associated with the SF-frame. Therefore, a transformation matrix is used to transform the AUV motion from the B-frame to the G-frame, and vice versa. The transformation matrix for the translational and rotational motions is (Fossen, 1994):

$$\boldsymbol{J} = \begin{bmatrix} \mathrm{c}\varphi\,\mathrm{c}\theta & -\mathrm{s}\varphi\,\mathrm{c}\emptyset + \mathrm{c}\varphi\,\mathrm{s}\theta\,\mathrm{s}\emptyset & \mathrm{s}\varphi\,\mathrm{s}\emptyset + \mathrm{c}\varphi\,\mathrm{s}\theta\,\mathrm{c}\emptyset & 0 & 0 & 0 \\ \mathrm{s}\varphi\,\mathrm{c}\theta & \mathrm{c}\varphi\,\mathrm{c}\emptyset + \mathrm{s}\varphi\,\mathrm{s}\theta\,\mathrm{s}\emptyset & -\mathrm{c}\varphi\,\mathrm{s}\emptyset + \mathrm{s}\varphi\,\mathrm{s}\theta\,\mathrm{c}\emptyset & 0 & 0 & 0 \\ -\mathrm{s}\theta & \mathrm{c}\theta\,\mathrm{s}\emptyset & \mathrm{c}\theta\,\mathrm{c}\emptyset & 0 & 0 & 0 \\ 0 & 0 & 0 & 1 & \mathrm{s}\emptyset\,\mathrm{t}\theta & \mathrm{c}\emptyset\,\mathrm{t}\theta \\ 0 & 0 & 0 & 0 & \mathrm{c}\emptyset & -\mathrm{s}\emptyset \\ 0 & 0 & 0 & 0 & \frac{\mathrm{s}\emptyset}{\mathrm{c}\theta} & \frac{\mathrm{c}\emptyset}{\mathrm{c}\theta} \end{bmatrix}, \tag{3.2}$$

where s, c and t are acronyms of $\sin(\cdot)$, $\cos(\cdot)$ and $\tan(\cdot)$ respectively.

Therefore the translational and rotational motions in the B-frame are

$$\begin{bmatrix} u \\ v \\ w \\ p \\ q \\ r \end{bmatrix} = \boldsymbol{J} \begin{bmatrix} \dot{x} \\ \dot{y} \\ \dot{z} \\ \dot{\emptyset} \\ \dot{\theta} \\ \dot{\psi} \end{bmatrix}. \tag{3.3}$$

The total velocity of the vehicle is

$$V = \sqrt{u^2 + v^2 + w^2} = \sqrt{\dot{x}^2 + \dot{y}^2 + \dot{z}^2}\,. \tag{3.4}$$

The angle of attack α and sideslip angle β can be derived as

$$\begin{aligned} \alpha &= \tan^{-1}\frac{w}{u}, \\ \beta &= \tan^{-1}\frac{v}{u}. \end{aligned} \tag{3.5}$$

Based on the kinematics model, a dynamics model will be discussed in the subsequent section.

3.1.2 AUV dynamics model

Dynamics modelling is essential for planning feasible and reliable motions of under-actuated AUVs. It captures the AUV inertias and actions on the vehicle, including the forces and moments experienced by the AUV, which are not considered in the kinematics model. In this section, the forces and moments exerted on the vehicle will be analysed in terms of the hydrodynamic effects resulting from the surrounding fluid and the propulsion actions from the equipped thrusters.

$$\mathbf{F}_{total} = \mathbf{F}_{hydrodynamics} + \mathbf{F}_{hydrostatic} + \mathbf{F}_{thrusters} \tag{3.6}$$

The total forces and moments mainly consist of three components as given in Equation (3.6), the forces and moments due to hydrodynamics, hydrostatic and thrusters, which will be elaborated sequentially.

3.1.2.1 Hydrostatic forces and moments

The hydrostatic force and moments result from the vehicle gravity and buoyancy (Prestero, 2001). The prototype AUV is neutrally buoyant, therefore the total hydrostatic force is zero. Since the Centre of Buoyancy (CoB) and the Centre of Gravity (CoG) of the AUV is not coincident but the CoG is lower than the CoB, hydrostatic moments in pitch and roll are generated as demonstrated in Figure 3.2 and Figure 3.3.

The moment shown in Figure 3.2 plays an important role in the stability of the AUV in roll as it tends to restore the vehicle from rolling. Whenever the AUV rolls, there will be a moment acting in the opposite direction to eliminate the roll and bring the AUV back to the original vertical orientation. As will be presented in Section 3.1.3.3, the thrusters on the AUV will generate a torque on the hull causing the vehicle to roll, however this torque can be balanced out by the hydrostatic moment in roll, assuming roll stability.

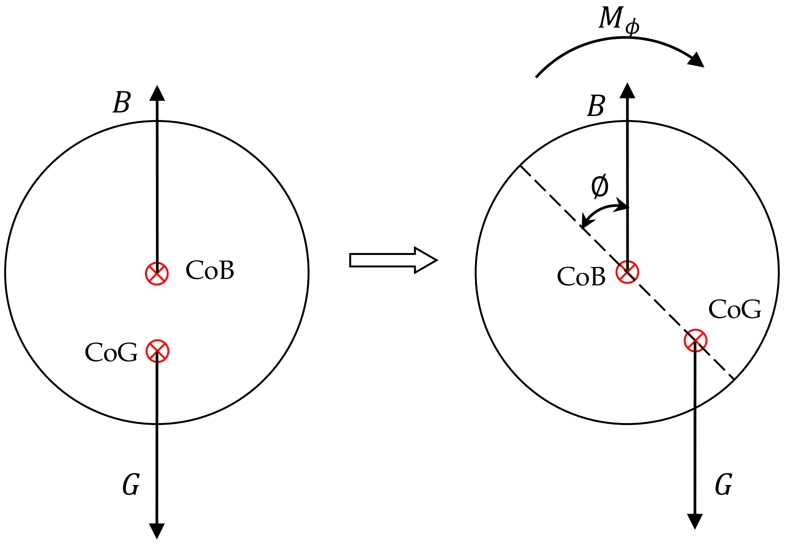

Figure 3.2: Hydrostatic moment in roll. The hydrostatic moment in roll M_ϕ results from the buoyancy (B) and gravity (G). When the roll angle ($\emptyset$) is not zero, this moment tends to restore the vehicle to bring the CoG back to align vertically with the CoB.

As shown in Figure 3.3, a hydrostatic moment is generated when the AUV pitches. This moment acts opposed to the pitching direction to realign the CoB and CoG of the AUV on the vertical plane. In this research, only motion on the horizontal plane of the AUV is considered, hence hydrostatic moment in roll and pitch can be neglected.

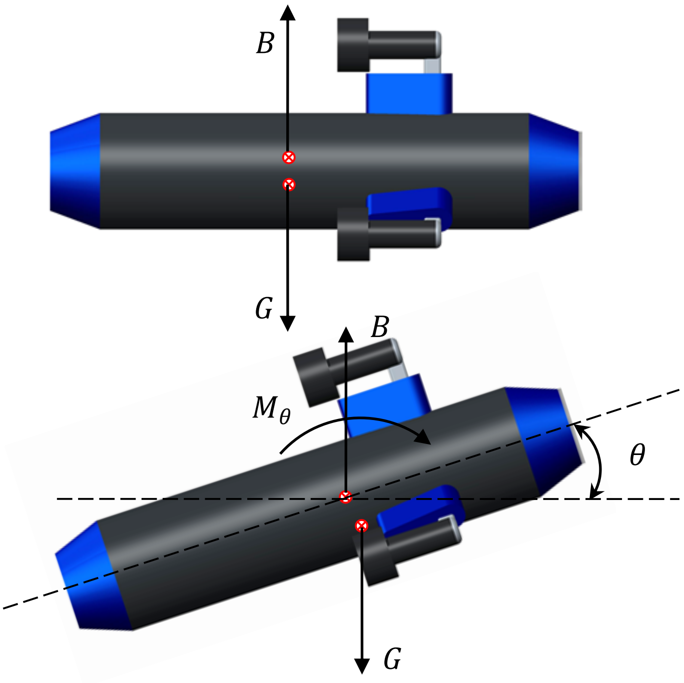

Figure 3.3: Hydrostatic moment in pitch. The hydrostatic moment in pitch, M_θ due to the buoyancy (B) and gravity (G) when the pitch angle (θ) is not zero, this moment tends to restore the vehicle to realign the CoG and CoB vertically.

3.1.2.2 Hydrodynamic forces - drag and lift

As illustrated from the side view of the prototype AUV in Figure 3.4 (a), the vehicle is moving at an angle (α) with respect to the fluid, experiencing drag, D, and lift, L. Similarly, the bottom view of the AUV in Figure 3.4 (b) demonstrates that the vehicle is travelling at a sideslip angle of β. Drag force is one of the main hydrodynamic non-conservative forces for ocean craft, and it has been extensively studied in the literature in many research fields. It is known as a resistance force arising from the fluid against which the vehicle is moving, and has an equivalent effect to the actual pressure field on the body. Lift is another hydrodynamic force. As demonstrated in Figure 3.4, lift force acts perpendicular to the vehicle motion on either the XY-plane or the XZ-plane of the B-frame. It results from the vehicle's motion when traversing at an angle. This angle can be the angle of attack for the XZ-plane, or the side slip angle for the XY-plane.

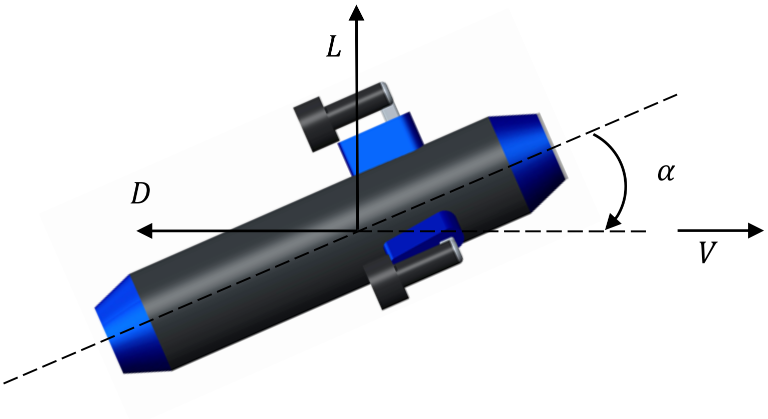

(a) Schematic of the side view of the AUV

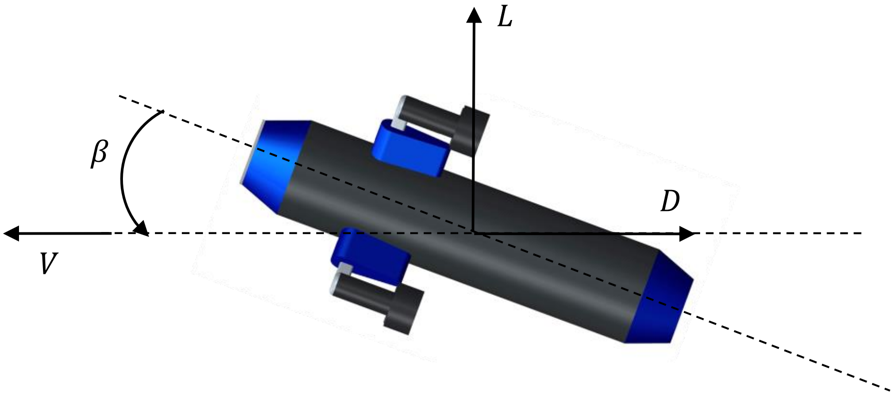

(b) Schematic of the bottom view of the AUV

Figure 3.4: Illustration of the angle of attack, sideslip angle, lift and drag on the AUV. (a) Side view of the AUV when it is travelling at an angle of attack, α. (b) Bottom view of the AUV when it is travelling at a sideslip angle of β.

The drag force is calculated by (Maeda *et al.*, 2001)

$$D = \frac{1}{2}\rho C_D A_f V^2, \tag{3.7}$$

$$C_D = \text{function}(R_e, \alpha, \beta)\,, \tag{3.8}$$

where D is the drag, ρ represents the density of the fluid, A_f is the frontal area of the vehicle, V stands for the incident/total velocity of the vehicle, and C_D refers to the drag coefficient, which is dependent on the Reynolds number R_e, the angle of attack α and the sideslip angle β (Ostafichuk, 2004). The Reynolds number R_e can be calculated as

$$R_e = \frac{\rho V D}{\mu}, \tag{3.9}$$

where μ is the dynamic viscosity of the fluid and D is the characteristic length.

Similar to drag, lift can be calculated as

$$L = \frac{1}{2}\rho C_L A_f V^2, \tag{3.10}$$

$$C_L = \text{function}(R_e, \alpha, \beta)\,, \tag{3.11}$$

where C_L is the lift coefficient, which is also related to the Reynolds number R_e, the angle of attack α and the sideslip angle β.

According to Equations (3.7) and (3.10), the drag and lift on the AUV can be determined once the drag and lift coefficients are derived. The estimation and verification of the hydrodynamic coefficients will be introduced in detail in Section 3.3.1.

3.1.2.3 Pitching and yawing drag

When the vehicle is making rotational manoeuvres, there will also be resistance exerted on the AUV from the surrounding fluid. Similar to the resistance force - the drag in translations that tends to stop the vehicle from accelerating to infinite speed translationally, the resistance moment – the drag in pitch and yaw, prevents the vehicle from rotating at an infinite angular velocity. Figure 3.5 demonstrates the rotational resistance on the side and top views of the AUV.

The hydrodynamic resistance moments in pitch and yaw can be calculated as parabolic functions of the AUV angular speed,

$$\begin{cases} M_q = C_q q^2 \\ M_r = C_r r^2, \end{cases} \tag{3.12}$$

where M_q and M_r are the hydrodynamic moments in the pitch and yaw directions, C_q and C_r are the pitching and yawing moment coefficients and q and r are the pitch and yaw rate (in Table 3.2).

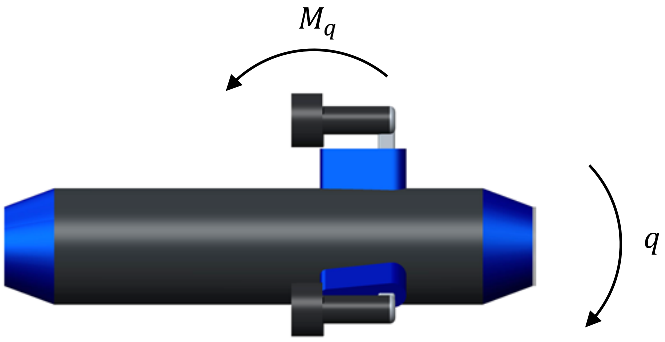

(a) Schematic of the AUV side view during pitching. The AUV is pitching clockwise at a rate of q on the XZ-plane, and a pitching drag in the anticlockwise sense will be acting on the AUV

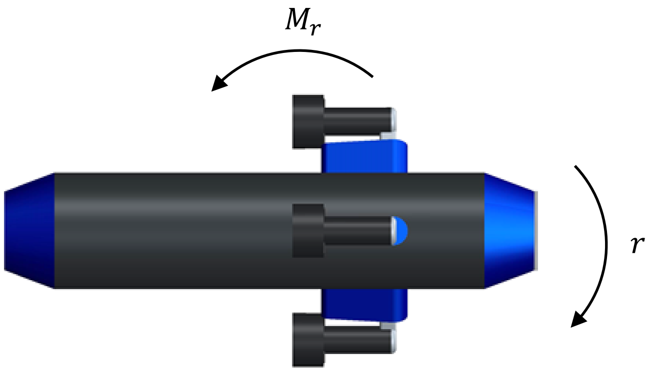

(b) Schematic of the AUV top view during yawing. When the AUV yaws clockwise at a rate of r on the XY-plane, there will be a yawing drag opposite to the yaw motion on the AUV

Figure 3.5: Rotational resistance effects on the AUV

As mentioned in Section 3.1.2.1, pitch motion in the vertical plane is out of the research scope, hence drag in pitch is neglected and only drag in yaw is considered in the AUV model.

3.1.3 Propulsion system dynamics

The manoeuvring mechanism of the differential thrust propulsion system will be introduced first. The original configuration was simplified for planar motion, and the manoeuvring model based on the modified differential thrust configuration will be presented. Lastly issues around the dynamics of the thrusters will be discussed.

3.1.3.1 Manoeuvring mechanism

The differential thrust system of the prototype AUV consists of three bi-directional thrusters, which actuates the AUV in three motion modes, respectively surge, pitch and yaw. The surge motion of the vehicle arises from the total thrust of the three, whilst the yaw and pitch motions are actuated using differential thrusts. Figure 3.6 shows the frontal view of the prototype AUV and will be used to demonstrate its working principle.

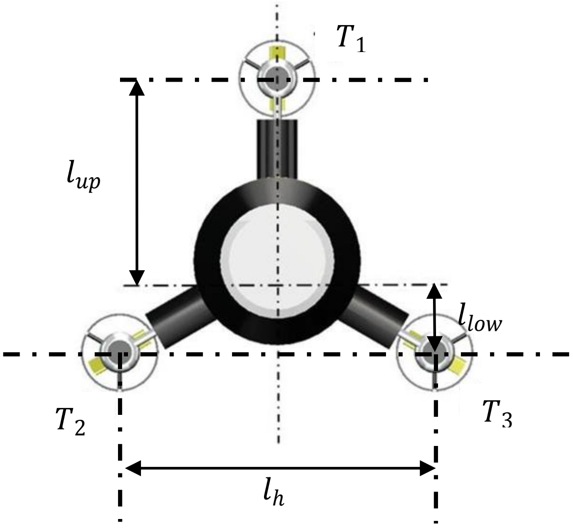

Figure 3.6: Schematic of the front view of the prototype AUV. T_1, T_2 and T_3 are the thrust forces from the top and bottom thrusters. l_{up}, l_{low} and l_h are the lever arms from the top and side thrusters to the rotational centre.

There are three available actuations using the three thrusters, namely the propulsion force (thrust), pitch torque and yaw torque. As summarised in Table 3.3, T is the total thrust force, M_y and M_z are the pitching and yaw torques resulting from the differential thrust. Also, the resultant motions from the three are named surge, pitch and yaw respectively.

Table 3.3: Actuation schemes of the differential thrust system in surge, pitch and yaw motion.

Motion	**Actuation schemes**
Surge	Propulsion T
Pitch	Pitch torque M_y
Yaw	Yaw torque M_z

These forces and moments from the differential thrust system are derived as

$$\begin{cases} T = T_1 + T_2 + T_3 \\ M_y = T_1 l_{up} - (T_2 + T_3) l_{low} \\ M_z = (T_2 - T_3)\dfrac{l_h}{2}, \end{cases} \tag{3.13}$$

where the surge motion is a result of the total thrust for propulsion generated by T_1, T_2 and T_3. The pitch moment results from the differential thrust between the top thruster T_1, and the sum of the bottom two thrusters $(T_2 + T_3)$. Similarly, the differential thrust generated by T_2 and T_3 produces a yaw moment.

3.1.3.2 Actuation configuration for planar motion

As the focus of this research is to investigate planar motion on the XY-plane, the AUV model is simplified based on a modified actuation configuration as demonstrated in Figure 3.7. Since the top thruster (Figure 3.7 (a)) correlates to pitch and brings more complex couplings in actuation, it is removed in the new configuration (Figure 3.7 (b)) and two thrusters are symmetrically placed on each side of the vehicle body. The thrust and torque of the new configuration can be calculated as

$$\begin{cases} T = T_1 + T_2 \\ M_z = \Delta T \dfrac{{l_h}'}{2} = (T_1 - T_2)\dfrac{{l_h}'}{2}, \end{cases} \tag{3.14}$$

where T_1, T_2 are the thrust forces of the side thrusters. The total thrust force T is the sum of the two. M_z is the yawing torque generated by the differential thrust, ΔT, and l_h' is the lever arm between the two thrusters.

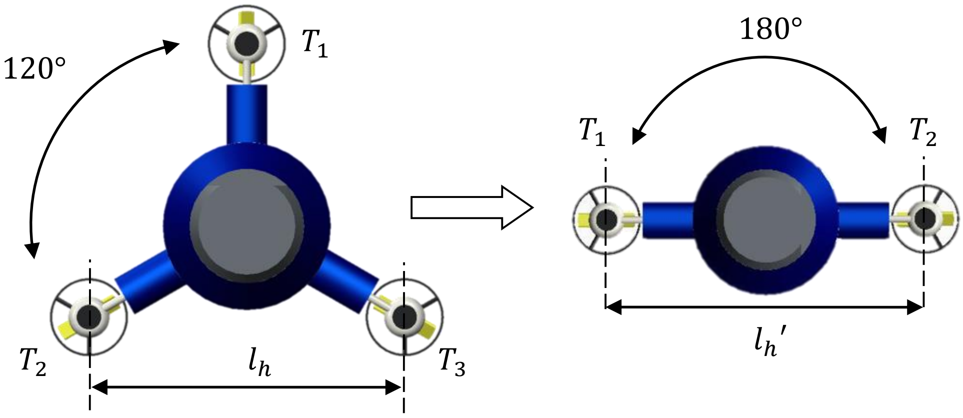

(a) The original three thrusters design (b) The two thrusters design

Figure 3.7: Differential thrust system configuration modified to investigate motion in 2D. There are three thrusters 120° apart from each other for the original configuration (a), whereas the revised configuration (b) consists of two thrusters 180° apart and is used for planar motion.

3.1.3.3 Thruster dynamics

In practice, the thruster dynamics are highly nonlinear (Cooney, 2006). A schematic of a typical thruster is demonstrated in Figure 3.8. The propeller is covered by a shroud and is driven by a motor.

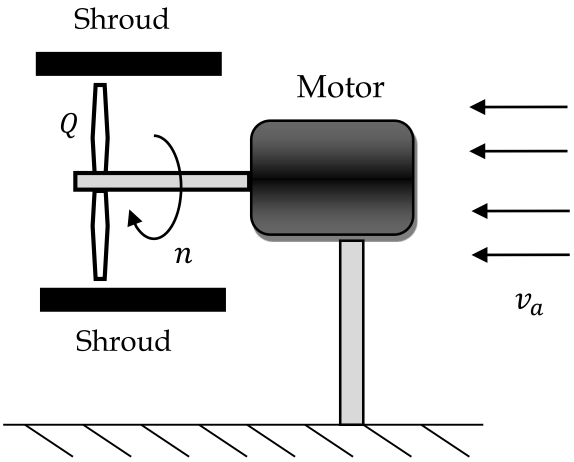

Figure 3.8: Schematic of a typical thruster. The propeller blade is rotating at a speed of n, the advance speed of the fluid is v_a, and the volumetric flowrate within the shroud is Q.

The propulsion force (thrust) and torque of the thrusters are respectively functions of the advance speed v_a (the actual water speed of the AUV relative to the blade of the thrusters), the rotational speed of the propeller n, and the geometric factors of the thruster, such as the pitch of the propeller, θ_p, and the duct area, A.

For fixed thruster geometry, where both the pitch and the duct area are constants, the thrust, T and torque, M of a thruster can be determined by the following dynamics functions (El-Hawary, 2001):

$$\begin{aligned} T &= \rho D^4 K_T(J_0)n|n|\,, \\ M &= \rho D^5 K_Q(J_0)n|n|\,, \end{aligned} \tag{3.15}$$

where ρ is the density of the surrounding fluid, D is the diameter of the thruster. J_0 is a non-dimensional term, which is called the advance ratio and can be calculated by

$$J_0 = \frac{v_a}{nD}\,. \tag{3.16}$$

The thrust and torque coefficients K_T and K_Q are functions of J_0 . These two coefficients are often determined from water tests (Liang *et al.,* 2008). When the thrusters are in operation, the torque tends to cause a rolling motion on the AUV body. For the maximum thrusts of 30 N for both thrusters of the prototype AUV, the maximum torque in roll is 5.69 $\mathrm{N} \cdot \mathrm{m}$. As analysed in Section 3.1.2.1, there is a counteracting moment so the AUV remains stable in roll, due to the fact that the CoG (Centre of Gravity) is designed to be lower than the CoB (Centre of Buoyancy), and therefore the system will be stable as the metacentre is always higher than the CoG (Techet, 2005).

As for the AUV modelling, the dynamics of the thruster can be treated as the lowest control loop of the system (Kim, 2008). In Figure 3.9, a block diagram of the AUV system with the thruster control loop is illustrated.

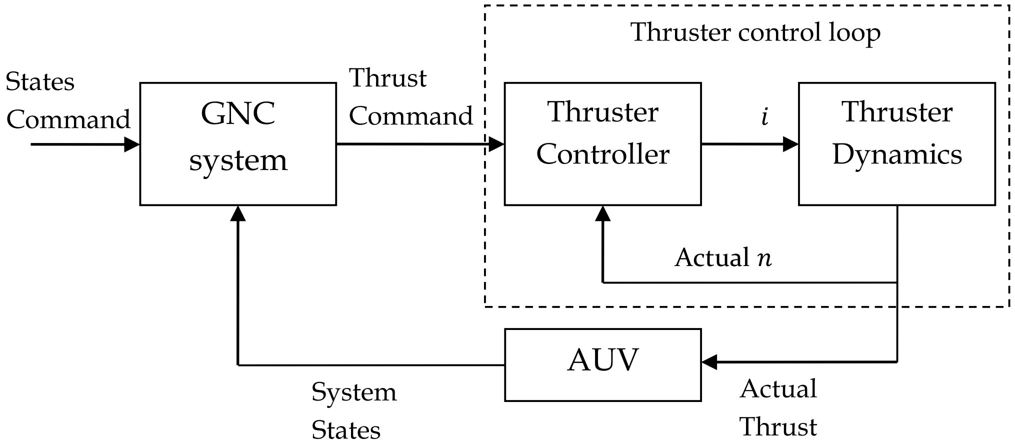

Figure 3.9: Block diagram of the AUV system with thruster control loop. The thrust command generated from the GNC system is fed into the thruster control loop, then the thruster controller determines the required current i. The actual rotational speed of the propeller n is fed back to the controller to adjust the current.

When the thrusters are under servo control, the time constant of the servo motor is very short. For example, for a MAXON 90W DC motor, which is similar to the one used in the prototype AUV in terms of power and size, a mechanical time constant of 5.65 ms can be achieved (Maxon Motor, 2015). In contrast, the response time of the AUV, as will be demonstrated in Section 3.3.2.1, is nearly 3 seconds for linear acceleration to its top speed. Moreover, the thrust force decreases as the traversing speed of the AUV increases, and the relationship between the two is complex depending on many thruster-specific properties. This can be obtained by water tests, but is beyond the scope of this research project. According to the literature review, the thruster dynamics can be neglected for simplification and is modelled as a source of constant thrust and torque in the AUV model (Prestero, 2001).

3.2 Complete AUV model

With all aspects of the dynamics model analysed, a complete three degree-of-freedom AUV model can be constructed. The governing equations and the Simulink model were derived, and both will be presented in this section.

3.2.1 Three degree-of-freedom model for planar motion

The model considers both the kinematics and dynamics of the AUV during planar motion. Based on Equation (3.2) and (3.3), the kinematics equations can be reduced to

$$\begin{bmatrix} u \\ v \\ r \end{bmatrix} = \begin{bmatrix} \cos\psi & -\sin\psi & 0 \\ \sin\psi & \cos\psi & 0 \\ 0 & 0 & 1 \end{bmatrix} \begin{bmatrix} \dot{x} \\ \dot{y} \\ \dot{\psi} \end{bmatrix}. \tag{3.17}$$

The total velocity of the vehicle is

$$V = \sqrt{u^2 + v^2} = \sqrt{\dot{x}^2 + \dot{y}^2}. \tag{3.18}$$

The angle of the velocity relative to the X-axis, χ, in the G-frame and sideslip angle β can be derived as

$$\begin{aligned} \chi &= \tan^{-1}\frac{\dot{y}}{\dot{x}}, \\ \beta &= \tan^{-1}\frac{v}{u}. \end{aligned} \tag{3.19}$$

The governing equations of the 3DOF model can be expressed in the G-frame as

$$\begin{aligned} \sum F_x &= T_x + D_x + L_x = m\ddot{x}\,, \\ \sum F_y &= T_y + D_y + L_y = m\ddot{y}\,, \\ \sum M_z &= M_z + M_r = I_{zz}\ddot{\psi}\,, \end{aligned} \tag{3.20}$$

where $\sum F_x$ and $\sum F_y$ are the total forces along the X and Y axes, $\sum M_z$ is the total moment about the Z axis. T_x and T_y are the X and Y components of the total thrust. D_x and D_y are the X and Y components of drag, while L_x and L_y are the components of lift. m is the mass of the vehicle, and I_{zz} is the moment of inertia about the Z axis. The governing equations can be expanded

$$
\begin{gathered}
\sum F_x = (T_1 + T_2)\,\mathrm{c}\,\psi + \frac{1}{2}\rho A C_D V^2(\mathrm{c}\,\beta\,\mathrm{c}\,\psi + \mathrm{c}\,\beta\,\mathrm{c}\,\psi) + \frac{1}{2}\rho A C_L V^2(\mathrm{s}\,\beta\,\mathrm{c}\,\psi + \mathrm{s}\,\beta\,\mathrm{c}\,\psi),\\
\sum F_y = (T_1 + T_2)\,\mathrm{s}\,\psi + \frac{1}{2}\rho A C_D V^2(\mathrm{s}\,\beta\,\mathrm{s}\,\psi + \mathrm{s}\,\beta\,\mathrm{s}\,\psi) + \frac{1}{2}\rho A C_L V^2(\mathrm{c}\,\beta\,\mathrm{s}\,\psi + \mathrm{c}\,\beta\,\mathrm{s}\,\psi),\\
\sum M_z = (T_1 - T_2) l_h' + C_r \dot{\psi}^2,
\end{gathered}
\tag{3.21}
$$

where s and c are acronyms of $\sin(\cdot)$ and $\cos(\cdot)$ respectively. As will be demonstrated in Section 3.3.1, the hydrodynamic coefficients C_D and C_L are determined according to the theoretical formulas and experimental results.

3.2.2 Simulink model

The block diagram of the three degree-of-freedom Simulink model is presented in Figure 3.10. It can be seen that the thrust outputs from the two thrusters T_1 and T_2 are used to calculate the total thrust and differential thrust for manipulating the AUV. The total thrust is transformed from the B-frame to the G-frame, and is resolved into two components T_x and T_y. The differential thrust is used to determine the moment in yaw M_z by Equation (3.14).

Meanwhile, the hydrodynamic function blocks calculate the drag, D, lift, L, and yawing drag, M_r, using the instantaneous speed, V, yaw rate, r and sideslip angle, β. As the AUV block outputs states in the G-frame, the instantaneous speed and sideslip angle are derived by Equations (3.17), (3.18) and (3.19). Once the drag and lift are determined, they are transformed from the SF-frame to the G-frame, which result in four components, L_x, L_y, D_x and D_y respectively.

When the external forces and moments from the hydrodynamics and thrusters are determined, taking the summation of them gives the resultant forces $\sum F_x$, $\sum F_y$ and moment $\sum M_z$, which are the three inputs to the AUV in the G-frame.

The AUV inertia block, in linear state space form, can be expressed as

$$\begin{bmatrix} \ddot{x} \\ \dot{x} \\ \ddot{y} \\ \dot{y} \\ \dot{r} \\ r \end{bmatrix} = \mathbf{A} \begin{bmatrix} \dot{x} \\ x \\ \dot{y} \\ y \\ r \\ \psi \end{bmatrix} + \mathbf{B} \begin{bmatrix} \sum F_x \\ \sum F_y \\ \sum M_z \end{bmatrix}, \tag{3.22}$$

$$\begin{bmatrix} \dot{x} \\ x \\ \dot{y} \\ y \\ r \\ \psi \end{bmatrix} = \mathbf{C} \begin{bmatrix} \dot{x} \\ x \\ \dot{y} \\ y \\ r \\ \psi \end{bmatrix} + \mathbf{D} \begin{bmatrix} \sum F_x \\ \sum F_y \\ \sum M_z \end{bmatrix}, \tag{3.23}$$

or

$$\mathbf{G} = \begin{bmatrix} \mathbf{A} & \mathbf{B} \\ \mathbf{C} & \mathbf{D} \end{bmatrix},$$

where

$$\mathbf{A} = \begin{bmatrix} 0 & 0 & 0 & 0 & 0 & 0 \\ 1 & 0 & 0 & 0 & 0 & 0 \\ 0 & 0 & 0 & 0 & 0 & 0 \\ 0 & 0 & 1 & 0 & 0 & 0 \\ 0 & 0 & 0 & 0 & 0 & 0 \\ 0 & 0 & 0 & 0 & 1 & 0 \end{bmatrix}, \mathbf{B} = \begin{bmatrix} \frac{1}{m} & 0 & 0 \\ 0 & 0 & 0 \\ 0 & \frac{1}{m} & 0 \\ 0 & 0 & 0 \\ 0 & 0 & \frac{1}{I_{zz}} \\ 0 & 0 & 0 \end{bmatrix},$$
$$\mathbf{C} = \begin{bmatrix} 1 & 0 & 0 & 0 & 0 & 0 \\ 0 & 1 & 0 & 0 & 0 & 0 \\ 0 & 0 & 1 & 0 & 0 & 0 \\ 0 & 0 & 0 & 1 & 0 & 0 \\ 0 & 0 & 0 & 0 & 1 & 0 \\ 0 & 0 & 0 & 0 & 0 & 1 \end{bmatrix}, \mathbf{D} = \begin{bmatrix} 0 & 0 & 0 \\ 0 & 0 & 0 \\ 0 & 0 & 0 \\ 0 & 0 & 0 \\ 0 & 0 & 0 \\ 0 & 0 & 0 \end{bmatrix}. \tag{3.24}$$

m and I_{zz} are the mass and moment of inertia of the vehicle. The AUV block outputs are the states $\dot{x}, \dot{y}, r, x, y, \psi$ in the G-frame. As shown in Figure 3.10, the entire Simulink model is in a closed loop form, representing the AUV dynamics in three degrees of freedom.

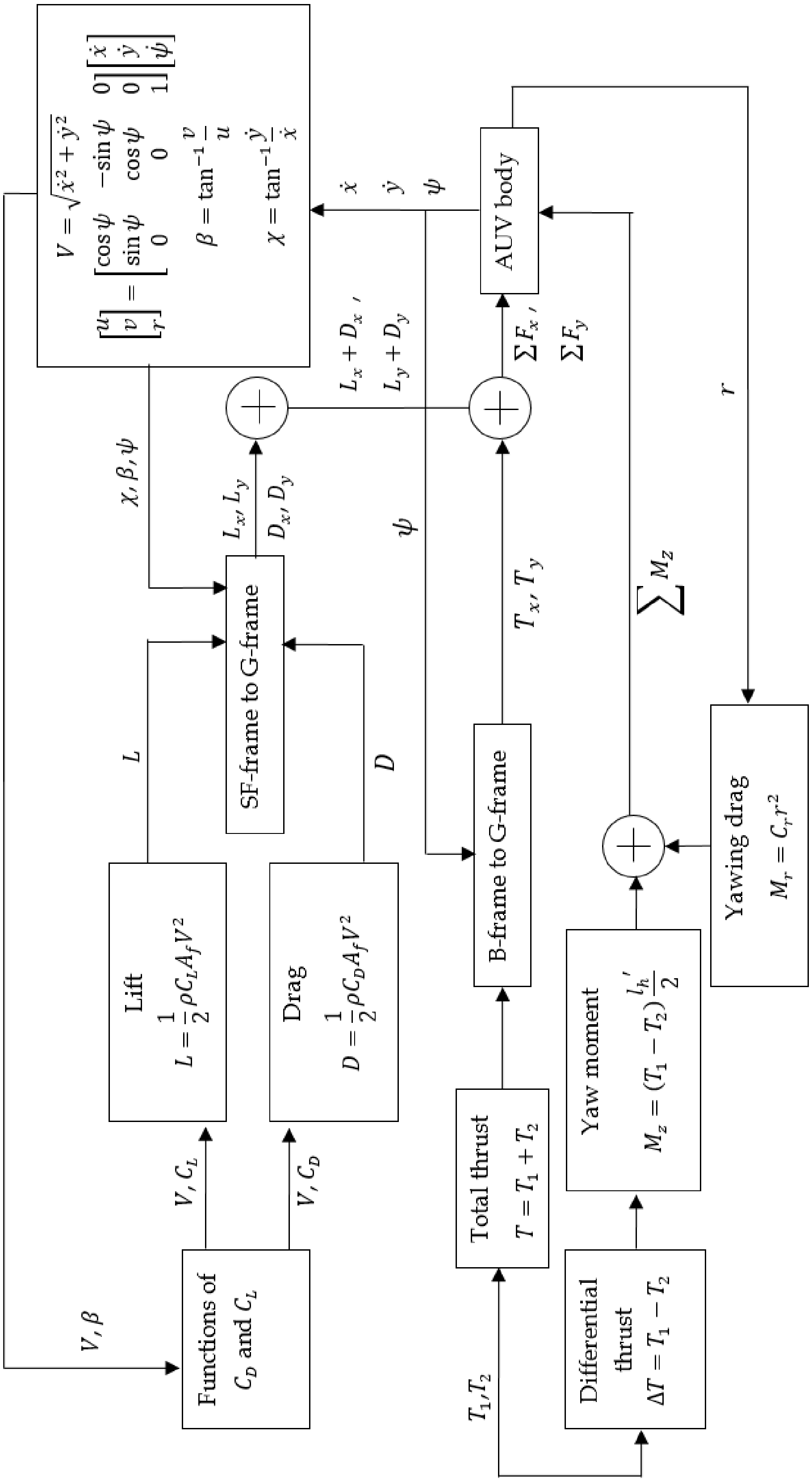

Figure 3.10: Block diagram of the 3DOF Simulink model

3.3 Model verification

In this section, the theoretical model will be verified. The verification begins with the hydrodynamic coefficients. Although the accuracy of these coefficients is not the focus of the thesis, it is crucial that the estimated coefficients in the model retain the key features of the dynamics. Simulations were performed to examine the AUV model in response to some simple commands in order to verify the main characteristics of the hydrodynamics and the differential thrust are kept.

3.3.1 Estimation and verification of hydrodynamic coefficients

As mentioned in Chapter 2, the hydrodynamic coefficients in the model were estimated based on existing formulas (Allen and Perkins, 1951) on bodies with similar shape and empirical results (Pavloudis *et al.,* 2012). Allen and Perkins' formulas (1951) as given in Equation (3.25), provide a theoretical solution to the drag and lift coefficients,

$$\begin{aligned} C_D &= C_{DF}\,(\cos\beta)^3 + (k_2-k_1)\tfrac{S_b}{A}\sin 2\beta\,\sin\tfrac{\beta}{2} + \eta C_{DC}\tfrac{A_P}{A}(\sin\beta)^3, \\ C_L &= (k_2-k_1)\frac{S_b}{A}\sin 2\beta\,\cos\frac{\beta}{2} + \eta C_{DC}\frac{A_P}{A}(\sin\beta)^2\cos\beta\,, \end{aligned} \tag{3.25}$$

where C_{DF} is the drag coefficient of the hull when the hull is parallel to the flow/motion, C_{DC} is the crossflow drag coefficient of the cylinder section, S_b is the cross-sectional area, A_p and A are respectively the plan-form area of the AUV and reference area (which depends on the object, i.e., cross-sectional area for a sphere, and wing area for an aeroplane). Moreover, (k_2-k_1) is called the apparent mass factor, which is dependent on the fineness ratio:

$$f = \frac{l}{d}, \tag{3.26}$$

where l and d are respectively the length and diameter of the cross section. The value of (k_2-k_1) is determined according to Table 3.4.

Table 3.4: Lookup table of the apparent mass factor (Evans, 2003)

f	$(k_2 - k_1)$
1	0
1.5	0.316
2	0.493
2.5	0.607
3	0.681
4	0.778
∞	1

For the prototype AUV with $f = 3.3$, the apparent mass factor can be interpolated from Table 3.4, which is 0.713. Hence the drag and lift coefficients can be derived as shown in Figure 3.11. Additionally, the coefficients derived from the formulas were compared with the data from earlier wind tunnel tests conducted on the actual prototype AUV. The tests were performed for an Honours project in the School of Mechanical Engineering at the University of Adelaide (Pavloudis *et al.*, 2012), and details can be found in Appendix A.

The comparison of the formulation of the drag coefficients and the empirical data is demonstrated in Figure 3.11. It can be seen that the drag coefficients from the wind tunnel test show good overall agreement with the theoretical values using the formulae in Equation (3.25). There is little variation between the drag coefficients from the wind tunnel test at different Reynolds numbers, $R_e = 5.91 \times 10^5$ and $R_e = 1.06 \times 10^6$. Theoretically, the drag coefficient is dependent on the Reynolds number. However, when the Reynolds number is above 10^4, the flow becomes highly turbulent, the drag coefficients are dominated by the geometric structure of the AUV and therefore the coefficients remain constant for non-deformable bodies (Çengel *et al.*, 2011).

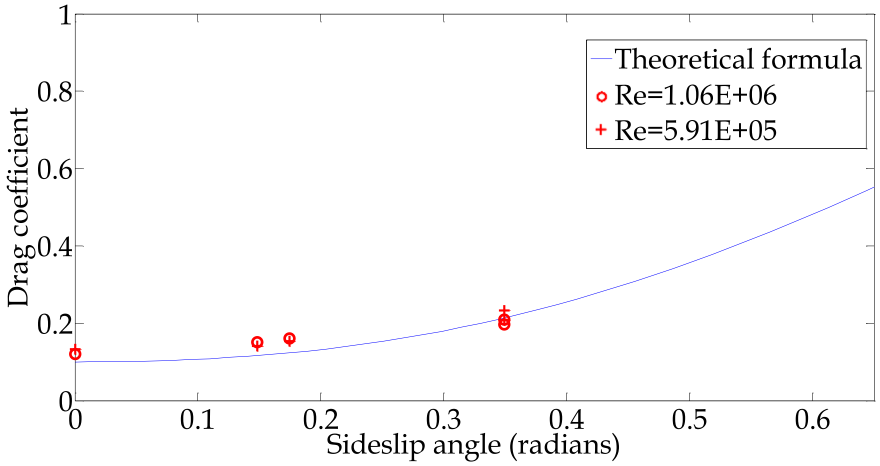

Figure 3.11: The drag coefficients derived by the theoretical formula (Equation (3.25)), are compared with data from the wind tunnel test for (a) $R_e = 5.91 \times 10^5$ and (b) $R_e = 1.06 \times 10^6$.

In terms of the lift coefficient, Prestero (1994) found large variations (over an order of magnitude) in the estimation of lift coefficients by using four different methods. These methods involve empirical studies on torpedos and theoretical studies on AUVs, but the numerical values of the lift coefficients may be very sensitive to small variations in the geometric structure. Therefore, the lift coefficients from the wind tunnel test are considered more reliable to use in the model (Prestero, 1994). The lift coefficients from the wind tunnel test were used for curve fitting and parameters in the theoretical function are determined as given

$$C_L = 0.112 \sin 2\beta \cos\frac{\beta}{2} - 0.121(\sin\beta)^2 \cos\beta\,. \tag{3.27}$$

Figure 3.12 illustrates a comparison between the wind tunnel test results and the theoretical formulae given by Equation (3.25), and showed an adequate agreement. Hence the lift coefficients can be determined according to the sideslip angle, β.

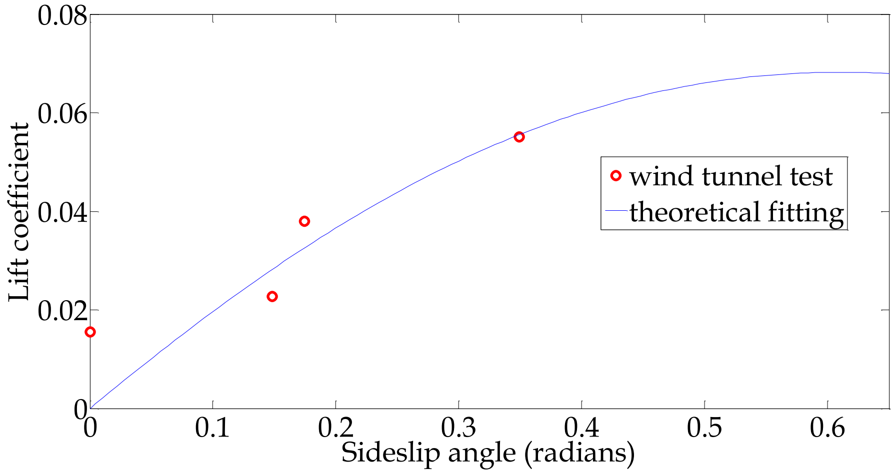

Figure 3.12: Curve fitting of lift coefficients based on the wind tunnel test. The lift coefficients were obtained from the wind tunnel test, and were fitted to a curve correlated to the theoretical formulae given by Equation (3.25).

3.3.2 Simulations

Simulations were performed based on a range of intuitive physical scenarios and the system response in each case was studied. As will be illustrated, the results demonstrated consistency with reality, which indicates that the theoretical model is suitable for the development of the guidance and control system. Details of the simulations and the results will be discussed in this section.

Table 3.5: Simulation scenarios and the corresponding thruster setting

Case	Scenario	Thrusters setting
1	Rectilinear acceleration	Full thrust and $T_1 = T_2$
2	Rotational acceleration	Full thrust and $T_1 = -T_2$
3	Curvilinear motion on XY-plane	Constant differential thrust

As summarised in Table 3.5, three intuitive scenarios were selected. In the first case, both thrusters are fully on in the same direction so the AUV should perform maximum acceleration along a straight line. In the second case, both thrusters are still fully on, but opposite in direction, so the vehicle would spin with maximum rotational acceleration. The last case simulates curvilinear motions on the XY-plane. The AUV response under these operations was recorded and plotted for analysis, which will be presented in the subsequent sections.

3.3.2.1 Case 1: Rectilinear acceleration

The first case is to verify the translational dynamics of the model by simulating the rectilinear acceleration of the AUV under full thrust. The AUV was initially at rest and started accelerating with $T_1 = 30$ N and $T_2 = 30$ N, which results in 60 N of total thrust. The velocity evolution during the rectilinear acceleration with respect to time is plotted in Figure 3.13.

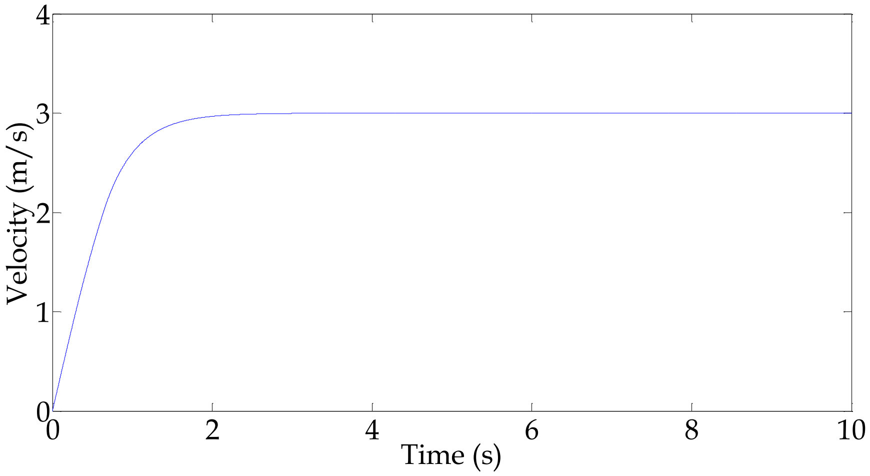

Figure 3.13: The velocity evolution during acceleration with full thrust. The motion in the first 10 seconds is plotted. It took the vehicle approximately 2.5 seconds to reach its maximum speed (which is 3 m/s) from stationary.

The slope of the curve represents the acceleration, and it can be seen that it decreases as the velocity increases. Intuitively, this is due to the fact that higher speed induces higher drag. As derived in Equation (3.20), the increase in resistance leads to the reduction of total force if the propulsion force is constant. Moreover, the top speed of the prototype AUV obtained from field testing is approximately 3 m/s (Jin *et al.*, 2011). Therefore, it can be seen that the rectilinear response of the AUV shows reasonable agreement with the physical tests.

3.3.2.2 Case 2: Rotational acceleration

In the second case, the AUV starts rotating from stationary to verify the rotational dynamics of the model. Both T_1 and T_2 were set to maximum thrust, but in opposite directions. In this case, $T_1 = 30$ N and $T_2 = -30$ N. Therefore, the differential thrust is 60 N, which results in 9 Nm of yaw moment on the vehicle according to Equation (3.14). The rotational motion response with respect to time is demonstrated in Figure 3.14.

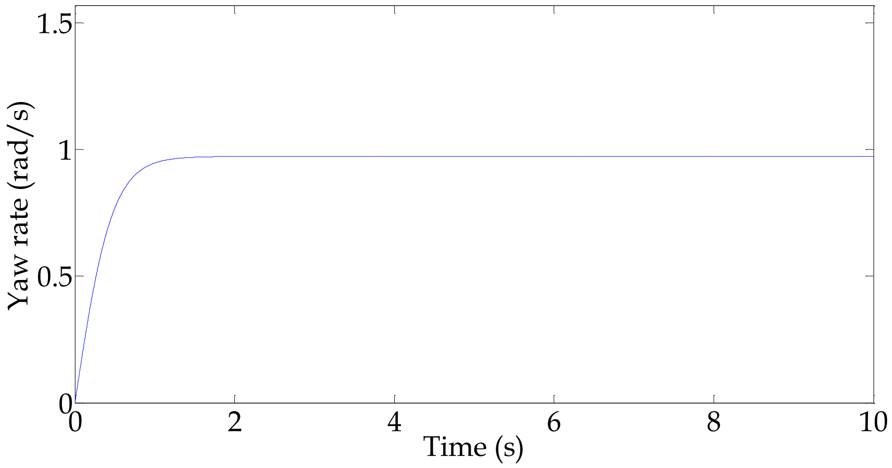

Figure 3.14: The angular velocity evolution during rotational acceleration. The system response within the first 10 seconds was plotted. It can be seen that the yaw rate increases from zero and reaches the maximum (0.8 rad/s) within 1.8 seconds. The slope of the curve is the yaw acceleration, which decreases as the yaw rate increases due to the increase in the rotational resistance (yawing drag) on the vehicle.

Similar to the translational motion response in the first case, the rotational acceleration, the slope of the curve, decreases with respect to time. As the rotational resistance (yawing drag) is proportional to the square of the yaw rate according to Equation (3.12), larger rotational speed incurs larger yaw resistance, hence the angular acceleration reduces. The rotational speed eventually converges to a constant value when the yawing drag is equal to the yaw moment due to the differential thrust. Also the simulation result is compared with the field test result. In the field test, it took the vehicle 2.51 seconds to yaw 90 degrees ($\frac{\pi}{2}$ radians)

(Jin *et al.*, 2011). A similar result of 2.35 seconds for the same yaw movement is found from the simulation.

3.3.2.3 Case 3: Planar motion on the XY-plane

In the last case, the AUV motion on the XY-plane was evaluated to verify both the translational and rotational dynamics of the model. The simulations were conducted under three sets of thrusts. The thruster values in each set, and the corresponding differential thrust and the total thrust of each set can be calculated as

$$\begin{cases} T = T_1 + T_2 \\ \Delta T = T_1 - T_2. \end{cases} \tag{3.28}$$

Table 3.6: Thruster set up and resultant thrust and differential thrust, where T is the total thrust and ΔT represents the differential thrust, which are determined by Equation (3.28).

Simulation	T_1 (N)	T_2 (N)	ΔT (N)	T (N)
1	20	10	10	30
2	25	5	20	30
3	30	0	30	30

As shown in Table 3.6, the thrusters were set up in a way that the total thrust remained at 30 N and the differential thrust was increased from 10 N to 30 N in the three simulations.

The resultant trajectories of the AUV for applying the three sets of actuations are demonstrated in Figure 3.15, which are respectively represented by the green solid line (Simulation 1), the dotted blue line (Simulation 2) and the dashed red line (Simulation 3).

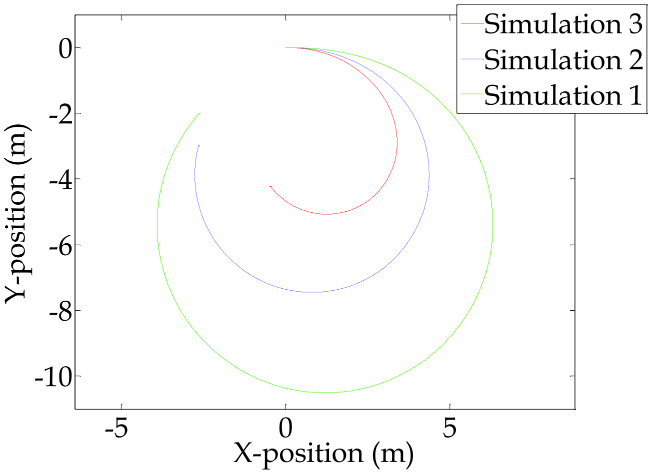

Figure 3.15: Resultant paths in the three simulations. The green, blue and red curves are the resultant paths in Simulation 1, 2, and 3 respectively.

It can be seen that the larger the differential thrust is, the larger the curvature of the resultant path, under the same total thrust of 30 N. According to Equation (3.11), higher differential thrust yields larger yaw moment, hence results in smaller turning radius. For all three cases, the vehicle gradually converges to circular paths with different radii of curvature as the system reaches its steady state. For example, the resultant path in Simulation 3, is plotted in Figure 3.16.

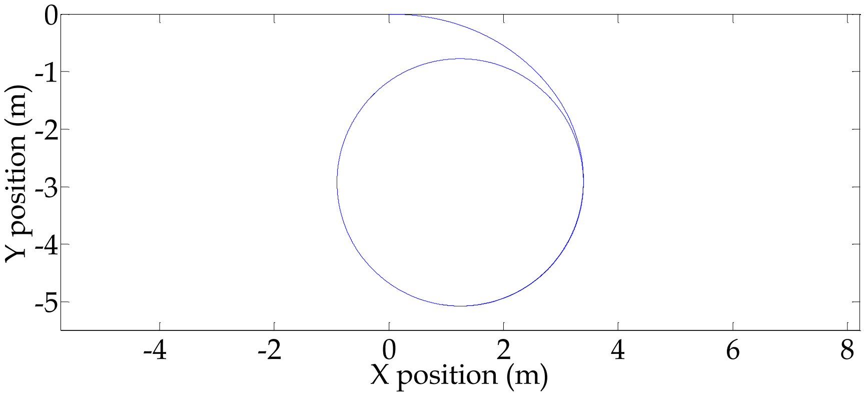

Figure 3.16: Resultant path and the AUV orientation in Simulation 3. The AUV converges to a circular path in Simulation 3. The radius of curvature of the circular path is approximately 2 m.

The orientation of the vehicle along the resultant path is plotted in Figure 3.17. It can be seen that the orientation of the vehicle is not aligned with the motion, but at a sideslip angle, β.

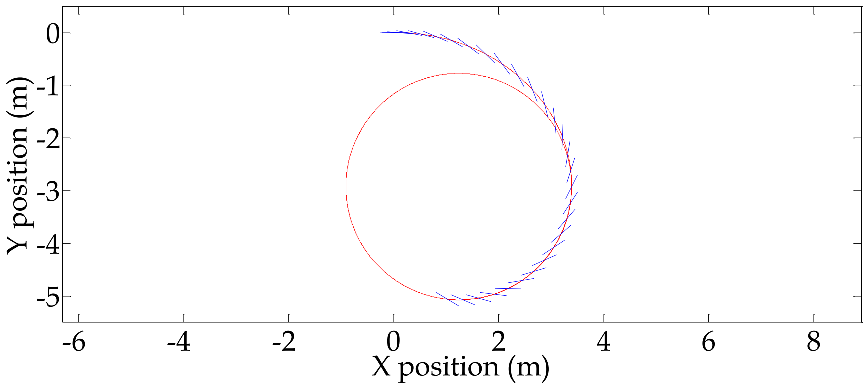

Figure 3.17: The evolution of the AUV orientation along the resultant path in Simulation 3. The vehicle is heading towards the inner side of the curve.

This is due to the dynamics of the differential thrust maneuvering. For conventional fin-maneuvered AUVs, the centripetal force required for a circular motion is generated through fin deflection. Without fins, the prototype AUV has to steer inwards on the curve as shown in Figure 3.17. Therefore the sideslip angle results in a component of the thrust force and a lift force, from which the centripetal force can be sourced, as will be analyzed in Chapter 4. The evolution of the sideslip angle is demonstrated in Figure 3.18 (a). As shown in the plot, the sideslip angle increases from zero and takes approximately 5 seconds to stabilize at 0.44 radians (25 degrees).

Other AUV responses including the total speed and yaw rate with respect to time are also plotted. In Figure 3.18 (b), it can be seen that the total velocity increases then decreases, and eventually converges to 1.47 m/s. Reasons behind these system responses are analyzed next.

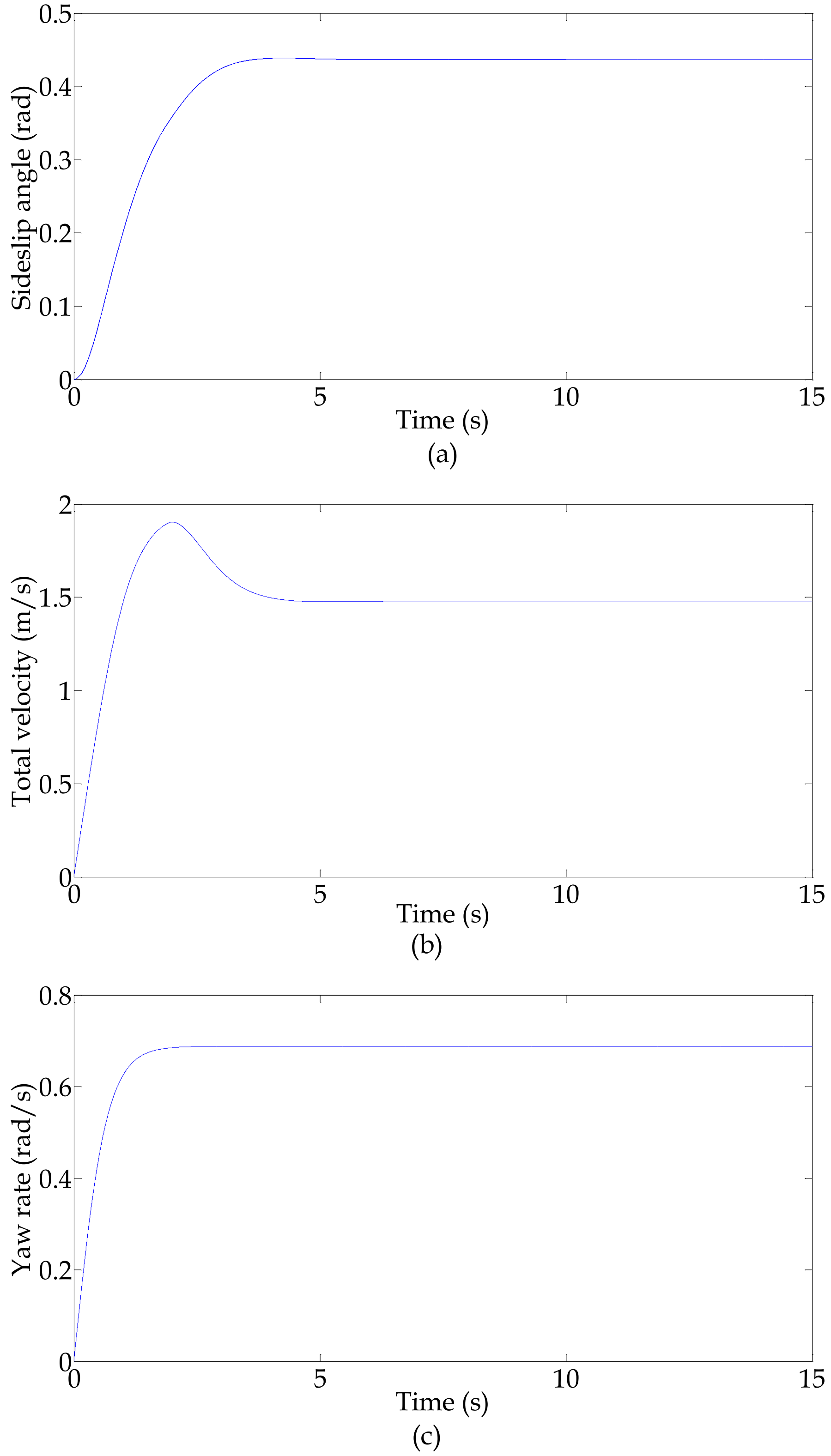

Figure 3.18: AUV response in simulation 3 within 15 seconds. (a) The sideslip angle increases from zero and converges to 0.44 radians (b) The total speed increases to 1.9 m/s then gradually decreases and converges to 1.47 m/s (c) The yaw rate increases and reaches 0.69 rad/s.

When the vehicle is operating at an angle to the motion, the total force in the motion direction is,

$$\Sigma F_t = D + T_t = ma_t \,, \tag{3.29}$$

where D is the drag force, a_t is the acceleration and T_t is the component of the total thrust in the motion direction, and is given by

$$T_t = T \cos \beta \,. \tag{3.30}$$

As the speed and sideslip angle increases, the drag force, D increases, whereas T_t decreases. Initially, D is lower than T_t, so the AUV keeps accelerating until its speed reaches $1.9\ \mathrm{m/s}$. As the sideslip angle continues increasing, D exceeds T_t, and hence the AUV starts decelerating until it reaches its steady state.

In Figure 3.18 (c), the yaw rate increases and converges to $0.69\ \mathrm{rad/s}$. The rotational acceleration, which is represented by the slope of the curve, decreases with increasing yaw rate. According to Equation (3.12) and (3.21), larger yawing drag is induced by higher yaw rate, hence the rotational acceleration reduces under constant differential thrust.

3.4 Summary

In this chapter, a theoretical model based on an under-actuated differential thrust prototype AUV has been established. The configuration of the original prototype AUV was modified for planar motion, and a model was developed in Simulink taking into account both the AUV kinematics and dynamics. The estimation and verification of hydrodynamic coefficients was performed based on a combination of theoretical formulations and empirical results. In addition, the Simulink model was examined through several simulations of basic scenarios. From the analysis of the AUV responses in these simulations, it can be seen that both the hydrodynamics and differential thrust actuation are effectively modelled and validated, which provides a platform for the development of the guidance system. Also, as will be presented in Chapter 4, a numerical method for the derivation of the AUV motion limit will be applied to the AUV model.

Chapter 4

AUV motion analysis

4.1 Problem description

To achieve time-efficient path following, it is desirable for the guidance system to generate motion references allowing the AUV to follow the path as fast as possible at all times. Feasible motion references need to satisfy both the path curvature and system dynamics constraints. This results in a problem of investigating the motion limit of the AUV along predefined paths, which will be addressed in this chapter. The problem will be analysed both analytically and numerically. The analytical analysis of the AUV dynamics gives an insight into the problem and identifies the key factors and their interconnections, whereas a Monte Carlo Analysis provides a practical solution to derive the motion limit of the AUV.

4.2 Analytical analysis

The dynamics of the AUV following a given path on the XY-plane is analysed. In Figure 4.1, the forces experienced by the vehicle are illustrated. As shown, the AUV is orientated inward of the path and moving in the clockwise sense. V represents the speed. A SF-frame can be established. As introduced in Chapter 3, the two axes of the SF-frame, represented by **T** and **N**, are pointing to the path tangential (motion direction) and normal direction.

At any instant, the thrust force, T, represented by the red arrow, is aligned with the vehicle orientation. Drag, D, shown by the blue arrow, is opposite to the motion of the vehicle (in **T** direction). With the vehicle traversing at an angle, β, the lift force, L (the arrow in green), acts in the **N** direction – perpendicular to the motion on the horizontal plane (XY-plane).

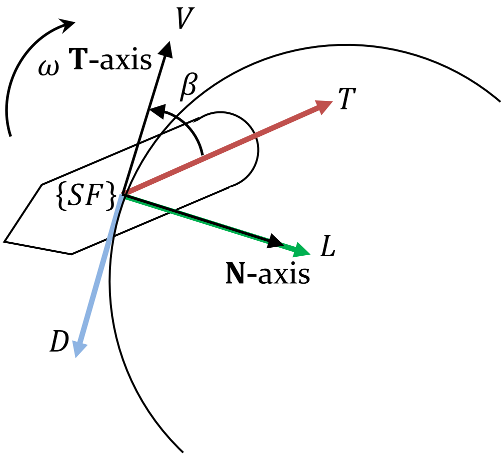

Figure 4.1: Schematic of an AUV traversing along a planar path. The AUV (round end is the front of the AUV and sharp end is the aft) is orientated to the inside of the curve at a sideslip angle, β. A SF-frame is used, with its **T**-axis and **N**-axis pointing to the motion and its perpendicular directions. The coloured arrows are the forces exerted on the vehicle, namely the drag (blue), lift (green) as well as the thrust force (red).

In the SF-frame, T can be resolved into two components, T_t and T_n, in the path tangential (**T**) and normal (**N**) direction respectively,

$$\begin{cases} T_n = T\sin\beta \\ T_t = T\cos\beta\,. \end{cases} \tag{4.1}$$

Therefore, the resultant forces on the AUV in the path-normal and tangential direction are

$$\begin{cases} \Sigma F_n = L + T_n \\ \Sigma F_t = D + T_t\,. \end{cases} \tag{4.2}$$

Combining Equation (4.1) and Equation (4.2) gives

$$\begin{cases} \Sigma F_n = L + T\sin\beta \\ \Sigma F_t = D + T\cos\beta\,. \end{cases} \tag{4.3}$$

As derived in Chapter 3, the hydrodynamic forces on the vehicle, the lift and drag, are dependent on the sideslip angle and velocity,

$$L = L(V,\beta) = \frac{1}{2}\rho C_L(\beta) A_f V^2, \tag{4.4}$$

$$D = D(V,\beta) = \frac{1}{2}\rho C_D(\beta) A_f V^2. \tag{4.5}$$

Then Equation (4.3) becomes,

$$\begin{cases} \Sigma F_n = L(V,\beta) + T\sin\beta \\ \Sigma F_t = D(V,\beta) + T\cos\beta\,. \end{cases} \tag{4.6}$$

According to Newton’s second law, the following relationships hold:

$$\begin{cases} \Sigma F_n = L(V,\beta) + T\sin\beta = ma_n \\ \Sigma F_t = D(V,\beta) + T\cos\beta = ma_t\,. \end{cases} \tag{4.7}$$

When the AUV is following a curve with instantaneous radius of $R, \Sigma F_t$ determines the rate of change of the magnitude of the velocity, ΣF_n changes the direction of the velocity, which gives,

$$\begin{cases} \Sigma F_t = D(V,\beta) + T\cos\beta = ma_t = m\dfrac{dV}{dt} \\ \Sigma F_n = L(V,\beta) + T\sin\beta = ma_n = m\dfrac{V^2}{R}. \end{cases} \tag{4.8}$$

On the other hand, the resultant moment for the rotation can be mathematically derived from Equations (3.12) and (3.14),

$$\sum M = M_z + M_r = \triangle T\frac{l_h{}'}{2} + C_r r^2 = I_{zz}\ddot{\psi}\,, \tag{4.9}$$

where M_z stands for the yaw moment generated by the differential thrust system, M_r represents the drag in yaw, r is the yaw rate of the vehicle, and $\ddot{\psi}$ is the angular acceleration of the AUV.

By definition, the sideslip angle is the angle between the motion of the vehicle and the direction that the vehicle is heading towards. As demonstrated in Figure 4.2, the relationship of the three angles is

$$\beta = \chi - \psi, \tag{4.10}$$

where χ is the course angle between the motion and X-axis of the G-frame and ψ represents the angle between the vehicle heading and X-axis of the G-frame.

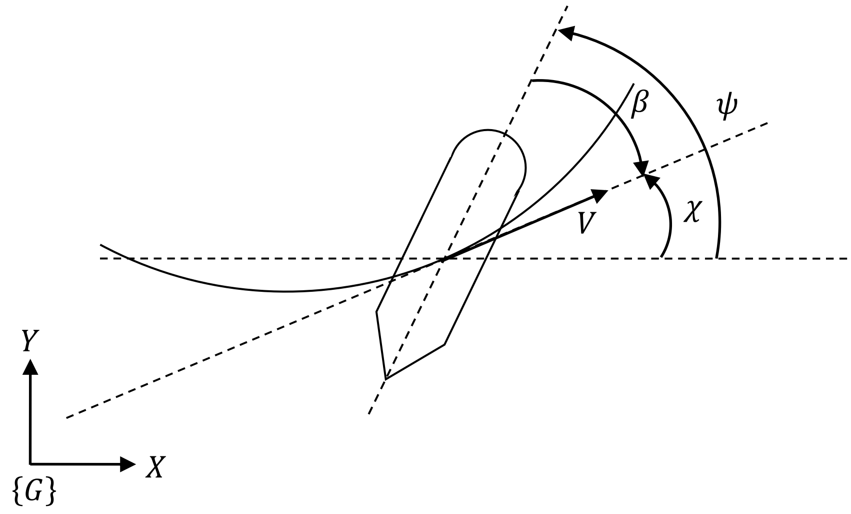

Figure 4.2: Schematic of the relationship between the sideslip angle, β, course angle, χ and the AUV heading angle, ψ.

Taking the time derivative of Equation (4.10), the relationship between the angular speed, $\frac{V}{R}$, the yaw rate, r, and the changing rate of sideslip angle yields,

$$\dot{\beta} = \dot{\chi} - \dot{\psi} = \frac{V}{R} - r. \tag{4.11}$$

Combining all the equations derived above gives,

$$\begin{cases} \dot{V} = \dfrac{T\cos\beta + D(V,\beta)}{m} \\ \dot{\beta} = \dfrac{T\sin\beta + L(V,\beta)}{m \cdot V} - \displaystyle\int_{t1}^{t2} \frac{\Delta T \frac{l_h{}'}{2} + C_r r^2}{I_{zz}} dt. \end{cases} \tag{4.12}$$

When the vehicle stabilizes at its top speed, both the rotational and translational motions are in steady state, hence

$$\begin{cases} \dot{V} = \dfrac{T\cos\beta + D(V,\beta)}{m} = 0 \\ \sum M = \triangle\, T\dfrac{{l_h}'}{2} + C_r r^2 = 0 \\ \dfrac{T\sin\beta + L(V,\beta)}{mV_{max}} = \dfrac{V_{max}}{R} \\ \dot{\beta} = \dfrac{V_{max}}{R} - r. \end{cases} \tag{4.13}$$

From Equation (4.13), it can be seen that the dynamics are nonlinear and coupled, and equations corresponding to the translational and rotational motions are summarized in Table 4.1.

Table 4.1: Dynamics equations for translation and rotation

Translation		**Rotation**
Tangential direction	**Normal direction**	
$\dot{V} = \dfrac{T\cos\beta + D(V,\beta)}{m}$	$\dfrac{V_{max}}{R} = \dot{\chi}R = \dfrac{T\sin\beta + L(V,\beta)}{mV_{max}}$	$\sum M = \triangle\, T\dfrac{{l_h}'}{2} + C_r r^2$
$a_t = \dot{V} = 0$	$a_n = \dfrac{V_{max}}{R} = \dot{\chi}R$	$\ddot{\psi} = 0$

For a particular radius of curvature, R, the sideslip angle, β, is critical to the maximum speed of the AUV. As illustrated in Figure 4.1, reducing β results in more thrust in the tangential direction – more actuation available for higher speed. Higher speed requires higher centripetal force. However, the centripetal force decreases as β reduces. This is because the centripetal force is sourced from T_n and L. Both are dependent on β – both get smaller as β reduces. The reduction in the centripetal force requires the AUV to either reduce its speed or increase the radius of curvature. To follow a particular radius of curvature, the maximum admissible speed becomes smaller. Therefore, there exists a particular β from which the maximum speed of a certain radius of curvature R can be determined.

The sideslip angle, β, is a result of the translational and rotational motion according to Equation (4.10). Therefore, the total thrust and differential thrust needs to be determined for each steady state.

In order to derive the speed limit, V_{max}, with respect to the radius of curvature, the sideslip angle, β, the total thrust, T, and the differential thrust, ΔT, are all to be determined. A numerical method was proposed in this case to derive the motion limit of the AUV. The numerical analysis was conducted using the AUV model. Details will be presented in the subsequent section.

4.3 Numerical analysis

To determine the motion limit of the under-actuated differential thrust AUV, a numerical method, namely Monte Carlo analysis, was performed using the AUV model developed in Chapter 3. In this section, the methodology will be introduced, and the results will be presented and analysed.

4.3.1 Monte Carlo method

The definition of the Monte Carlo method has not yet fully achieved consensus, but, in general, it refers to a wide range of algorithms that investigate a system numerically by feeding the system with a number of randomly selected input values, then analyses the system responses to each (Rubinstein, 2008). It is used for a large variety of mathematical and physical problems, for which the analytical solutions are difficult to obtain explicitly. Usually, for such problems, there are many parameters involved, and the relationships among these parameters are complex. In this case, the Monte Carlo method can be used to explore the internal connections among the parameters.

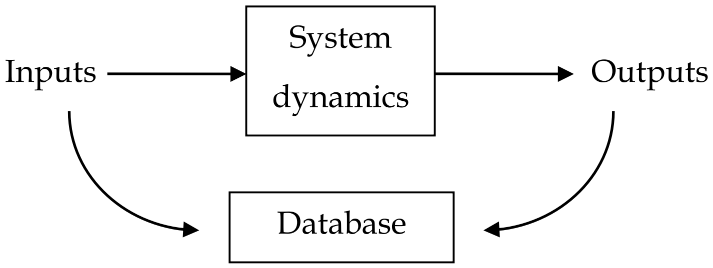

Figure 4.3: The Monte Carlo method. The system dynamics can be represented by a model for simulations or the actual system for experiments. The database is built for analysis.

The method has significant value in practice and is undertaken by repetitive simulations or experiments. As shown in Figure 4.3, the system is fed with a number of randomly generated inputs, which must be sufficiently large to capture the characteristics. Then the corresponding system responses, which are the outputs, are recorded. The relationships among any parameters of interest within the database can be estimated. To explore the motion limit of the AUV, Monte Carlo Analysis was conducted through repetitive simulations of planar motion using the AUV model. Details of the simulation will be introduced in the following section.

4.3.2 Monte Carlo analysis of the AUV model

The investigation on the AUV motion limit is specifically to establish the relationship between the maximum speed, the sideslip angle and the path curvature. As will be illustrated in Figure 4.7, the AUV is provided with a number of sets of randomly generated thrusts (T_1 and T_2). Once the AUV reaches steady state for each set of thrusts, the speed, the sideslip angle and the path curvature are all recorded and tabulated into a data pool, which is used to determine the motion limits. When studying the steady states, there are only two input settings, T_1 and T_2. A gridded space method could also be used, however it is not suitable when studying transitions. Compared with the Monte Carlo method, there is only a small difference between any two successive inputs for the gridded space method, which leads to short transition time. In contrast, the Monte Carlo method allows the study of transitions between pairs of thruster value, which can be seen from Figure 4.4 - the transition time/settling time during the Monte Carlo analysis ranges from 5 s to 35 s.

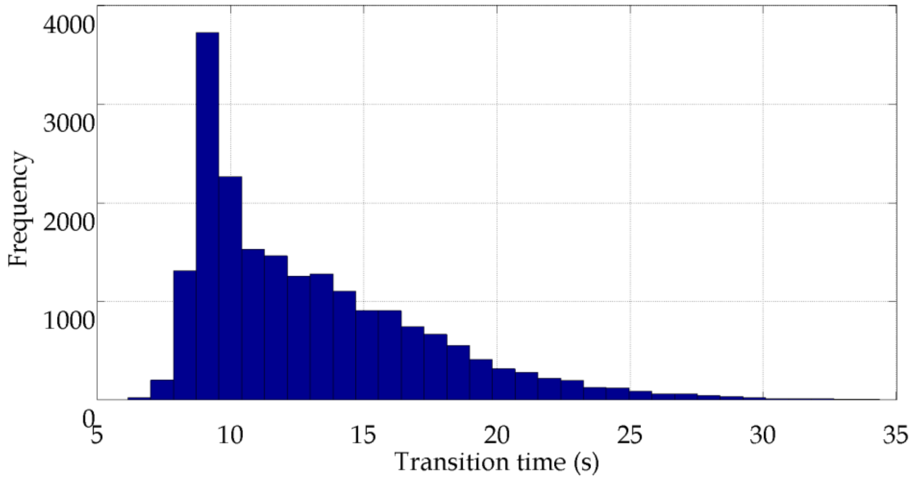

Figure 4.4: Histogram of the transition time in the Monte Carlo analysis. The transition time ranges from 6 s to 35 s.

In addition, as will be presented in Chapter 5, transitions between steady states play an important role in the path following performance in terms of time and accuracy, although the transitions will not be explored in full detail in this thesis. Therefore, the Monte Carlo method has been selected. Details of the Monte Carlo analysis will be presented next.

Figure 4.5 illustrates the simulated scenario, in which case the AUV motion is within the XY-plane under the actuation of the two thrusters on each side of the vehicle. During the simulations, 20,000 sets of thrust values were generated randomly within the thrusters' physical limit domain $[-30\text{ N} \quad 30\text{ N}]$ and were assigned to the two thrusters (T_1 and T_2) accordingly. Although larger data pool might be desirable for the analysis, relative higher computational effort is required accordingly. Despite of the limited computational capability, 20,000 sets of simulations have provided sufficient information for the analysis and acceptable computational efficiency.

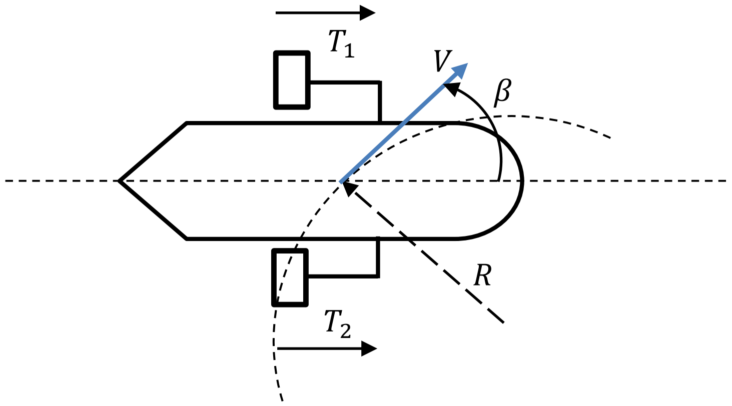

Figure 4.5: Schematic of an AUV traversing on a given path on the XY-plane. At the instant shown, the vehicle is travelling at a sideslip angle of β with the thrusters' thrusts at T_1 and T_2 respectively. The instantaneous radius of curvature of the path, also known as the turning radius is R.

As shown in Figure 4.6, thrust values for both thrusters are uniformly random, while the total thrust, T, and the differential thrust, ΔT, are both following the triangular distribution. This is expected from a mathematical point of view as the summation of two uniform distributions results in a triangular distribution. As will be demonstrated in the Monte Carlo analysis results, such a distribution of the total and differential thrust has an impact on the data points' distribution.

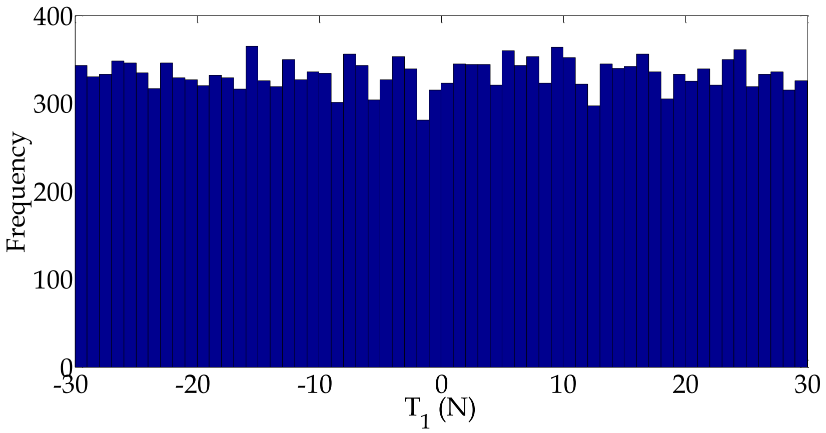

(a) Histogram of values chosen for T_1.

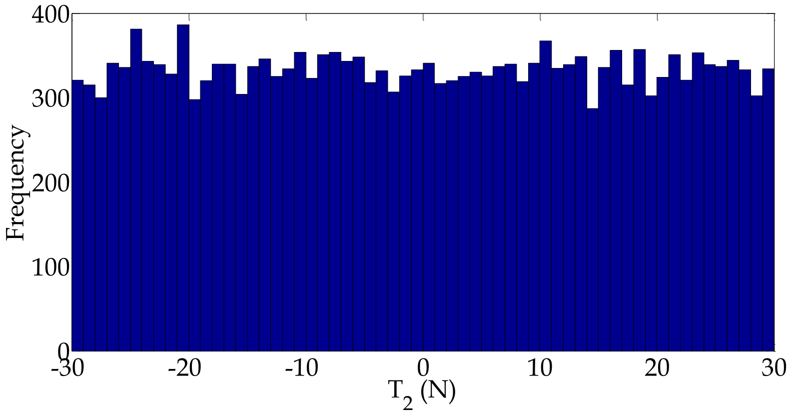

(b) Histogram of values chosen for T_2.

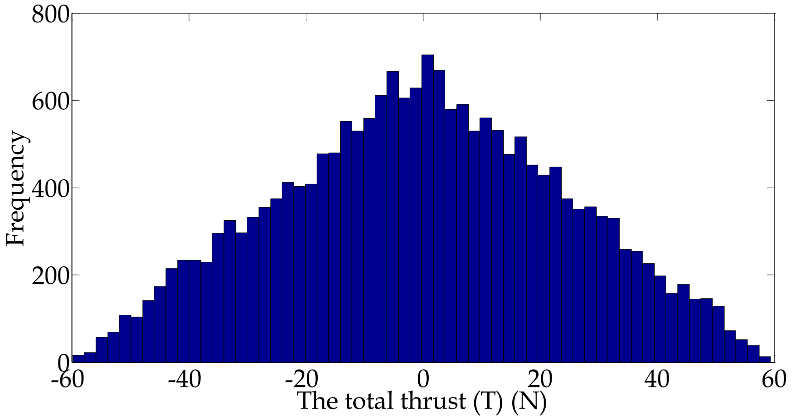

(c) Histogram of T

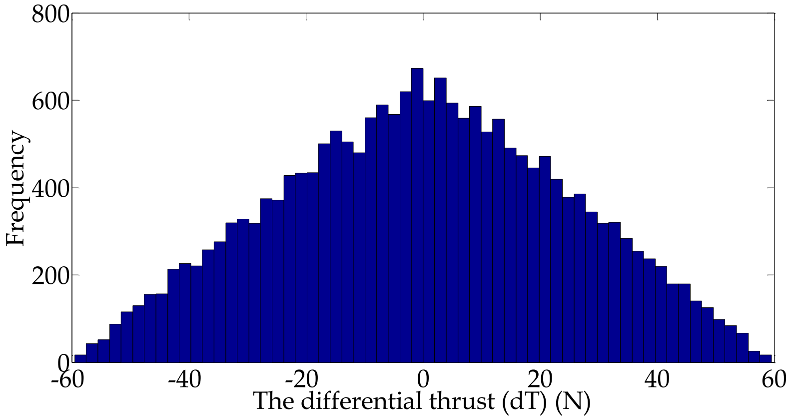

(d) Histogram of ΔT

Figure 4.6: Histogram of thrust values chosen for the two thrusters, T_1 and T_2 , and the total thrust T for the Monte Carlo analysis. The thrusts for both thrusters are generated randomly following a uniform distribution. The total thrust, T, and the differential thrust, ΔT, respectively as the summation and the difference between T_1 and T_2 demonstrates a triangular distribution.

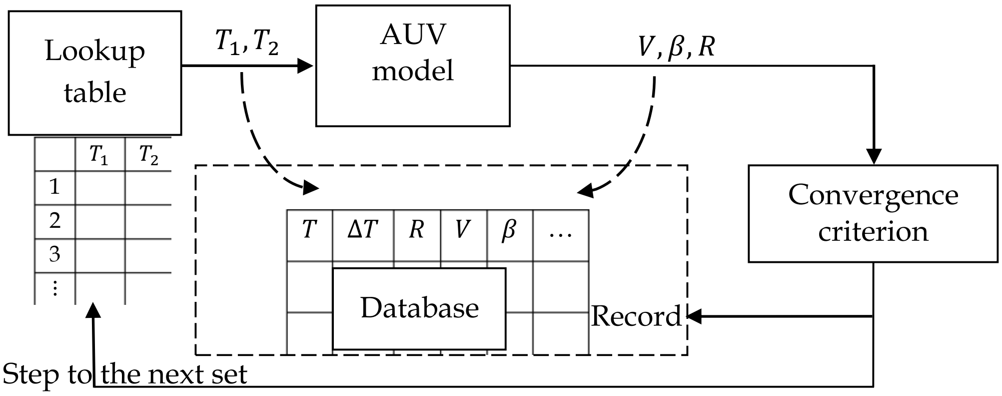

Figure 4.7: Monte Carlo simulations on the AUV model. Given the inputs of the thruster values from the lookup table in sequence, the outputs are the total velocity, sideslip angle and radius of curvature of the resultant path. These parameters and the corresponding thruster setting at steady state were all recorded into the database for analysis.

The thrusts values generated are tabulated into a lookup table of the thruster settings, as illustrated in Figure 4.7. In order to capture the AUV responses to each thruster setting, the AUV model was fed with one set from the lookup table at a time. As shown in Figure 4.7, T_1 and T_2 were assigned as the simulation started. Once the vehicle reaches steady state, the motion of the AUV: the total velocity, V, the sideslip angle, β, and the instantaneous radius of curvature of the resultant path, R, were recorded to the database.

As illustrated in Figure 4.7, a convergence criterion was designed to evaluate the convergence status by using the actual turning radius. As will be demonstrated in Appendix B, the convergence criterion is designed that the system is recognized as in steady state if the variation of the instantaneous turning radius within 3 seconds is less than 0.01 m. The duration should be sufficiently large to ensure the convergence, as larger turning radius requires longer duration. However, longer computational time comes at a cost if the duration is set to be too large. Hence, 3 seconds was eventually selected according to the system response time in different cases. Convergence triggers the data recording and alteration of thrust settings to the next set. This simulation process was repeated for the entire 20,000 sets of thruster setting. The database contains all key parameters of interest, and the analysis of these parameters will be addressed in the subsequent section, where the motion limits of the AUV are derived.

4.3.3 Results and analysis

The data collected from Monte Carlo simulations is analysed in this section. From the database, it was found that the radius of curvature R ranges from 0 m to infinity as expected. With respect of the radius of curvature, the speed and sideslip angle of interest are analysed.

4.3.3.1 Sideslip angle and speed with respect to the radius of curvature

Figure 4.8 is a scatter plot of the sideslip angle with respect to the path curvature. As shown, there exists a boundary of the sideslip angle with respect to the radius of curvature, and the trend of the boundary demonstrates a significant reduction as the radius of curvature of the path increases. In the extreme case, for a straight path, the radius of curvature reaches infinity and the sideslip angle is zero - indicating the vehicle is in the direction of the straight path. In contrast, for tighter turns with smaller radius of curvature, the AUV operates at larger sideslip angles.

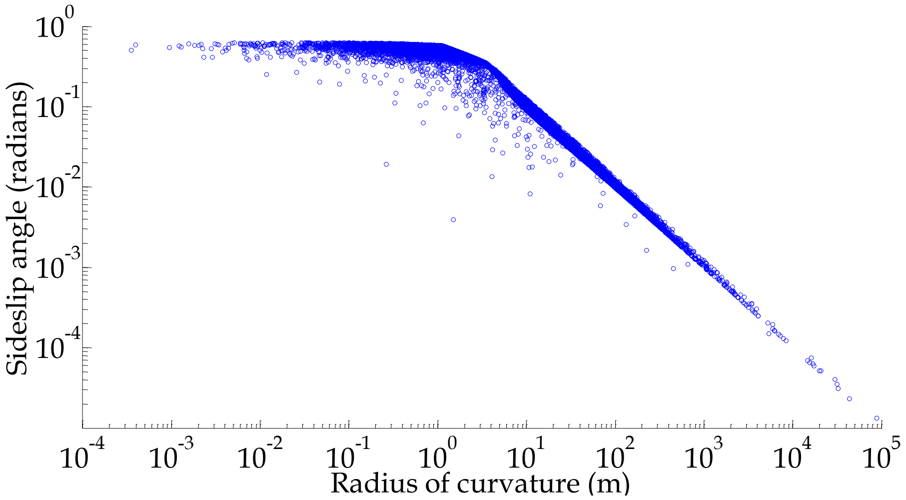

Figure 4.8: Scatter plot of the sideslip angle with respect to radius of curvature.

Figure 4.9 demonstrates the speeds of the AUV with respect to the radii of curvature of paths from the 20,000 simulations. As shown, there is a boundary of the speed with respect to the radius of curvature, which represents the maximum admissible speeds for the vehicle to follow paths with the corresponding radii of curvature.

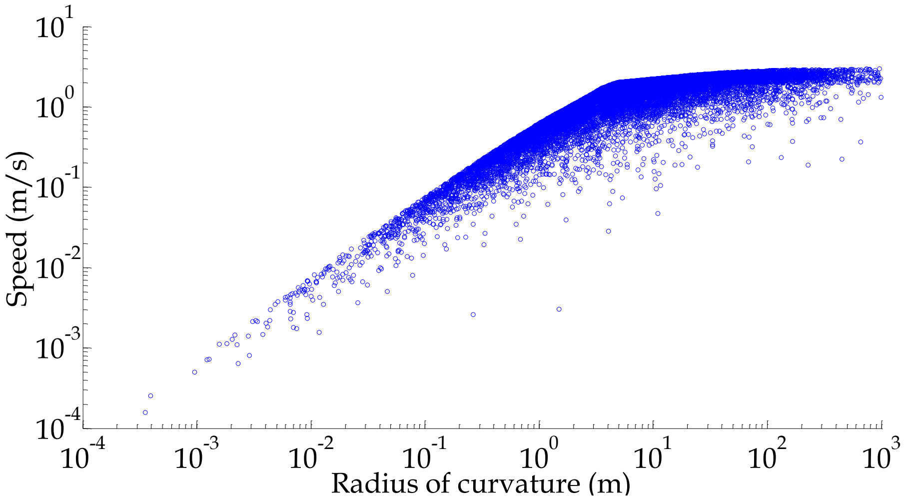

Figure 4.9: Scatter plot of the speed with respect to radius of curvature.

It can be seen that the larger the radius of curvature of the path is, the faster the vehicle can traverse on it. From a heuristic point of view, the maximum feasible speed for making a turn should be lower than it is for going straight. More importantly, this boundary outlines the region of the motion limit of the AUV, within which the speeds are admissible to guide the vehicle to follow paths with different curvatures.

The Monte Carlo analysis, therefore, provides a solution to determine the optimal feasible speed and the corresponding sideslip angle, with respect to the radius of curvature of the paths without explicitly solving the nonlinear analytical equations in Equation (4.13). The motion limits of the AUVs are therefore derived.

4.3.3.2 Motion limit with respect to the actuation

When the AUV is at its maximum speed for the corresponding radius of curvature, it was found that one of the thrusters, either T_1 or T_2, is fully engaged - operating on the maximum thrust (±30 N). In order to justify this observation, an additional 5000 simulations were performed. This analysis only involves one input setting. Therefore, as demonstrated in Table 4.2, one of the thrusters was set to be constantly on its limit while the thrust of the other one was changed at a fixed increment within the thrusters' limit range $[-30\text{ N } 30\text{ N}]$.

Table 4.2: Thrusters setting

Set number	T_1(N)	T_2(N)
1	30	-30
2	30	-29.988
3	30	-29.976
4	30	-29.964
⋮	⋮	⋮
5000	30	30

The results of the 5000 simulations are compared with the results from 20,000 Monte Carlo simulations, as demonstrated in Figure 4.10.

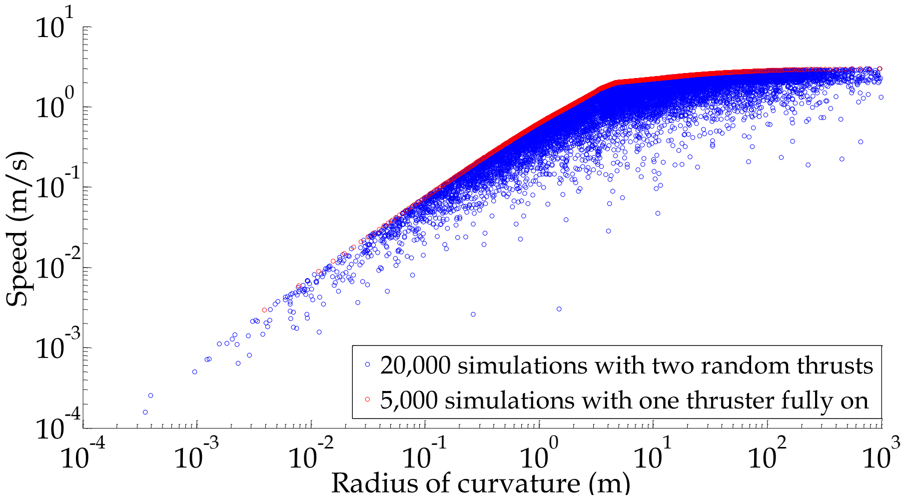

Figure 4.10: Comparison of the speeds when one of the thrusters is at its limit with the results of Monte Carlo simulations. The speeds from the 5,000 simulations (in red) are coinsident with the speed boundary of Monte Carlo results in the initial 20,000 simulations (in blue).

It can be seen that the speeds of the AUV when one of its thrusters was at its limit matches with the speed limit of the Monte Carlo results. This is due to the actuation characteristics of differential thrust system. As mentioned in Chapter 1, the actuations of the differential thrust system are the total thrust T and the differential thrust ΔT. Their saturations are dependent on the instantaneous value of each other, while the saturation of the actual actuators, T_1 and T_2, are independent. A few examples are given in Table 4.3. When the value of T is given, the maximum value of ΔT can be determined.

Table 4.3: The maximum differential thrust for given total thrust

Instantaneous T (N)	Maximum ΔT (N)
60	0
30	± 30
0	± 60
-30	± 30
-60	0

Such actuation saturation can be summarized by a constraint equation,

$$|T| + |\Delta T| = 60 \text{ N}. \tag{4.14}$$

As demonstrated in Table 4.4, when T_1 is fully on (30 N) and varying T_2, then the total thrust T and differential thrust ΔT are respectively calculated to justify Equation (4.14). The equation shows that the actuation saturation of the differential thrust system occurs when one of the thrusters, either T_1 or T_2 , is saturated – being operated on full thrust (± 30 N). Therefore, the AUV reaches its maximum feasible speed with respect to the path curvature by putting any of the two thrusters on saturation.

Table 4.4: Examples of the actuation saturation

T_1(N)	T_2(N)	T (N)	ΔT (N)	$\|T\| + \|\Delta T\|$ (N)
30	-30	0	60	60
30	-29.988	0.012	59.988	60
30	-29.976	0.024	59.976	60
⋮	⋮	⋮	⋮	⋮
30	30	60	0	60

4.4 Summary

In this chapter, the AUV motion was analysed analytically and a numerical method, the Monte Carlo method, was used to explore the motion limits of the AUV under the path curvature constraint. The results of the Monte Carlo analysis were analysed based on the actuation feature of the differential thrust system.

Most importantly, the Monte Carlo method provides a practical solution to the derivation of the motion limits with respect to the radius of curvature of the path. Guiding the vehicle to follow given paths on its motion limits ensures the time efficiency of path following without violating the capability of the actuation system. In Chapter 5, a guidance algorithm based on the motion limit will be presented.

Chapter 5

Guidance and control system

In this chapter, a curvature based guidance algorithm is presented which utilizes the motion limits derived in the Monte Carlo analysis in Chapter 4. This guidance algorithm is designed to generate motion references for time efficient path following of any arbitrary path. Motion controllers are developed to physically realise the motion references commanded by the guidance system.

5.1 An overview of the motion control system

Figure 5.1 illustrates the structure of the complete guidance and control system. The guidance system generates motion references, V_r (velocity) and ψ_r (heading angle), using the radius of curvature along given paths, R, the course angle, χ, as well as the reference position, $\boldsymbol{p}_r$, and the actual position, $\boldsymbol{p}_a$, of the AUV.

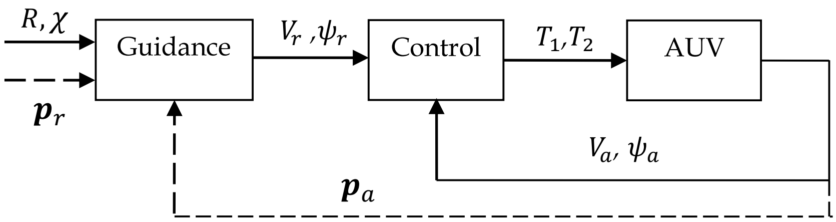

Figure 5.1: Block diagram of the AUV guidance system

The control system will generate actuations for both thrusters, T_1 and T_2, to execute these motion commands in a closed-loop fashion. Details of the guidance and control system will be introduced respectively in the following sections.

5.2 A curvature-based guidance method

As reviewed in Chapter 2, a motion control system for time efficient path following generally involves two aspects: namely traversing along the path and converging to the path (Breivik, 2010). Figure 5.2 demonstrates the motion control system in detail. The guidance consists of a traversing law and a convergence law. The traversing law generates the speed, V_r, and heading angle, ψ_r^t, (superscript t stands for the traversing law) based on the radius of curvature, R, and the course angle, χ, along the path. Compared to existing kinematic-level guidance methods, the curvature based guidance algorithm is developed from the dynamics. It takes into account the motion limits of the prototype AUV derived from the Monte Carlo analysis. Consequently, the motion references should guide the vehicle to traverse the given paths at its maximum admissible speed and to converge to the path when it deviates.

The convergence law is a steering law which outputs a correction angle, ψ_r^c, (superscript c refers to the convergence law) using the real-time deviation, $\boldsymbol{e}_p$, such that the vehicle converges to the path. The deviations are calculated by comparing the actual position of the AUV, $\boldsymbol{p}_a$, to its closest point on the reference path, $\boldsymbol{p}_r$, as $\boldsymbol{e}_p = \boldsymbol{p}_r - \boldsymbol{p}_a$.

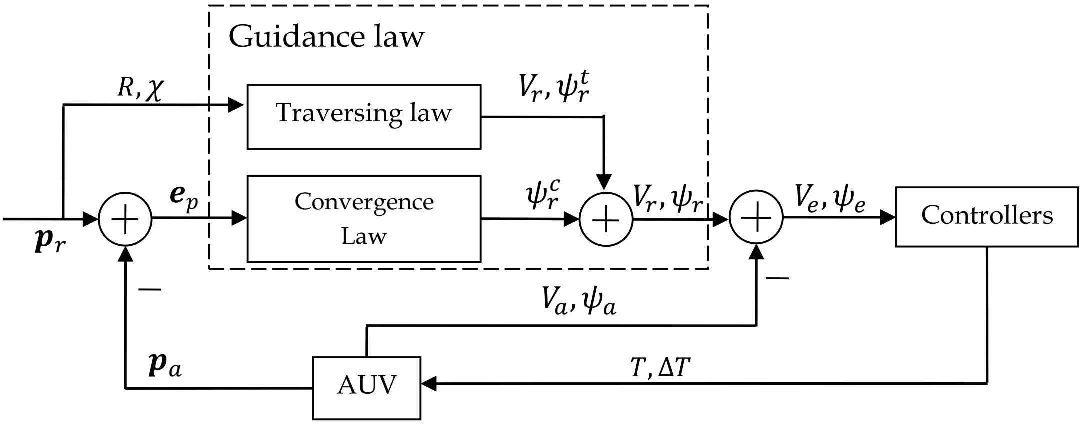

Figure 5.2: Block diagram of the guidance in a complete motion control system. Guidance system generates reference speed and heading through the traversing and convergence laws.

As a result of the traversing and convergence laws, the final speed and heading reference commands, V_r and ψ_r, are assigned. In addition, this proposed guidance algorithm is not limited by path continuity and consequently can be applied to any arbitrary path. Details of the traversing and convergence law will be presented to illustrate the guidance principle.

5.2.1 Guidance method – traversing law

Fundamentally, the traversing law generates speed and orientation references based on the Monte Carlo analysis presented in Section 4.3, which determines the motion limit of the AUV subject to the path curvature constraints using the system dynamics. An example is used to demonstrate the working principle of the traversing law in detail. Figure 5.3 demonstrates a curvature discontinuous (G^1, C^0) path, which consists of three segments with constant radius of curvature.

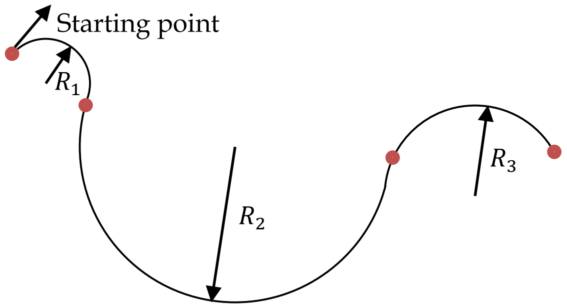

Figure 5.3: Schematic of a path. The path is curvature discontinuous and consists of three sections with constant radius of curvature, which are labeled as R_1, R_2 and R_3 respectively.

Any geometric path can be seen as a number of successive segments of constant curvatures. Based on the radius of curvature along the path, the motion limit can be determined from the Monte Carlo analysis - the values of the vehicle's maximum speed and the corresponding sideslip angle for each radius of curvature can be derived. As illustrated in Figure 4.7, the Monte Carlo analysis results are tabulated into a lookup table containing the radius of curvature, R, the speed, V, as well as the sideslip angle, β. Once the radius of curvature along the path is given, the corresponding speed and sideslip angle are interpolated using the lookup table.

Given the path in Figure 5.3, profiles of the radius of curvature, speed and sideslip angle are demonstrated in Figure 5.4 (a), (b) and (c) respectively.

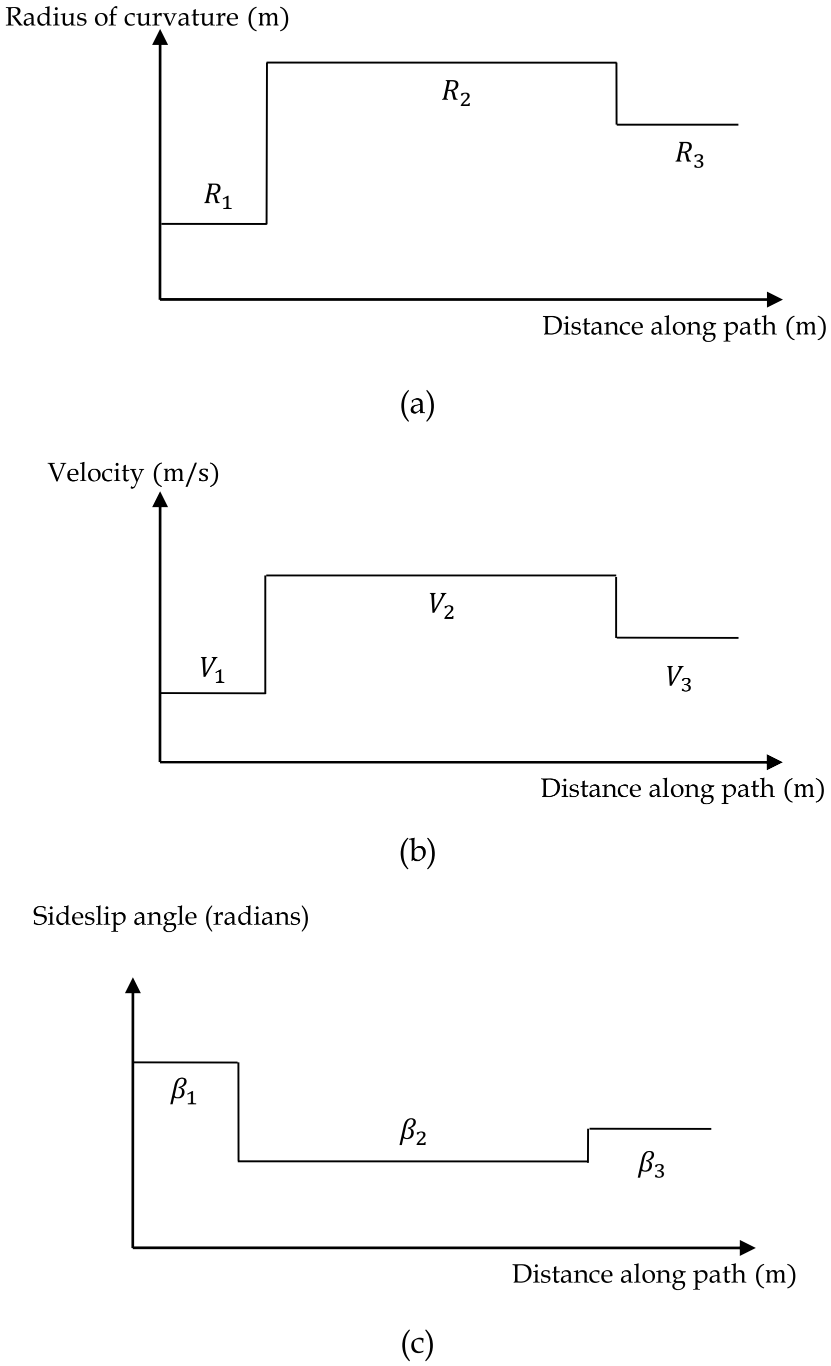

Figure 5.4: (a) Radius of curvature: R_1, R_2 and R_3 (b) The speed limit: V_1, V_2 and V_3 (c) The sideslip angle: β_1, β_2 and β_3, of each section along the path based on Monte Carlo analysis.

Based on both the sideslip angle, β, and the course angle, χ, - given in Figure 5.5 (a), heading angle, ψ, of the vehicle along the path can be derived by Equation (4.10) as plotted in Figure 5.5 (b).

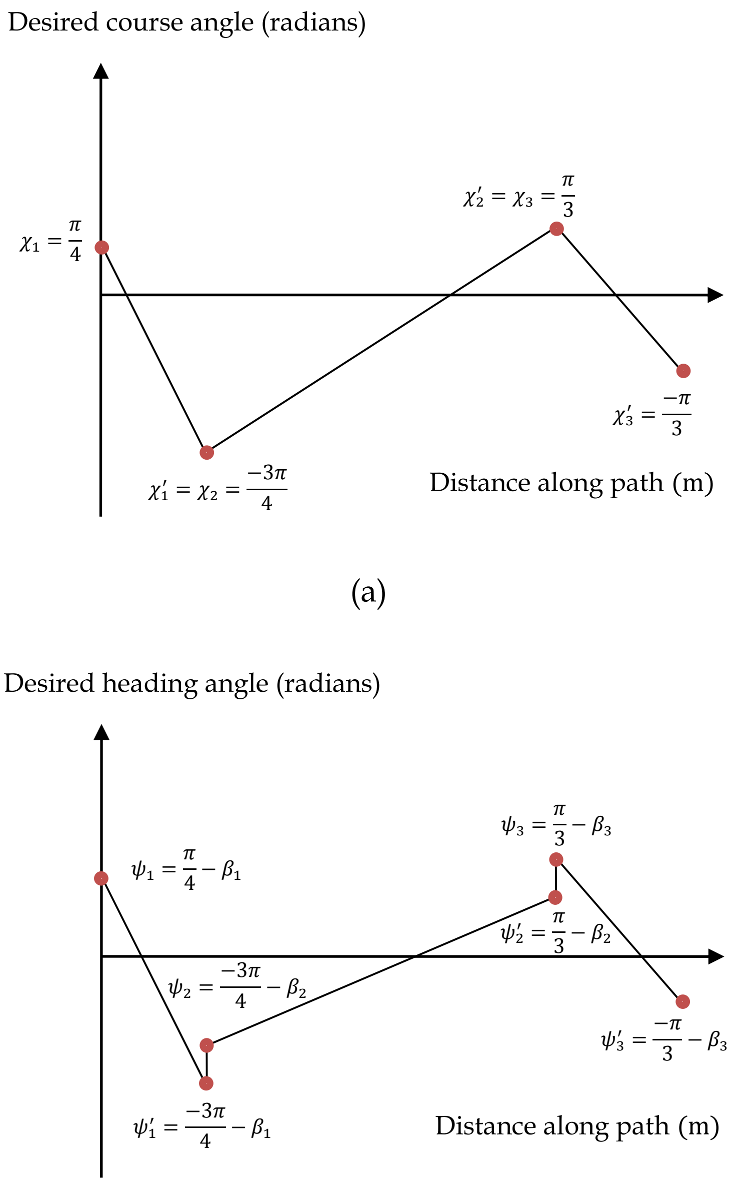

(a)

(b)

Figure 5.5: Course angle and heading angle along the given path. (a) Course angle, χ, of the path (b) Heading angle, ψ, of the path.

The traversing law is suitable for any path regardless of the path continuity. As long as the path to be followed is parameterized with respect to the radius of curvature and the course angle along it, which can both be easily obtained, motion references along the path can be determined.

As demonstrated in Figure 5.4 (b) and Figure 5.5 (b), it can be seen that the motion reference profiles of the speed and the heading angle generated using the traversing law contain step changes due to the curvature discontinuities in the path. However, such step changes in AUV motion are not feasible in practice, and hence results in inevitable path deviations. Therefore the guidance system needs to be capable of accounting for the deviations and the convergence law is developed.

5.2.2 Guidance method – convergence law

As explained in the literature review, guided convergence to the path is achieved by assigning steering laws (Breivik, 2010). The steering law is to determine the heading angle for the vehicle to eliminate deviations. Recalling the LOS (Line of Sight) guidance method reviewed in Chapter 2, the course angle is dependent on the deviation, also known as the cross track error. The LOS method highlights an intuitive principle that deviations can be corrected by steering the AUV towards the intended path. For example, as shown in Figure 5.6, the AUV always needs to steer towards the path for convergence.

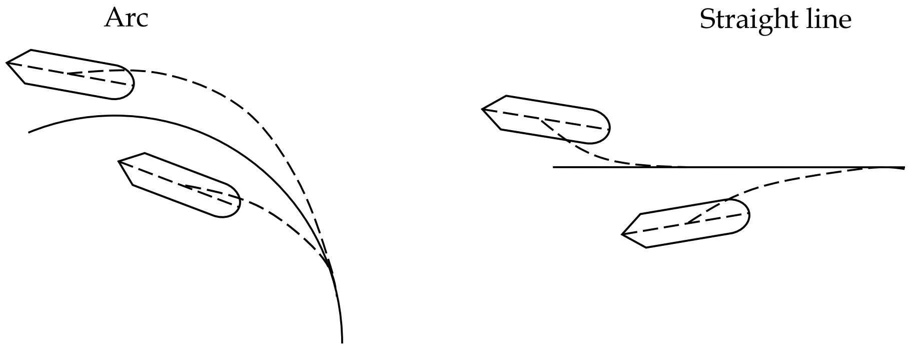

Figure 5.6: Typical examples of AUV converging to arc and straight line. The dotted lines represent the paths of the AUV converging to the reference paths (the solid lines).

In this research, a simple yet effective convergence law is developed according to this principle. The convergence law produces a correction on the heading angle based on the relative position between the actual position of the vehicle and its nearest position on the path.

Giving the manifold of waypoints on the path by $\{\boldsymbol{p}_r^i, i = 1 \cdots n\}$, the relative position vector between the actual position of the AUV and any waypoint on the path can be determined by

$$\boldsymbol{e}_p^i = \boldsymbol{p}_a - \boldsymbol{p}_r^i = \begin{bmatrix} x_a - x_r^i \\ y_a - y_r^i \end{bmatrix}, i = 1 \cdots n \tag{5.1}$$

Therefore, the nearest waypoint can be found through determining the shortest position vector, hence the deviation of the AUV from the path can be decided:

$$|\boldsymbol{e}_p| = (\min_{i=1\cdots n} |\boldsymbol{e}_p^i|)\,. \tag{5.2}$$

For planar paths, the shortest relative position vector $\boldsymbol{e}_p$ can be represented by its two components in the body coordinate system $\{B\}$. These components are obtained by transforming the position errors in the global coordinate system into the local body fixed coordinate system as:

$$\boldsymbol{e}_p = \begin{bmatrix} e_x \\ e_y \end{bmatrix} = \begin{bmatrix} \cos\psi & \sin\psi \\ -\sin\psi & \cos\psi \end{bmatrix} \begin{bmatrix} x_a - x_r \\ y_a - y_r \end{bmatrix}. \tag{5.3}$$

The sign of the y-component of deviation, e_y, can be used to determine the relative position of the path to the vehicle. As demonstrated in Figure 5.7, there are two paths locating to the right and left of the AUV respectively. The actual position of the AUV, $\boldsymbol{p}_a$, is represented by the marker in red in the figure and its nearest positions on the two paths, denoted by $\boldsymbol{p}_r^{min}$, are marked in yellow. Deviation, $\boldsymbol{e}_p$, is resolved into e_y and e_x in the body coordinate system. The component, e_y, is negative when the path is on the left and is positive when the path is on the right.

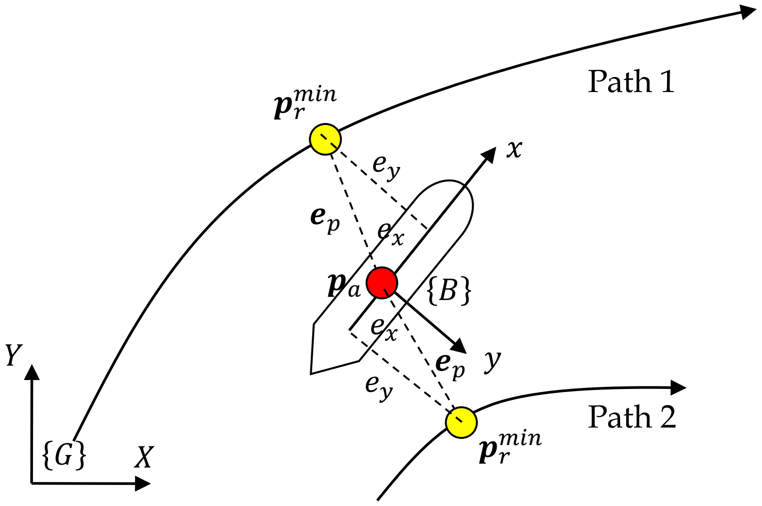

Figure 5.7: Diagram of relative positions of the path to the AUV and sign of the deviation. The sign of e_y is determined by the relative position between the path and the AUV in the body coordinate system.

In order to converge to the desired path, with regard to the top view in Figure 5.7 above, the vehicle needs to rotate anticlockwise when the path is located to its left and rotate in the clockwise direction when the path is to its right. Therefore the steering angle due to deviations is determined by

$$\psi_r^c = \mathrm{sign}(e_y) k_e |\boldsymbol{e}_p|, \tag{5.4}$$

where k_e is used to modify the steering rate for the convergence. The larger k_e is, the more aggressive the steering action is, and thus the quicker convergence will be achieved. However, the system could become unstable if the value is too large. Therefore, a desirable k_e allows effective convergence without pushing the system into unstable condition. Overall, the convergence law operates in a closed loop manner, where the AUV deviation is monitored and eliminated in real-time.

In combination with the traversing law developed in Section 5.2.1, the proposed guidance method generates speed and heading commands for the AUV to follow any arbitrary paths in a time efficient manner.

5.3 Motion controllers design

In order to execute the speed and heading commands generated from the guidance system, motion controllers need to be developed. In this section, a motion control system with two controllers is developed, based on a review of existing control laws for AUVs. The rationale of the controller design will be presented.

5.3.1 PID controller fundamentals

As analyzed in the literature review, PID controllers are commonly used in practice due to their simplicity. In this research, PID controllers are also selected to realize the commanded speed and heading from the guidance system. The controller mechanism of a typical PID controller is demonstrated in Figure 5.8, where y_r is the reference signal, y_a is the actual output from the system, y_e is the error between the reference and output, and u is the controller output.

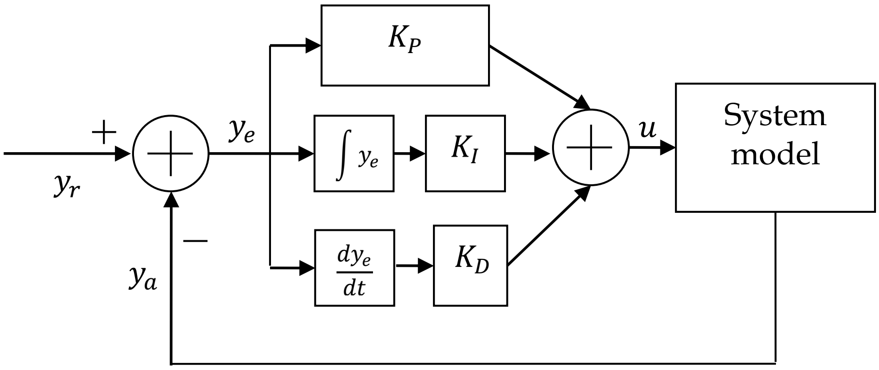

Figure 5.8: Block diagram of a closed loop PID controller

The terms, K_P, K_I and K_D are respectively the gains of the Proportional, Integral and Derivative of the PID controller. K_P acts on the present error, K_I focuses on the accumulative effect of the error within a previous period of time, while K_D accounts for the changing rate of the error and intended to prevent potential error in the future (Bloch, 2003). All of the three gains can be tuned for different control purposes. Details of the motion controllers, including their gains and response for step inputs, will be presented in Chapter 6.

5.3.2 Motion controllers

Two decoupled PID controllers are developed for speed and heading control. Figure 5.9 (a) illustrates the speed controller and heading controller, and how they operate with the guidance system.

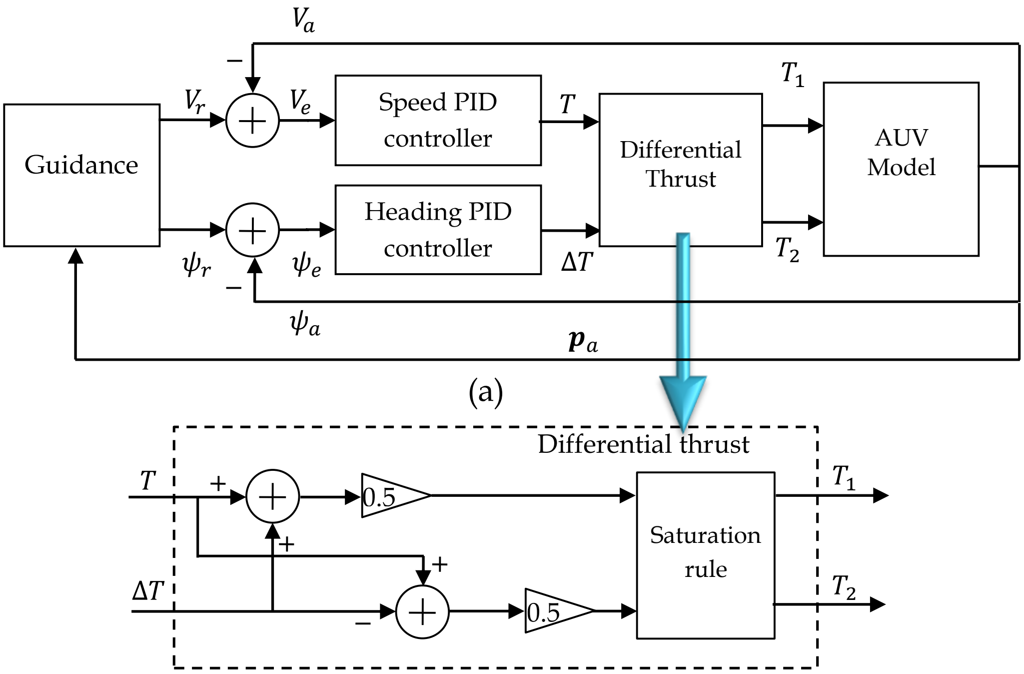

Figure 5.9: Block diagram of the speed and heading controllers. As shown in (a), the speed control loop and heading control loop work in parallel to generate thrust, T, and differential thrust, ΔT, to eliminate the speed and heading errors, while the upper level guidance generates commanded speed and heading signals to follow the reference paths time efficiently. In the "Differential thrust" block in (b), the thrusts required are calculated, and then assigned to the two thrusters to execute.

While the AUV is following a given path, the position ($\boldsymbol{p}_a$) of the AUV is monitored and fed back to the guidance system. The guidance system uses the actual position to locate the nearest point on the path to the AUV. The current radius of curvature of the path at this nearest point and the current deviation of the AUV are used in the guidance system to determine the desired speed (V_r) and heading (ψ_r) for time efficient path following. The speed controller takes the desired speed signal and compares it with the actual AUV speed (V_a). If there is a difference between the actual and desired speed of the AUV, the speed controller eliminates the error (V_e) by applying thrust (T). The heading controller operates based on the same principle as the speed controller. It monitors the real-time heading error (ψ_e) of the AUV and applies a steering torque (ΔT) to achieve the desired AUV heading.

As shown in Figure 5.9 (b), the differential thrust block is used for allocating the thrusts of the two thrusters. In general, the control allocation for the actuation system determines the action required for each, and constraints such as saturation need to be considered. For over-actuated systems (there are more actuations than the degrees of freedom), allocation of the actuation can result in an optimization problem, for example, minimum power consumption (Fossen, 1994). The prototype AUV is under-actuated, and the required thrust, T, and differential thrust, ΔT, can not be executed directly by the differential thrust system. Therefore, the actuation allocation is a problem of determining a function to map T and ΔT into the required thrust values, T_1 and T_2, by the two thrusters. As illustrated in Figure 5.9 (b) of the differential thrust block, the function developed consists of the following rules:

$$\begin{cases} T_1 = \frac{T+\Delta T}{2} \\ T_2 = \frac{T-\Delta T}{2}. \end{cases} \tag{5.5}$$

Another rule embedded in the function is a saturation algorithm, which compares the required thrust forces, T_1 and T_2, with the maximum thrust force of the thrusters, T_{max}. $T_{max} = 30\ \mathrm{N}$ here for the ones used on the prototype AUV (SeaBotix BTD 150, refer to Appendix C). Whenever the magnitude of T_1 or T_2 exceeds the physical limits of the thrusters, the motion required exceeds the capability of the actuation system, the corresponding thruster will be put on full thrust of $30\ \mathrm{N}$. When saturation occurs, there is only one degree of freedom left, which means, the speed and heading control cannot be both achieved at the same time. Therefore, the system will prioritize the heading control to ensure the AUV stays on/converges to the path. In Chapter 6, the performance of the proposed algorithm is evaluated through simulations.

Chapter 6

Guidance based path following

In this chapter, simulations of the AUV following an arbitrary path with curvature discontinuities and a lawn mower path are presented, and the path following performance will be analysed to demonstrate the effectiveness of the proposed guidance and control algorithm.

6.1 Path following of an arbitrary path

Firstly, the AUV following an arbitrary path was simulated. As the proposed guidance method is not limited to curvature continuous paths, the reference path is designed to be curvature discontinuous. In addition, the proposed method doesn’t have constraints on the radius of curvature, so the reference path consists of both line segments and arc segments with a variety of path curvatures. As shown in Figure 6.1, the path is divided into 14 segments, and the radius of curvature of each segment is summarized in Table 6.1. In fact, any path can be represented by a succession of lines and arcs. Moreover, different transitions have been included in this reference path, such as transitions from arc segment to line (ATL), from line to arc (LTA), as well as arc to arc (ATA). In regard to the path resolution when constructed in Matlab, 0.01 m was selected for the straight segments and $\frac{\pi}{720}$ radians (approximately 0.25°) for the arc segments.

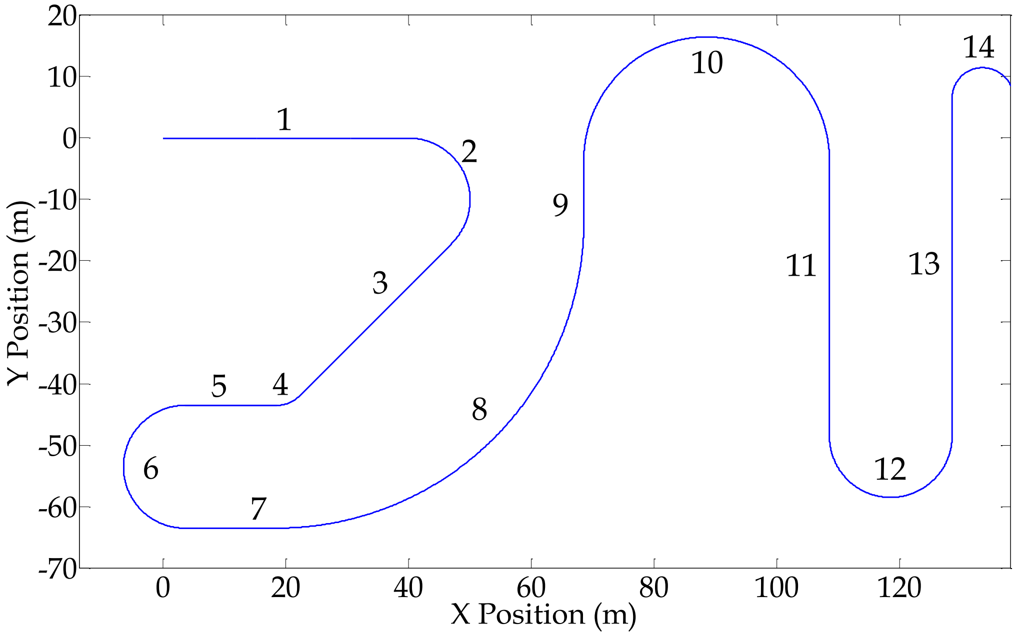

Figure 6.1: An arbitrary path to be followed by the AUV. The path can be divided into 14 line segments and arc segments with constant radius of curvature.

Table 6.1: Segments of the arbitrary path plotted in Figure 6.1.

Segment	Type	Radius of curvature R (m)
1	Line	∞
2	Arc	10
3	Line	∞
4	Arc	5
5	Line	∞
6	Arc	10
7	Line	∞
8	Arc	50
9	Line	∞
10	Arc	20
11	Line	∞
12	Arc	10
13	Line	∞
14	Arc	5

Due to the complexity of the highly nonlinear system dynamics of the AUV, systematic tuning is not applicable to determine the control parameters. Therefore, the parameters used in the current controllers were manually tuned based on trial and error. Gains of the motion controllers, a speed controller and a heading angle controller, used in the simulations are listed in Table 6.2, and the definitions of the parameters have been introduced in Figure 5.8. As can be seen from Table 6.2, the resultant tuned controllers are respectively a PI controller for speed control and a P controller for heading angle control. Although the gains listed in Table 6.2 may not represent the optimum controller settings, further controller optimization is out of the current research scope and can be extended into a potential research direction in the future (refer to the future work in Chapter 7). In addition, the scaling factor $k_e = 0.4$ was used, which decides the steering rate for path convergence as discussed in the convergence law in Equation (5.4). As will be demonstrated, the combination of parameters can be justified by the system performance through the system response analysis of the simulation results.

Table 6.2: Gains of the speed and heading controllers

	Speed controller	Heading controller
K_P	1000 (Ns/m)	5000 (N/radians)
K_I	600 (N/m)	0
K_D	0	0

Firstly, the performance of the two motion controllers are analyzed. Figure 6.2 and Figure 6.4 respectively show the system responses to step inputs of speed and heading angle, while the thrusters' behavior is illustrated in Figure 6.3 and Figure 6.5. In Figure 6.2, the red dashed and green dotted lines show that the AUV accelerates from stationary to the commanded reference speeds of $3\ \mathrm{m/s}$ and $1\ \mathrm{m/s}$, and the reference speeds are represented by the blue solid line and the pink dash-dot line.

It can be seen from the results that the time taken for the AUV to accelerate to its maximum speed on a straight line is approximately 2.5 seconds. This is consistent with the settling time of the simulated result in Figure 3.13 for the scenario of translational acceleration using full thrusts for both thrusters. In correspondence to the thrusters' behavior in Figure 6.3, equal thrusts from the two thrusters are used ($T_1 = T_2$) for both cases, as no differential thrust is needed for pure translational motions. A difference in the responses to different reference speeds (3 m/s and 1 m/s) can be observed with slight overshoot in the 1 m/s case. When the reference speed is 3 m/s – the top speed of the AUV, the actual speed of the AUV (the red dashed line in Figure 6.2) cannot exceed this value, and both thrusters are operated on their maximum capability at all time. Whereas in the case with the reference speed of 1 m/s, the AUV initially accelerates with maximum thrust, then there is a slight overshoot, which brings the thrusts down to 4.4 N. As fixed gains are used in this highly nonlinear plant, the performance varies at different operating points of the system. Designing a more sophisticated controller could improve the performance, but it is out of the research scope.

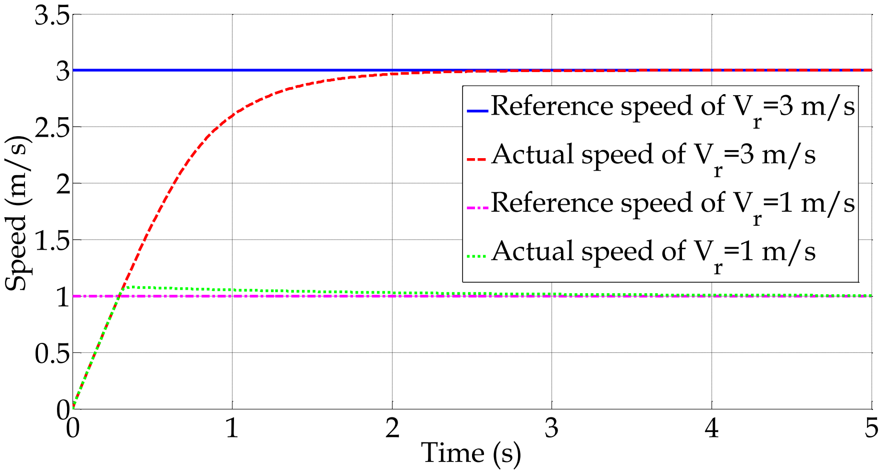

Figure 6.2: System response to step speed commands. The reference speeds are respectively 3 m/s and 1 m/s, which are represented by the blue solid line and pink dash-dot line. Correspondingly, the red dashed and green dotted lines are

the actual speed responses of the AUV. In both cases, the AUV accelerates from stationary.

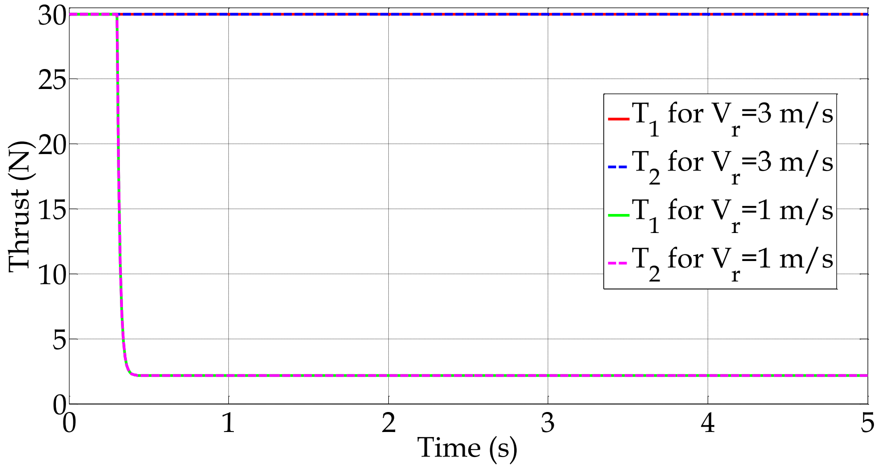

Figure 6.3: Thrusters response to step speed command (shown in Figure 6.2). Both thrusters are operated on full thrust (30 N), represented by the red solid and blue dashed lines, when the reference speed is 3 m/s. When the reference speed is 1 m/s, the thrusters are initially on their maximum for maximum acceleration, and then the total thrust is reduced to 4.4 N to regulate the AUV to the desired speed. Equal thrust is used in both thrusters for the pure translational acceleration.

The heading angle response is illustrated in Figure 6.4. It can be seen that the system is an inherently heavily damped plant. Hence, no derivative gain is needed in the heading angle controller. Additionally, as shown in the actual heading angle response (represented by the red dashed line), the response time for the AUV to steer to the commanded heading angle of π radians (180°) is about 5.5 seconds, and the yaw speed gradually reaches a constant rate (approximately 0.8 rad/s by taking the slope of the red dashed line). This is consistent with the earlier results in Figure 3.14, where the AUV rotates using the maximum differential thrust. As expected, from the thrusters' behavior illustrated in Figure 6.5, it can be seen that the thrusters were initially operated on their physical limits before the AUV rotates to the desired heading angle. The thrusts of the two thrusters are always equal and opposite ($T_1 = -T_2$), in order to accomplish the commanded pure rotational motion.

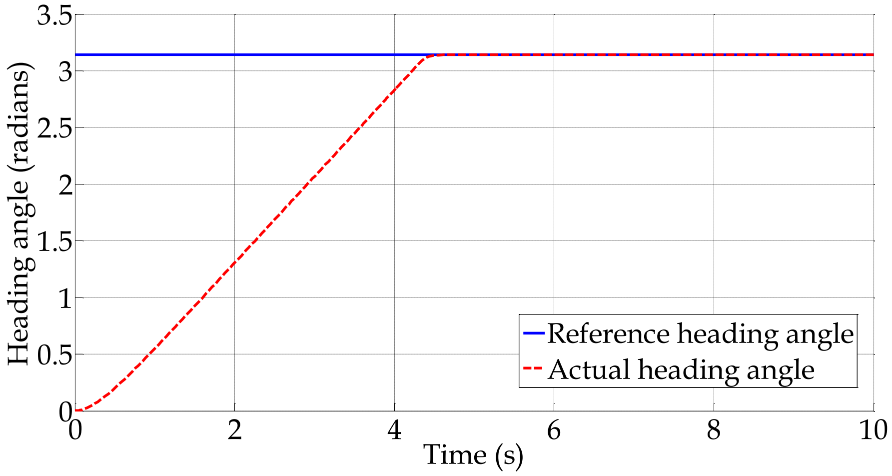

Figure 6.4: System response to step heading angle command. The blue solid line is the commanded signal, and the red dashed line represents the actual heading angle. The system is heavily damped, and it takes the AUV approximately 5.5 seconds to steer to the reference heading angle of π radians from stationary. The yaw rate is a constant (approximately 0.8 rad/s) when the AUV reaches steady state.

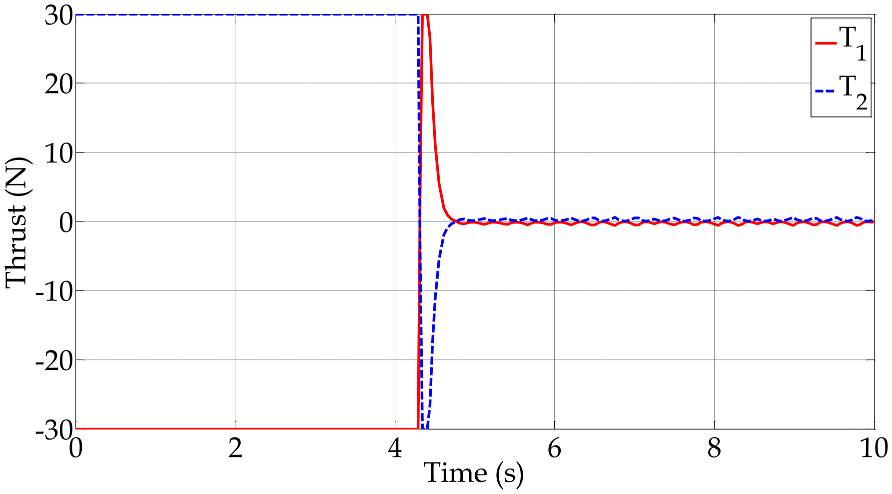

Figure 6.5: Thrusters behavior for the rotational motion (shown in Figure 6.4). During the initial 4.3 seconds, both thrusters are operated on their physical limit for maximum angular acceleration. Then thrusts are reduced to achieve the commanded heading angle. Thrusts are equal and opposite for a pure rotational motion.

Next, the results of the simulated path following of the AUV on the arbitrary path are presented. The actual path of the AUV and the reference path are demonstrated in Figure 6.6. As shown, the actual path traversed by the vehicle is represented by the red dashed curve and the blue solid curve is the reference path. Through the comparison between the actual path and the reference path, it can be seen that the AUV traversed along the reference path using the proposed guidance and control system.

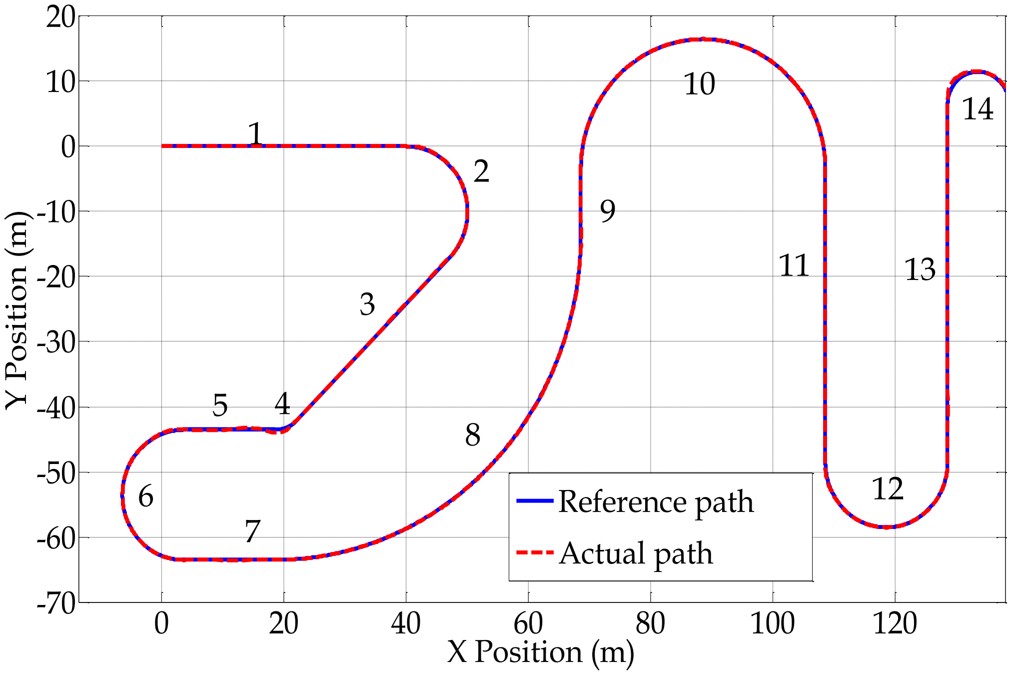

Figure 6.6: An arbitrary reference path (shown in Figure 6.1) and the actual path following trajectory. The reference path is curvature discontinuous and is made of tangentially-connected arcs and lines.

In addition, error analysis is performed. Figure 6.7 is a histogram of the deviations during path following, which includes 4489 data points in total. The deviation is calculated by comparing the actual path and the reference path. It was found that most deviations, around 55.6% of the total, are concentrated in the region within 0.05 m. The largest deviation during path following is below 0.5 m.

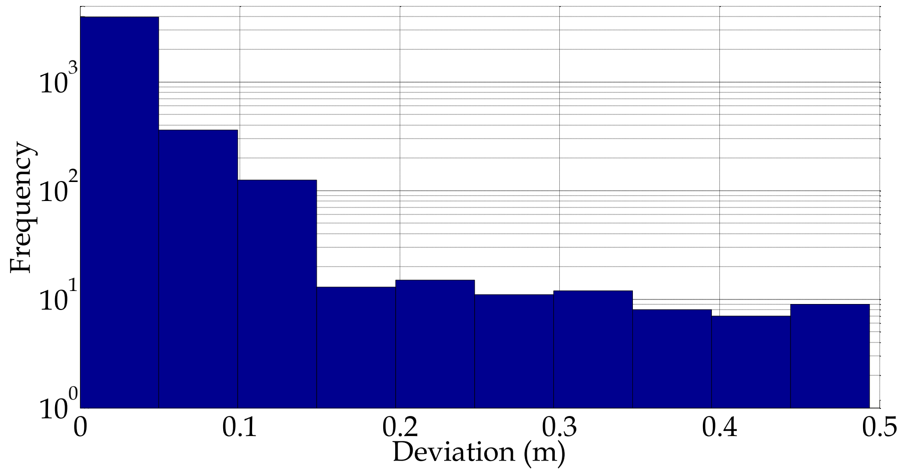

Figure 6.7: Histogram of deviations during path following of the arbitrary path. There are 4489 data points in total. Most data points (55.6%) are within 0.05 m and the maximum deviation is less than 0.5 m.

Besides the error analysis from a statistical point of view, the real-time deviations during path following are analysed in Figure 6.8. As demonstrated, the deviation of the AUV is plotted with respect to time. In order to correlate deviation of the AUV to each segment of the path, the deviations are labelled as illustrated in the figure.

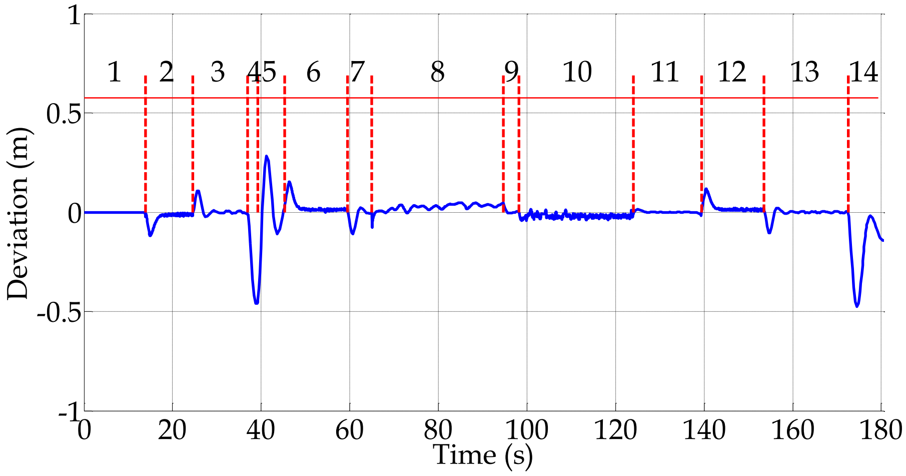

Figure 6.8: Deviations during path following on the arbitrary path. From the real-time deviations of the AUV on each segment, relatively large deviations are found during transitions between two segments and are under 0.5 m.

The real-time position of the AUV during path following is also recorded, from which the starting and ending time of each segment along the path are identified. Information on each segment's radius of curvature, timing of the AUV entering and exiting each segment, as well as the overall traversing time for each segment are summarised in Table 6.3.

Table 6.3: Starting and ending time for each segment of the path during path following. Relatively large deviations observed in Figure 6.8 are found during the transitions between the segments highlighted in yellow, where the AUV moves from a straight line segment to an arc segment.

Segments	Radius of curvature, R (m)	Starting time, t_s (s)	Ending time, t_f (s)	Traversing time (s)
1	∞	0.0	13.9	13.9
2	10	13.9	24.8	10.9
3	∞	24.8	36.9	12.1
4	5	36.9	39.2	2.3
5	∞	39.2	45.3	6.1
6	10	45.3	59.5	14.2
7	∞	59.5	65.0	5.5
8	50	65.0	94.7	29.7
9	∞	94.7	98.2	3.5
10	20	98.2	124.0	25.8
11	∞	124.0	139.4	15.4
12	10	139.4	153.5	14.1
13	∞	153.5	172.5	19.0
14	5	172.5	180.7	8.2

From Figure 6.8 and Table 6.3, it can be seen that deviations occur at the intersection point of two adjacent segments, where the AUV transients between lines and arcs. The largest deviations are observed in transitions from Segment 3 to 4 and from Segment 13 to 14. According to Table 6.3, in both cases highlighted in yellow, the AUV decelerates to transient from a line segment to an arc segment with $R = 5$ m. As will be discussed further in the following paragraphs, higher position errors are expected because larger changes in the path curvature induces larger step changes in the commanded speed and heading angle, and the AUV deviates once the commanded signals cannot be tracked. Nevertheless it can be seen from the results that the deviation is compensated effectively using the proposed guidance method.

Some small chattering can be observed in the deviation signal in Figure 6.8 (i.e. Segment 10). This corresponds to the action of the convergence algorithm to eliminate the deviation of the AUV. As discussed in the methodology in Chapter 5, the steering command generated by the convergence law is linear with respect to the deviation distance. This can be seen from Figure 6.9. The final heading reference is different from the heading reference generated by the traversing law reflecting the response of the convergence law to the deviation.

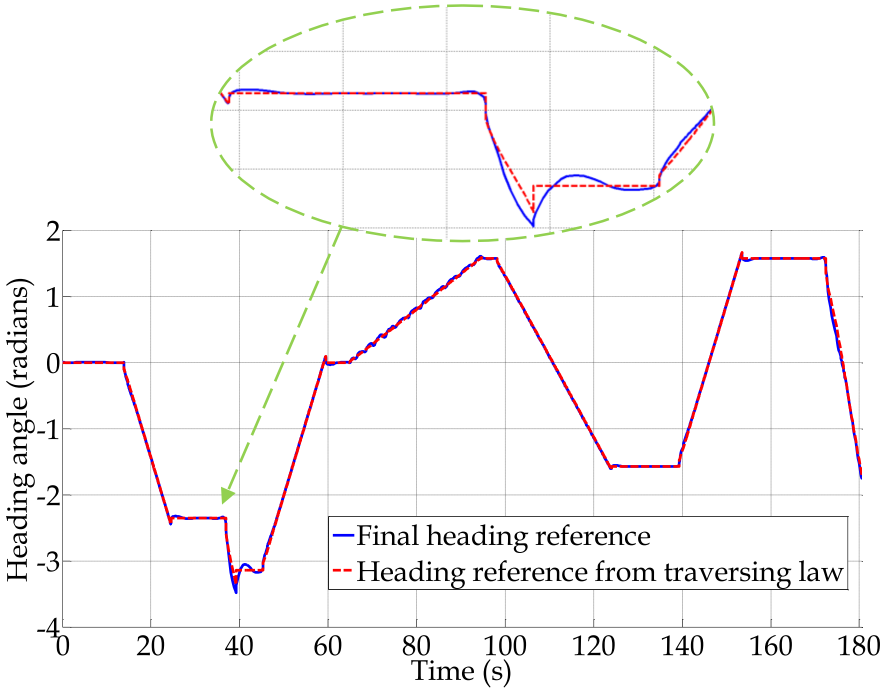

Figure 6.9: Reference heading angle of the AUV during path following. The reference heading angle from the traversing law (red dashed line) is compared with the final reference heading angle (blue solid line).

As illustrated in Figure 6.9, the reference command from the traversing law (in red) contains step changes due to the curvature discontinuities on the path at the intersections between two segments. Such step changes are physically infeasible for the AUV to achieve. Therefore, the AUV inevitably deviates from the path. As highlighted in the figure, a variation between the final heading angle command (the blue solid line) and the reference from the traversing law (the red dashed line) was observed. This is expected since the convergence law will become active to reduce the position error by steering the AUV towards the path as soon as deviation is detected. The final heading command changes as a result.

The AUV is guided with the final heading reference, and the actual tracking response of the vehicle during path following is analysed. The command signal (the blue solid line) is compared with the actual heading angle (the red dashed line), as illustrated in Figure 6.10. Through the comparison, it can be seen that the reference heading angle is tracked by the AUV.

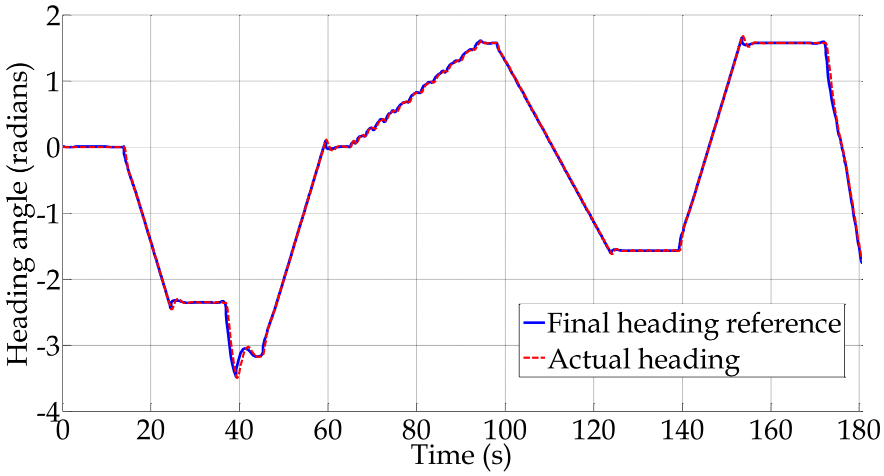

Figure 6.10: Heading response of the AUV during path following. The actual heading angle is compared with the reference heading angle. The blue solid line represents the final reference heading angle (shown in Figure 6.9) and the actual heading angle is the dashed line in red.

The speed response of the AUV is analysed. As shown in Figure 6.11, the blue solid line represents the reference command, which outlines the speed limit for following the given path. As introduced in the methodology chapter (Section 5.2.1), the speed reference is generated based on the Monte Carlo analysis - for a given radius of curvature, the speed can be determined using the look-up table (Figure 4.7). The reference speed from Monte Carlo analysis is the maximum admissible speed of the AUV to achieve time efficient path following.

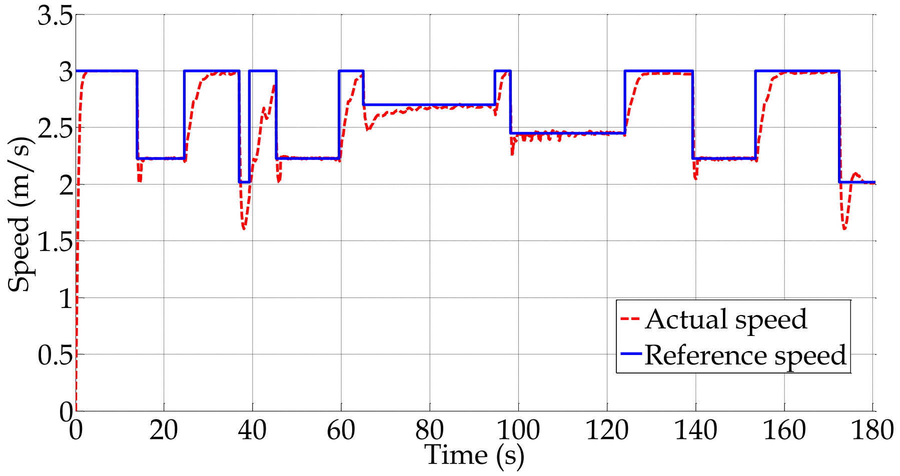

Figure 6.11: Speed response of the AUV during path following. The actual speed is compared with the reference speed. The blue solid line represents the reference speed generated from the traversing law, and the actual speed is in red.

The comparison between the reference speed (the blue solid line) with the actual speed (the red dashed curve) shows that the speed command has been tracked. The variations between the two within the transition periods are expected. Similar to the heading response, the instant change in the speed command signal is also practically infeasible and will cause deviation, which in turn affects the speed tracking performance as a result of the limitation of differential thrust manoeuvring systems. For example, when the AUV enters or exits from one segment of the path to the next, deviation occurs because of the instant change in the reference signal. Due to the deviation, the convergence law needs to recalculate the heading angle for the AUV to get back on track. The steering requires additional actuation – more differential thrust for rotation. This causes a reduction in the availability of the total thrust for propulsion, which eventually leads to the degradation in the speed tracking performance.

As mentioned earlier in Chapter 4, the capability of a differential thrust system is tightly coupled in propulsion and steering. Hence higher demand on one will limit the availability of the other. The extreme condition is that - when the total thrust is at maximum, there will not be any differential thrust available to steer the AUV. It can be observed in Figure 6.11 that the actual speed of the AUV is slightly lower than the reference command. Intuitively, this can be explained through an example of following a straight path. The AUV needs to use full thrust to achieve the commanded speed. However, if the AUV deviates from the path, the convergence algorithm will command the AUV to steer in order to converge to the reference path. This action requires differential thrust for the steering motion. Therefore, the maximum available thrust becomes less and the AUV is no longer able to achieve the maximum speed for a straight segment.

In addition to the speed response, the thrusters' behaviour is also analysed. As illustrated in Figure 6.12, the total thrust is represented by the blue dashed line and the differential thrust is the red solid line. The thrusters' response is labelled in correspondence to each segment along the arbitrary path. Referring to Table 6.1, Segment 1, 3, 5, 7, 9, 11 and 13 are line segments. It can be seen from the Figure 6.12 that the total thrust is around 60 N (full thrust) and differential thrust is varying around zero when the AUV is following these straight-line segments. Chattering can be observed in the total thrust and differential thrust signals. This is because of the actions taken when the AUV experiences deviation. The results also reflect the fact that larger differential thrust is required for smaller turning radius (tighter turns). For example, the average differential thrust for Segment 8 (an arc segment of R = 50 m) is smaller than the average differential thrust for Segment 12 (an arc segment of R = 10 m).

Moreover, an obvious reduction in the total thrust is found at the beginning of the transitions from a line segment to an arc segment (from Segment 1 to 2, 3 to 4, 5 to 6, 7 to 8, 9 to 10, 11 to 12, 13 to 14). This is expected as the AUV is supposed to decelerate during the transitions from line to arc based on the speed response in Figure 6.11. Moreover, as the step change in the speed reference cannot be met, the AUV deviates, and hence it is required that the vehicle slows down in order to get back on track.

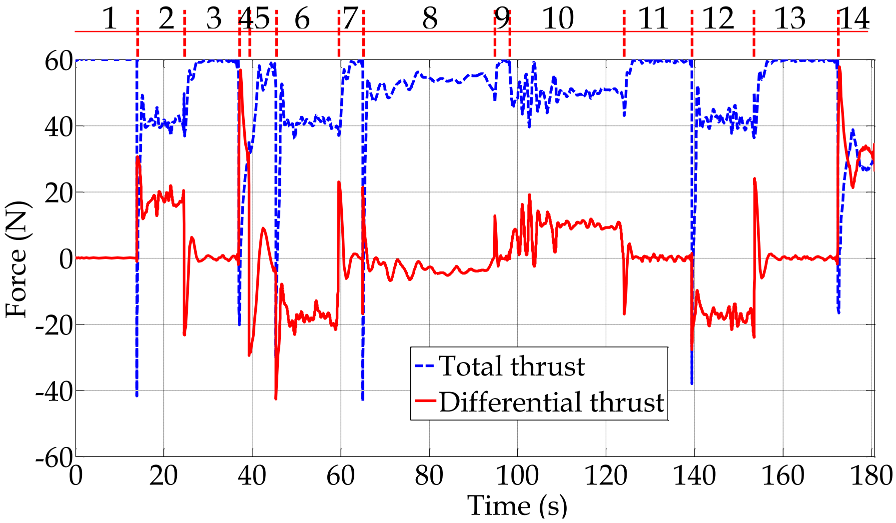

Figure 6.12: Total thrust and differential thrust during path following. The total thrust is represented by the blue dashed line and the red solid line represents the differential thrust.

Figure 6.13 illustrates the thrust evolution of the two thrusters. While the blue dashed line represents T_2, the red solid line represents T_1. At least one of the thrusters is operating around full thrust (30 N) during the path following. This is consistent with the findings from the Monte Carlo analysis – the differential thrust system reaches saturation when one of the thrusters is on full thrust in order to traverse as fast as possible. As labelled on the plot, the two thrusters are operated in the opposite direction when following a tight curve with small radius of curvature (i.e., Segment 4 of $R = 5$ m) and both are set on full thrust forward (30 N) when moving along line segments.

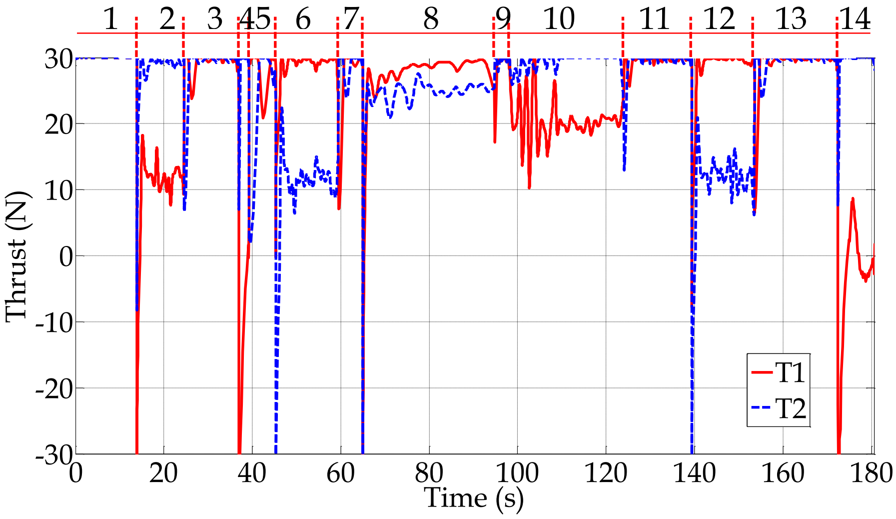

Figure 6.13: Thrusts of two thrusters during path following. The red solid line represents T_1 , and T_2 is the blue dashed line.

The results have shown that the prototype AUV managed to follow an arbitrary path according to the motion reference generated by the proposed guidance algorithm despite the small tracking error in speed. In addition, the time efficiency is analysed by comparing to the constant speed guidance method.

Table 6.4: Time taken for traversing a distance of 452.4 m using the proposed guidance and constant speed guidance along the arbitrary path (in Figure 6.6), and time for following a straight line path of the same length.

		Time taken for traversing 452.4 m
Guidance methods	The proposed guidance	180.5 s
	Constant speed guidance	224.3 s
Time taken for following a straight line of 452.4 m		151.4 s

As shown in Table 6.4, the given arbitrary path is 452.4 m in total, and it takes the AUV 180.5 seconds to follow this using the proposed guidance algorithm. This would otherwise take at least 224.3 seconds when the

AUV is guided with a constant path following speed, which is equivalent to around 19.5% of time saving. The time to follow the arbitrary path (180.5 seconds and 224.3 seconds) is also compared to the case of an AUV following a straight line of the same length (151.4 seconds as given in Table 6.4). As expected, it takes the AUV longer to follow the arbitrary path than to follow a straight line, as the former contains many curved segments (Figure 6.6) and the AUV needs to reduce its speed on these segments. In the subsequent section, the time efficiency of the proposed guidance for path following will be further investigated through consideration of a lawn mower path.

6.2 Path following of a lawn mower path

The lawn-mower pattern is one of the most popular pathways for mapping, searching and monitoring applications within a given region. The lawn mower path is simple, yet guarantees full coverage of the scanning area, which is crucial to the aforementioned missions (Haugen, 2010). Therefore, a lawn mower path is selected to evaluate the time efficiency of path following performance using the proposed algorithm. As shown in Figure 6.14, a typical lawn mower path consists of a series of lines and arcs (semicircles). The distance between two parallel lines is determined by the mission requirements. As the line and arc segments are tangentially connected, the radius of the arc segment is half of the distance between lines. For the example lawn mower path given in Figure 6.14, the parallel line segments are 10 m apart from each other, and hence the turning radius of the arc segments, R, is 5 m. The turning radius chosen for the example path is to demonstrate the time efficiency of the proposed guidance method. The length of the path is set to be 50 m, which is long enough for the AUV to reach its maximum speed on the straight segments, however, it should not be too long, otherwise it will be more difficult to observe the consequence of the speed reduction for the curve segments on the overall time efficiency. In the following section, simulation results of following the reference lawn mower path will be presented.

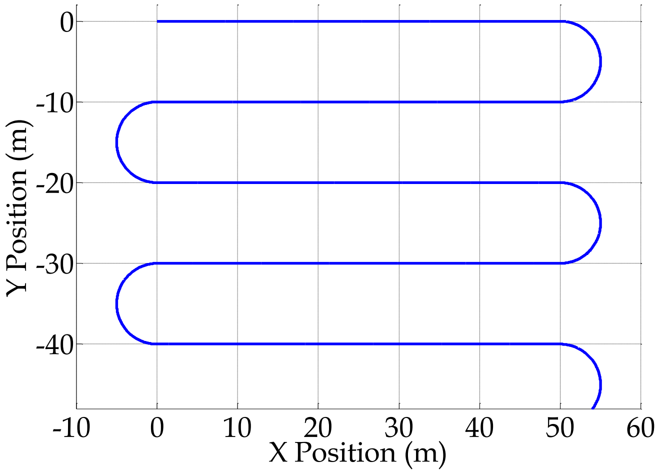

Figure 6.14: Diagram of a typical lawn mower path. The path consists of line segments and arc segments. These segments are tangentially connected. $R = 5$ m for the arc segments in the reference path.

6.2.1 Error analysis

Error analysis is performed based on the simulation results for the path following in this section. Firstly, the actual path (in red) is compared to the reference path (the blue line) in Figure 6.15. The comparison shows a good match between the two, indicating the reference lawn mower path has been followed. Deviations are observed around the transition regions - entering and exiting the arc segments. As discussed in the random path case in Section 6.1, this is due to the step changes in the motion commands from the guidance system. Details will be analysed by the motion response of the AUV later.

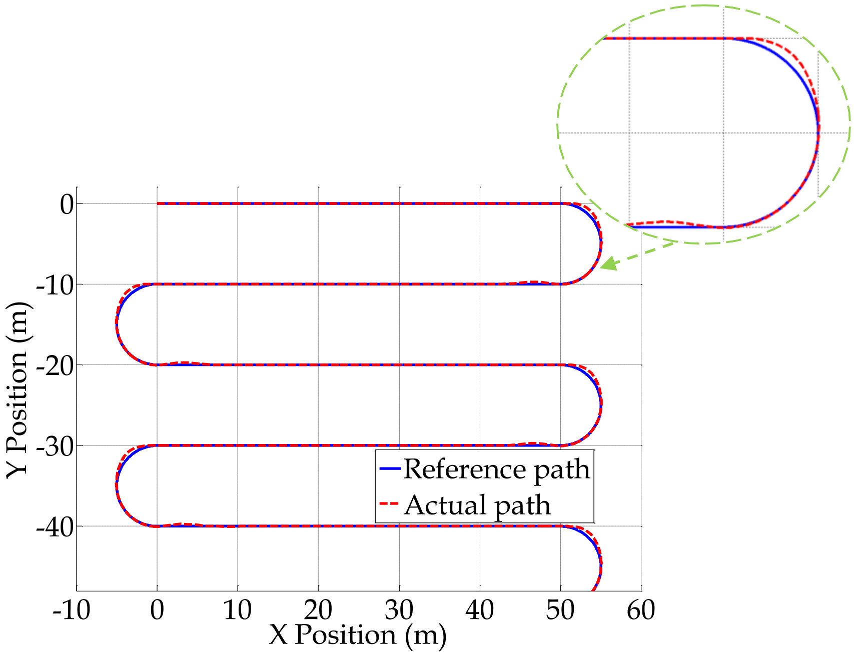

Figure 6.15: Comparison between the actual path and the reference path in the simulation. The reference path is represented by the blue solid line while the actual path is the red dashed line.

The deviations during path following of the lawn mower path also suggest that good path following accuracy has been achieved. From the histogram in Figure 6.16, it can be seen that most deviations of the AUV are very close to zero – within 0.02 m.

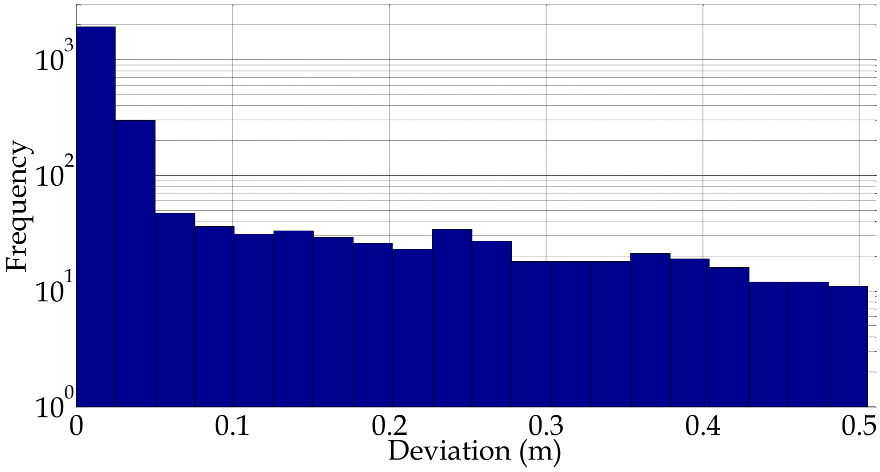

Figure 6.16: Histogram of the deviation during path following of the lawn mower path with $R = 5$ m. All deviations (in total 2630 data points) are under 0.5 m, while most (approximately 75.5%) are concentrated around 0.02 m.

In regard to the real-time deviation as illustrated in Figure 6.17, relatively large deviations are found around the transition regions; fundamentally, the deviation is due to the step changes of the command signal caused by the curvature discontinuities in the lawn mower path.

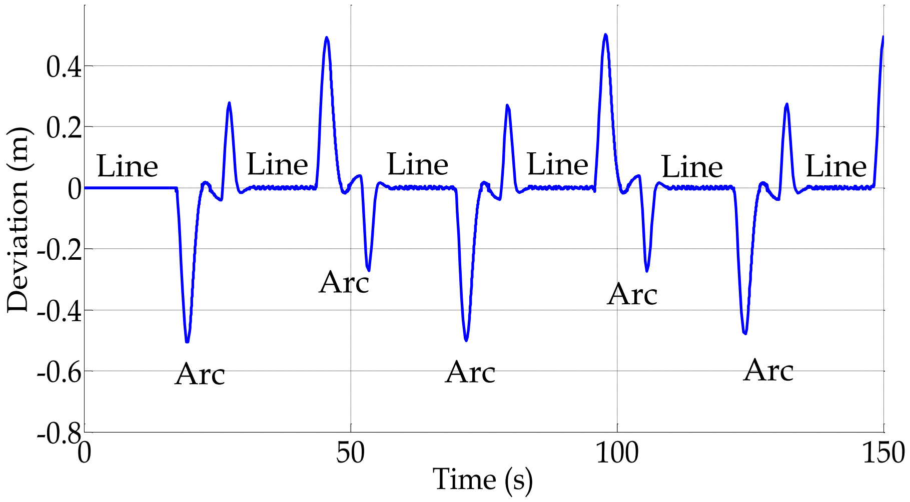

Figure 6.17: Real time deviation of the AUV during path following on the lawn mower path with $R = 5$ m.

Furthermore, it can be seen that the deviation when the AUV enters an arc segment is slightly larger than when it exits an arc segment. This is expected since the deceleration from a higher speed will lead to higher deviation than the acceleration from a lower speed due to the inertia. Nevertheless, the maximum deviation during the path following is below 0.5 m using the proposed algorithm.

6.2.2 Time efficiency analysis

In order to evaluate the time efficiency of the proposed guidance algorithm, path following using a conventional constant speed guidance method (Haugen, 2010) is simulated for comparison with the proposed method. For the constant speed method, as discussed in the literature review in Chapter 2, the selected reference speed needs to satisfy the smallest radius of curvature along given paths. The same lawn mower path with $R = 5$ m is used for the simulation, and the reference speed is decided accordingly. As shown in Figure 6.18, the speed response of the AUV using the two guidance methods are plotted.

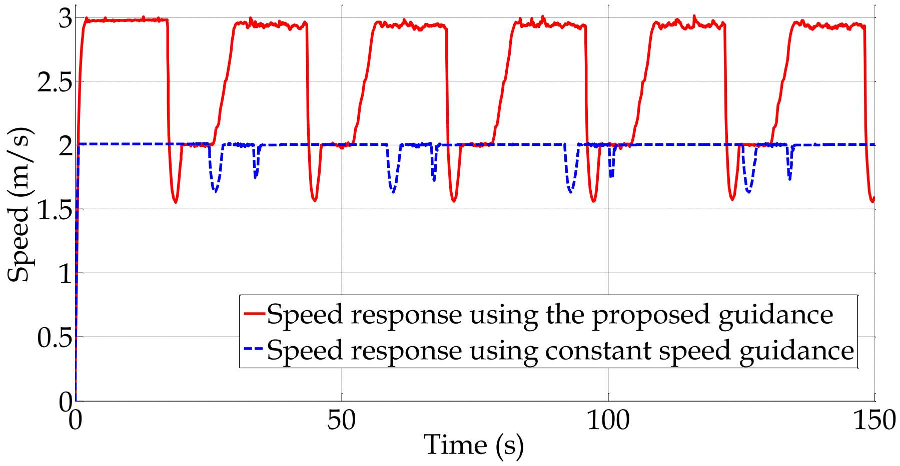

Figure 6.18: Simulated speed response of the AUV path following using two guidance methods. The constant speed guidance (in blue) and the proposed guidance method (in red) are compared.

In Figure 6.18, the red solid line represents the speed profile under the proposed guidance method with varying speed, while the blue dashed line represents the constant speed method as its counterpart. Both speed profiles are plotted with respect to time, therefore the traversing distance along the path can be determined by the area covered by these two curves. As should be apparent, within the same amount of time, the area covered by the red line is larger than that covered by the blue line. The traversing distances covered following the same lawn mower path by using the two guidance methods are summarized in Table 6.5.

Table 6.5: Traversing distance of the AUV in 150 seconds using the proposed guidance and constant speed guidance for path in Figure 6.14. Within same amount of time, the traversing distance for a straight line path is calculated for comparison.

		Traversing distance in 150 seconds
Guidance methods	The proposed guidance	384.6 m
	Constant speed guidance	296.9 m
Traversing distance on straight line in 150 seconds		448.3 m

According to the results, there is an approximate 30% increase in the traversing distance within 150 seconds by using the proposed method. The comparison shows that the proposed guidance algorithm enables the AUV to traverse further along the same lawn mower path within the same amount of time when compared with a conventional constant speed guidance method, meaning better time efficiency of path following. In Table 6.5, the distance when the AUV follows a straight path within the same amount of time is compared with the distance of following the lawn mower path. As expected, the results show that the AUV moves further along the straight path ($448.3\ \mathrm{m}$) than along the lawn mower path, (respectively 384.6 m and 296.9 m) within the same amount of time.

Additionally, Table 6.6 compares the two methods from a time saving point of view. As shown, the time required to follow the lawn mower path with a total length of 247.1 m is summarized, and the time of following a straight line with the same length is used as it gives the shortest time the AUV can achieve. Compared to 82.9 s for following the straight line, it takes the AUV 95.7 s, which is 15% increase in the total traversing time, to follow the lawn mower path (shown in Figure 6.14) using the proposed guidance method. This is expected as the AUV needs to slow down on arc segments when following the lawn mower path, which takes more time than following a straight path with the same length.

Table 6.6: Time taken for traversing a lawn mower path (in Figure 6.14) of 247.1 m using the proposed guidance and constant speed guidance. Time for following a straight line path.

		Time taken for traversing $\mathbf{247.1\ m}$
Guidance methods	The proposed guidance	95.7 s
	Constant speed guidance	125.3 s
Time taken for following a straight line of $\mathbf{247.1\ m}$		82.9 s

Moreover, when following the lawn mower path, it can be seen that it takes 125.3 seconds using the constant path following guidance method, whereas it only takes 95.7 s using the proposed method. This is a 23.6% time saving, which shows the time efficiency of the proposed guidance algorithm.

6.3 Summary

This chapter investigates the effectiveness of the proposed guidance algorithm. The path following of the prototype AUV on an arbitrary path was simulated. From the error analysis, it was found that the AUV was able to follow an arbitrary reference path using the proposed guidance law. Chattering was observed in the results, which is caused by the steering action commanded by the convergence law to eliminate the deviation. Nevertheless, the deviations during transitions were effectively attenuated by the convergence law.

The time efficiency of the proposed path following algorithm was also analysed. A comparison was made between the performance of the proposed method and a standard constant speed path following algorithm (Haugen, 2010). The results have clearly demonstrated that the proposed guidance method outperforms the constant speed guidance in respect of the time efficiency.

Based on the simulation results, the proposed guidance system is shown to be an effective solution for time efficient path following of the under-actuated differential thrust AUV for arbitrary paths. Potential future research directions extended from this work are identified in the subsequent chapter.

Chapter 7

Conclusions and future work

As introduced in Chapter 1, AUVs have been shown to have a significant role in many underwater applications, and have motivated extensive research. This research focuses on the time efficient path following of under-actuated differential thrust AUVs. The work presented in this thesis will be summarized, and future work will be discussed in this chapter.

7.1 Conclusions

Compared to the conventional fin-manoeuvred AUV, the prototype AUV in this research is manoeuvred by differential thrust. Guidance for such AUVs to follow arbitrary paths in a time efficient manner has not previously been addressed. This has been shown in the literature review in Chapter 2.

The development of a guidance and control system for path following is heavily reliant on simulations, and a model based on the prototype AUV with its configuration modified for planar motion was developed and verified in Chapter 3. The model was then used for a numerical analysis of the AUV motion limits in Chapter 4 and was also used for the development and verification of the proposed guidance algorithm in Chapters 5 and 6.

To traverse as fast as possible on the given path, the AUV is desired to be operated at its speed limits. The numerical solution presented in Chapter 4 was based on the Monte Carlo analysis using the AUV model. The results were constructed into a lookup table (as shown in Figure 4.7), where the maximum admissible speed and the sideslip angle can be determined for any given desired radius of curvature.

Based on the Monte Carlo analysis results, a curvature based guidance law was developed in Chapter 5. The guidance system consists of a traversing law and a convergence law. In the traversing law, the speed and heading commands are generated according to the path curvature using the database in Figure 4.7. Any reference path can be treated as a succession of segments with constant curvature, including curvature discontinuous paths. However, deviations occur when there are step changes in the motion references due to curvature discontinuities. Therefore, the convergence law was developed to eliminate the deviation by steering the AUV towards the path. To execute the reference speed and heading, two controllers were designed.

To evaluate the proposed guidance algorithm, the path following of an arbitrary path was simulated in Chapter 6. The results demonstrated good path following performance. Deviations are inevitable due to the curvature discontinuities and slight chattering was observed, but deviations were compensated effectively using the convergence law. In order to demonstrate the time efficiency, path following of a lawn mower path was simulated, using both the proposed guidance method and the conventional constant speed guidance method. It was illustrated that the former outperforms the latter with regard to the time efficiency of path following. Therefore, the proposed curvature-based guidance algorithm has been shown to be an effective solution for under-actuated differential thrust AUVs to follow arbitrary paths in a time efficient manner.

In addition, the simulation results provided insights into the potential future work to improve the path following performance further, as will be outlined in the subsequent section.

7.2 Future work

Future work extending from this research includes the following aspects. Firstly, it has been demonstrated from the simulation results in Chapter 6 that the time efficiency of path following can be further improved by reducing the deviation. Due to the feature of differential thrust systems, whenever deviation occurs, extra differential thrust is needed for corrective steering and hence less thrust can be used for traversing. The deviation is mainly caused by the curvature discontinuities, in which case the traversing law would generate motion references with step changes. The transitions between the segments can be formed into an optimization problem in order to minimize the path following time.

Secondly, the convergence algorithm can be improved to reduce the chattering. The current convergence law is based on a simple rule that the heading is adjusted proportionally with respect to the deviation (as discussed in Section 5.2.1). It can be integrated into a more sophisticated design in the future, where the corrective steering is adjusted according to the path ahead of the AUV to optimize the convergence.

In addition, the system robustness to external disturbances from the surrounding fluid could be analysed. There are many robust control laws available to be integrated with, and supported by, the guidance algorithm (Aguiar and Pascoal, 2008; Liu *et al.*, 2009)

Lastly, experimental implementation of the proposed method can be carried out in the future. The Monte Carlo analysis has found that the motion limit of the AUV can be achieved by using full thrust for one of the thrusters. Based on this finding, water tests can be performed to determine the motion limit of the AUV by setting one thruster on full and varying the thrust of the other thruster - each test uses a different thrust. Moreover, the path following performance using the proposed guidance algorithm can be evaluated by performing field tests. In order to achieve this, the motion controllers' gains need to be tuned experimentally. Similar to the simulations conducted in Chapter 6, different paths can be constructed for the AUV to follow. Deviations and motion responses of the AUV during the experiments can be used to validate the path following performance using the proposed method.

References

Aguiar, AP & Pascoal, AM (2002), 'Dynamic positioning and way-point tracking of underactuated AUVs in the presence of ocean currents'. In: *Proceedings of the 41st IEEE Conference on Decision and Control*, vol. 2, pp. 2105-2110.

Aguiar, AP & Hespanha, JP (2003), 'Position tracking of underactuated vehicles'. In: *IEEE Proceedings of the American Control Conference,* vol. 3, pp. 1988-1993.

Aguiar, AP, Hespanha, JP & Kokotovic, PV (2005), 'Path-following for nonminimum phase systems removes performance limitations'. In: *IEEE Transactions on Automatic Control*, vol. 50, no. 2, pp. 234-239.

Allen, H. and Perkins, E. (1951), *Characteristics of flow over inclined bodies of revolution*. Washington: National Advisory Committee for Aeronautics.

Antonelli, G & Robots, U (2002), 'Motion and Force Control of Vehicle-Manipulator Systems'. In: *Springer Transactions on Advanced Robotics, Napoli*.

Antonelli, G (2007), 'On the use of adaptive/integral actions for six-degrees-of-freedom control of autonomous underwater vehicles'. In: *IEEE Journal of Oceanic Engineering*, vol. 32, no. 2, pp. 300-312.

Antonelli, G, Fossen, T, & Yoerger, D (2008), ‘Underwater Robotics’. In: *Springer Handbook of Robotics*, Springer Berlin Heidelberg, pp. 987-1008.

Behal, A, Dawson, DM, Dixon, WE & Fang, Y (2002), 'Tracking and regulation control of an underactuated surface vessel with non-integrable dynamics'. In: *IEEE Transactions on Automatic Control,* vol. 47, no. 3, pp. 495-500.

Barsky, B & DeRose, TD (1990), 'Geometric continuity of parametric curves: Constructions of geometrically continuous splines'. In: *IEEE Computer Graphics and Applications,* vol. 10, no. 1, pp. 60-68.

Bibuli, M, Bruzzone, G, Caccia, M & Lapierre, L (2009), 'Path-following algorithms and experiments for an unmanned surface vehicle', In: *Journal of Field Robotics*, vol. 26, no. 8, pp. 669-688.

Blidberg, DR, Turner, RM & Chappell, SG (1991), 'Autonomous underwater vehicles: Current activities and research opportunities'. In: *Robotics and Autonomous Systems*, vol. 7, no. 2, pp. 139-150.

Blidberg, DR (2001), 'The development of autonomous underwater vehicles (AUV); a brief summary'. In: *IEEE International Conference of Robotics and Automation, Seoul, South Korea,* vol. 4.

Bloch, AM, Reyhanoglu, M & McClamroch, NH (1992), 'Control and stabilization of nonholonomic dynamic systems'. In: *IEEE Transactions on Automatic Control,* vol. 37, no. 11, pp. 1746-1757.

Bloch, AM (2003), *Nonholonomic mechanics and control*, vol. 24, Springer Science & Business Media.

Bobrow, JE, Dubowsky, S & Gibson, J (1985), 'Time-optimal control of robotic manipulators along specified paths'. In: *The International Journal of Robotics Research*, vol. 4, no. 3, pp. 3-17.

Breivik, M. (2010), *Topics in guided motion control of marine vehicles*. Ph.D. Norwegian University of Science and Technology.

Brockett, RW (1983), *Asymptotic stability and feedback stabilization*. Virginia: Defense Technical Information Center, 1983.

Caccia, M, Bibuli, M, Bono, R & Bruzzone, G (2008), 'Basic navigation, guidance and control of an unmanned surface vehicle'. In: *Autonomous Robots*, vol. 25, no. 4, pp. 349-365.

Casanova, D, Sharp, R & Symonds, P (2000), 'Minimum time manoeuvring: The significance of yaw inertia'. In: *Vehicle System Dynamics*, vol. 34, no. 2, pp. 77-115.

Cavallo, E, Michelini, RC & Filaretov, VF (2004), 'Conceptual design of an AUV equipped with a three degrees of freedom vectored thruster'. In: *Journal of Intelligent and Robotic Systems*, vol. 39, no. 4, pp. 365-391.

Çengel, Y., Cimbala, J. and Turner, R. (2011). *Fundamentals of thermal-fluid sciences*. New York: McGraw-Hill Higher Education.

Chin, C. S. (2012), *Computer-Aided Control Systems Design: Practical Applications using MATLAB and Simulink*, CRC Press, pp.182-186.

Christ, R. and Wernli, R. (2013), *ROV Manual: A User Guide for Remotely Operated Vehicles*, Butterworth-Heinemann.

Chyba, M, Haberkorn, T, Smith, RN & Choi, S (2008), 'Design and implementation of time efficient trajectories for autonomous underwater vehicles'. In: *Ocean Engineering*, vol. 35, no. 1, pp. 63-76.

Chyba, M, Haberkorn, T, Smith, RN & Choi, SK (2015), 'Autonomous Underwater Vehicles: Development and Implementation of Time and Energy Efficient Trajectories'. In: *Ship Technology Research*, 55(1), pp.36-48.

Craven, PJ, Sutton, R & Burns, RS (1998), 'Control strategies for unmanned underwater vehicles'. In: *Journal of Navigation*, vol. 51, no. 1, pp. 79-105.

Do, KD, Jiang, Z-P & Pan, J (2004), 'Robust adaptive path following of underactuated ships'. In: *Automatica*, vol. 40, no. 6, pp. 929-944.

Do, KD & Pan, J (2004), 'State-and output-feedback robust path-following controllers for underactuated ships using Serret–Frenet frame'. In: *Ocean Engineering*, vol. 31, no. 5, pp. 587-613.

Do, KD & Pan, J (2009), *Control of ships and underwater vehicles: design for underactuated and nonlinear marine systems*, Springer Science & Business Media.

Dolinskaya, IS & Maggiar, A (2012), 'Time-optimal trajectories with bounded curvature in anisotropic media'. In: *The International Journal of Robotics Research*, vol. 31, no. 14, pp. 1761-1793.

Encarnaçao, P & Pascoal, A (2000), '3D path following for autonomous underwater vehicle'. In: *Proceedings of 39th IEEE Conference on Decision and Control*.

Encarnaçao, P & Pascoal, A (2001), 'Combined trajectory tracking and path following: an application to the coordinated control of autonomous marine craft'. In: *Proceedings of the 40th IEEE Conference on Decision and Control, 2001*, pp. 964-969.

Evans, J (2003), *Dynamics Modelling and Performance Evaluation of an Autonomous Underwater Vehicle*. Masters of Philosophy in Engineering. McGill University.

Evans, J & Nahon, M (2004), 'Dynamics modelling and performance evaluation of an autonomous underwater vehicle'. In: *Ocean Engineering*, vol. 31, no. 14, pp. 1835-1858.

El-Hawary, F (2001). *The ocean engineering handbook*. Boca Raton, Fla.: CRC Press.

Fossen, TI (1994), *Guidance and control of ocean vehicles*, John Wiley & Sons Inc.

Fossen, TI (2002), 'Marine Control Systems: Guidance', *Navigation, and Control of Ships, Rigs and Underwater Vehicles,* Marine Cybernetics, Trondheim, Norway.

Geisbert, JS (2007), *Hydrodynamic modelling for autonomous underwater vehicles using computational and semi-empirical methods*. Ph.D. Virginia Polytechnic Institute and State University.

Haugen, J (2010), *Guidance algorithms for planar path-based motion control scenarios*. Masters of Science in Engineering Cybernetics. Norwegian University of Science and Technology.

Healey, AJ & Lienard, D (1993), 'Multivariable sliding mode control for autonomous diving and steering of unmanned underwater vehicles'. In: *IEEE Journal of Oceanic Engineering,* vol. 18, no. 3, pp. 327-339.

Hespanha, JP (2007), 'Trajectory-tracking and path-following of underactuated autonomous vehicles with parametric modelling uncertainty'. In: *IEEE Transactions on Automatic Control,* vol. 52, no. 8, pp. 1362-1379.

Hoerner, SF & Borst, HV (1985), 'Fluid-dynamic lift: practical information on aerodynamic and hydrodynamic lift'. In: *NASA STI/Recon Technical Report A*, *76*, pp. 32167.

Hopkin, D & Den Hertog, V (1993), 'The hydrodynamic testing and simulation of an autonomous underwater vehicle'. In: *Proceedings of the Second Canadian Marine Dynamics Conference,* pp. 274-281.

Hovel, FS, Grosenbaugh, MA & Triantafyllou, MS (1990), 'Modelling the dynamics of a deeply-towed underwater vehicle system'. In: *The First ISOPE European Offshore Mechanics Symposium,* International Society of Offshore and Polar Engineers.

Jiang, ZP & Nijmeijer, H (1997), 'Tracking control of mobile robots: a case study in backstepping'. In: *Automatica*, vol. 33, no. 7, pp. 1393-1399.

Jiang, ZP (2002), 'Global tracking control of underactuated ships by Lyapunov's direct method'. In: *Automatica*, vol. 38, no. 2, pp. 301-309.

Jorgensen, LH (1973), *Prediction of Static Aerodynamic Characteristics for Space-shuttle-like and Other Bodies at Angles of Attack from 0° to 180°*. In: *NASA Technical Report TN D-6996*.

Kaminer, I, Pascoal, A, Hallberg, E & Silvestre, C (1998), 'Trajectory tracking for autonomous vehicles: An integrated approach to guidance and control'. In: *Journal of Guidance, Control, and Dynamics*, vol. 21, no. 1, pp. 29-38.

Khalil, HK (2002), *Nonlinear systems*. Upper Saddle River, N.J.: Prentice Hall.

Kim, YS, Lee, J, Park, SK, Jeon, BH & Lee, PM (2009), 'Path tracking control for underactuated AUVs based on resolved motion acceleration control'. In: *IEEE 4th International Conference on Autonomous Robots and Agents, ICARA 2009*, pp. 342-346.

Kinsey, JC, Eustice, RM & Whitcomb, LL (2006), 'A survey of underwater vehicle navigation: Recent advances and new challenges'. In: *IFAC Conference of Manoeuvring and Control of Marine Craft,* vol. 88.

Kokegei, M, He, F & Sammut, K (2008), 'Fully coupled 6 degrees-of-freedom control of Autonomous Underwater Vehicles'. In: *IEEE OCEANS 2008,* pp. 1-7.

Lam, D (2012), *A model predictive approach to optimal path-following and contouring control*. Ph.D. The University of Melbourne.

Lamb, H (1932), *Hydrodynamics*, Cambridge University Press.

Lapierre, L & Jouvencel, B (2008), 'Robust nonlinear path-following control of an AUV'. In: *IEEE Journal of Oceanic Engineering,* vol. 33, no. 2, pp. 89-102.

Lea, R, Allen, R & Merry, S (1999), 'A comparative study of control techniques for an underwater flight vehicle'. In: *International Journal of Systems Science*, vol. 30, no. 9, pp. 947-964.

Lefeber, E, Pettersen, KY & Nijmeijer, H (2003), 'Tracking control of an underactuated ship'. In: *IEEE Transactions on Control Systems Technology*, vol. 11, no. 1, pp. 52-61.

Leonard, JJ, Bennett, AA, Smith, CM & Feder, HJS (1998), 'Autonomous underwater vehicle navigation'. In: *IEEE ICRA Workshop on Navigation of Outdoor Autonomous Vehicles, Leuven, Belgium, May*.

Liu, S, Wang, D & Poh, E (2009), 'Output feedback control design for station keeping of AUVs under shallow water wave disturbances'. In: *International Journal of Robust and Nonlinear Control*, vol. 19, no. 13, pp. 1447-1470.

Maeda, H, El-Hawary, F & Rahman, M, (2001), ‘Marine hydrodynamics and dynamics of a floating structure’. In: *The Ocean Engineering Handbook*, CRC Press LLC.

Maxon motor (2016). *maxon DC motor products*. [online] Available at: http://www.maxonmotor.com.au/maxon/view/content/products [Accessed 1 Mar. 2014].

Mazenc, F, Pettersen, K & Nijmeijer, H (2002), 'Global uniform asymptotic stabilization of an underactuated surface vessel'. In: *IEEE Transactions on Automatic Control*, vol. 47, no. 10, pp. 1759-1762.

Mostafa HS, John HLV, & Syed MZ (2010), ‘Thermophysical properties of seawater: A review of existing correlations and data’. In: *Desalination and Water Treatment,* vol. 16, pp. 354-380.

Munk, MM (1924), 'The aerodynamic forces on airship hulls'. In: *NASA Annual Report*, pp. 451-468.

Naeem, W (2004), *Guidance and control of an autonomous underwater vehicle*. Ph.D. University of Plymouth.

Nahon, M (1996), 'A simplified dynamics model for autonomous underwater vehicles'. In: *IEEE Proceedings of the 1996 Symposium on Autonomous Underwater Vehicle Technology*, pp. 373-379.

Newman, JN (1977), *Marine hydrodynamics*, MIT press.

Nijmeijer, H & Van der Schaft, A (2013), *Nonlinear dynamical control systems*, Springer Science & Business Media.

Oceaneering, (2013). Subsea Oilfield | Oceaneering. [online] Available at: http://www.oceaneering.com/products-and-services/subsea-oilfield/ [Accessed 3 Mar. 2013].

Ostafichuk, PM (2004), *AUV Hydrodynamics and modelling for improved control*. Ph.D. The University of British Columbia.

Paull, L, Saeedi, S, Seto, M and Li, H (2014), 'AUV navigation and localization: A review'. In: *IEEE Journal of Oceanic Engineering*, vol. 39, pp. 131-149.

Park, S, Deyst, J & How, JP (2004), 'A new nonlinear guidance logic for trajectory tracking'. In: *Navigation and Control Conference Proceedings of the AIAA Guidance*, pp. 1-16.

Perrault, DE (2002), *Autonomous underwater vehicles (AUV) sensitivity of motion response to geometric and hydrodynamic parameters and AUV behaviours with control plane faults,* Ph.D. Memorial University of Newfoundland.

Prestero, TTJ (2001), *Verification of a six-degree of freedom simulation model for the REMUS autonomous underwater vehicle,* Masters of Science in Mechanical Engineering and Ocean Engineering. Massachusetts Institute of Technology.

Refsnes, JE, Sorensen, AJ & Pettersen, KY (2008), 'Model-based output feedback control of slender-body underactuated AUVs: theory and experiments'. In: *IEEE Transactions on Control Systems Technology,* vol. 16, no. 5, pp. 930-946.

Repoulias, F & Papadopoulos, E (2005), 'Trajectory planning and tracking control of underactuated AUVs'. In: *Proceedings of the 2005 IEEE International Conference on Robotics and Automation, ICRA 2005*, pp. 1610-1615.

Repoulias, F & Papadopoulos, E (2007), 'Planar trajectory planning and tracking control design for underactuated AUVs'. In: *Ocean Engineering*, vol. 34, no. 11, pp. 1650-1667.

Rubinstein, R. (2008). *Simulation and the Monte Carlo Method, 2nd Edition Set*. John Wiley & Sons.

Sahafi, L (2013), *Cost effective navigation of autonomous underwater vehicles*, Masters of Philosophy in Mechanical Engineering. The University of Adelaide.

Samson, C (1995), 'Control of chained systems application to path following and time-varying point-stabilization of mobile robots'. In: *IEEE Transactions on Automatic Control,* vol. 40, no. 1, pp. 64-77.

Sanz, PJ, Prats, M, Ridao, P, Ribas, D, Oliver, G & Ortiz, A (2010), 'Recent progress in the RAUVI project: A reconfigurable autonomous underwater vehicle for intervention'. In: *IEEE Proceedings of ELMAR 2010*, pp. 471-474.

SeaBotix Inc., (2016). Seabotix.com. [online] Available at: http://www.seabotix.com/products/auv_thrusters.htm [Accessed 11 Mar. 2015].

Serrani, A & Conte, G (1999), 'Robust nonlinear motion control for AUVs'. In: *IEEE Robotics & Automation Magazine,* vol. 6, no. 2, pp. 33-38.

Shi, Y, Qian, W, Yan, W & Li, J (2006), 'Adaptive depth control for autonomous underwater vehicles based on feedforward neural networks'. In: *Intelligent Control and Automation*, Springer, pp. 207-218.

Shin, KG & McKay, ND (1985), 'Minimum-time control of robotic manipulators with geometric path constraints'. In: *IEEE Transactions on Automatic Control,* vol. 30, no. 6, pp. 531-541.

Skjetne, R & Fossen, T (2001), 'Nonlinear manoeuvring and control of ships'. In: *MTS/IEEE Conference and Exhibition OCEANS,* vol. 3, pp. 1808-1815.

Skjetne, R, Fossen, TI & Kokotović, PV (2004), 'Robust output manoeuvring for a class of nonlinear systems'. In: *Automatica*, vol. 40, no. 3, pp. 373-383.

Skjetne, R (2005), *The manoeuvring problem*, Ph.D. Department of Engineering Cybernetics, Norwegian University of Science and Technology, Trondheim, Norway.

Smallwood, D & Whitcomb, LL (2004), 'Model-based dynamic positioning of underwater robotic vehicles: theory and experiment'. In: *IEEE Journal of Oceanic Engineering,* vol. 29, no. 1, pp. 169-186.

Solberg, T (1992), *A numerical study of laminar and turbulent separated flows over a circular cylinder at a plane wall*, Ph.D. Division of Applied Mechanics, NTH, Norway, University of Trondheim.

Stengel, RF (2012), *Optimal control and estimation*, Courier Corporation.

Stutters, L, Liu, H, Tiltman, C & Brown, DJ (2008), 'Navigation technologies for autonomous underwater vehicles'. In: *IEEE Transactions on Systems, Man, and Cybernetics, Part C: Applications and Reviews,* vol. 38, no. 4, pp. 581-589.

Techet AH. (2005) *Hydrodynamics for Ocean Engineers course notes for MIT 13.012*. Massachusetts Institute of Technology.

Tedrake, R (2009), *Underactuated robotics: Learning, planning, and control for efficient and agile machines course notes for MIT 6.832*. Massachusetts Institute of Technology.

Triantafyllou, MS & Hover, FS, (2004), 'Manoeuvring and control of surface and underwater vehicles'. *Cambridge, Massachusetts, USA*.

Triantafyllou, MS & Grosenbaugh, M (1991), 'Robust control for underwater vehicle systems with time delays'. In: *IEEE Journal of Oceanic Engineering*, vol. 16, no. 1, pp. 146-151.

Velenis, E & Tsiotras, P (2005), 'Optimal velocity profile generation for given acceleration limits: Receding horizon implementation'. In: *IEEE Proceedings of American Control Conference*, pp. 2147-2152.

Velenis, E & Tsiotras, P (2005), 'Minimum time vs maximum exit velocity path optimization during cornering'. In: *2005 IEEE International Symposium on Industrial Electronics,* pp. 355-360.

Velenis, E, Katzourakis, D, Frazzoli, E, Tsiotras, P & Happee, R (2011), 'Steady-state drifting stabilization of RWD vehicles'. In: *Control Engineering Practice*, vol. 19, no. 11, pp. 1363-1376.

Wadoo, S & Kachroo, P (2010), *Autonomous underwater vehicles: modelling, control design and simulation*, CRC Press.

Wang, W & Clark, CM (2007), 'Modelling and simulation of the VideoRay Pro III underwater vehicle'. In: *IEEE OCEANS 2006-Asia Pacific,* pp. 1-7.

Wang, W (2007), *Autonomous control of a differential thrust micro ROV*. Masters of Applied Science in Mechanical Engineering. University of Waterloo.

Woods Hole Oceanographic Institution, (2014). *REMUS 100*. [online] Available at: http://www.whoi.edu/main/remus100 [Accessed Dec. 2014].

Woolsey, CA (2005), 'Review of marine control systems: Guidance, navigation, and control of ships, rigs and underwater vehicles'. In: *Journal of Guidance, Control, and Dynamics*, vol. 28, no. 3, pp. 574-575.

Yoerger, DR & Slotine, JJE (1985), 'Robust trajectory control of underwater vehicles'. In: *IEEE Journal of Oceanic Engineering,* vol. 10, no. 4, pp. 462-470.

Yuh, J (2000), 'Design and control of autonomous underwater robots: A survey'. In: *Autonomous Robots*, vol. 8, no. 1, pp. 7-24.

Appendix A

Wind tunnel test

A wind tunnel test was performed for a different project in the School of Mechanical Engineering at the University of Adelaide, in order to determine the hydrodynamic coefficients used in the AUV model (as presented in Chapter 3). The wind tunnel test is briefly introduced in this section. Details of the testing can be found in the project report (Pavloudis *et al.*, 2012). As illustrated in Figure A.1, a KC wind tunnel was used. This wind tunnel was operated at a range of airspeeds with the prototype AUV set inside, the flow speeds were measured using a pitot static probe.

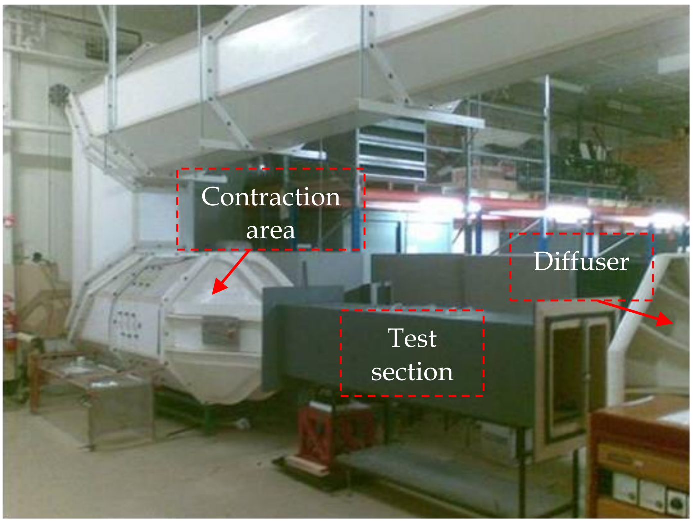

Figure A.1: KC wind tunnel (based on Pavloudis *et al.*, 2012)

In order to secure the vehicle in the wind tunnel during the tests, a testing rig was used as shown in Figure A.2. It can be seen that the rig consists of two components, a collar holding the hull and a strut attaching the vehicle to the load cell while maintaining the orientation of the vehicle. The drag and lift on the vehicle at different angles and speeds were determined.

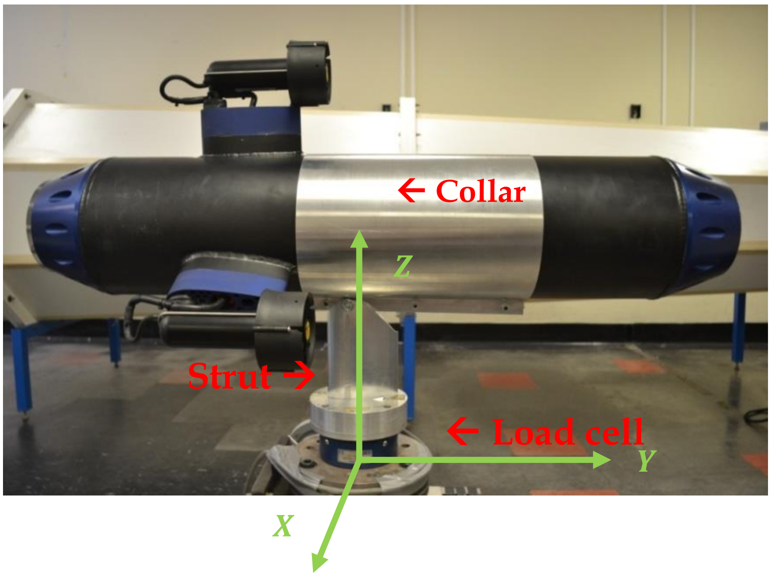

Figure A.2: The testing rig set up (based on Pavloudis *et al.,* 2012)

The equivalent operation water speeds for the chosen airspeeds in the wind tunnel test can be determined due to the non-dimensional similarity for the seawater and air. This can be achieved by applying the same Reynolds number as

$$Re_{Water} = Re_{Air}. \tag{A.1}$$

The equation for calculating the Reynolds number has been given in Equation (3.9). Therefore the equivalent water speed can be calculated as:

$$V_{Water} = \frac{\rho_{Air} V_{Air} \mu_{Water}}{\rho_{Water} \mu_{Air}}. \tag{A.2}$$

The fluid properties of the air and seawater are different, those used for the calculating the equivalent water speed is given in Table A.1.

Table A.1: Air and seawater properties (based on Pavloudis *et al.,* 2012)

Property	**Air**	**Seawater**
Temperature (°C)	24.5	18
Density (kg/m^3)	1.205	1035
Dynamic Viscosity (kg/ms)	1.983×10^{-5}	1.16×10^{-3}

During the wind tunnel test, the vehicle angle and flow speeds in the wind tunnel were adjusted over a range according to the KC wind tunnel capability (The KC wind tunnel is capable of producing up to approximately 32 m/s air speed), and a selection from the range was chosen for the verification, as tabulated in Table A.2. Also, the equivalent speeds in water were determined for the same Reynolds numbers, using the properties of water.

Table A.2: Air and water speed for the same Reynolds number

Reynolds Number (10^6)	**Air Speed (m/s)**	**Water speed (m/s)**
0.4861	10	0.6811
0.5834	12	0.8173
1.2639	26	1.7707
1.3126	27	1.8388

Appendix B

Simulink model

The Simulink model has been used for the numerical analysis of the motion limits and simulation of the AUV path following. In this section, subsystems of the Simulink model are illustrated in Figure B.1, Figure B.2, Figure B.3 and Figure B.4

Figure B.1 presents the guidance and control system. It can be seen that the waypoints along the path, the real-time position and orientation of the AUV are fed into the MC function. The nearest waypoint is found and the deviation of the AUV can be calculated, and then the reference speed and heading angle of the AUV are determined based on the nearest waypoint. A linear corrective steering angle with respect to the deviation will be compounded to the reference heading command. Two separate PID controllers compensate the speed and heading errors.

In Figure B.2, lift and drag are calculated for given speed and sideslip angle. All forces are transformed to G-frame based on the kinematics model as shown in Figure B.3. The resultant forces in G-frame (as shown in Figure 3.1: The G-frame $\{G\}$, the B-frame $\{B\}$) are fed into the AUV state space model, where the vehicle responses (states) are used as feedback of the control loop.

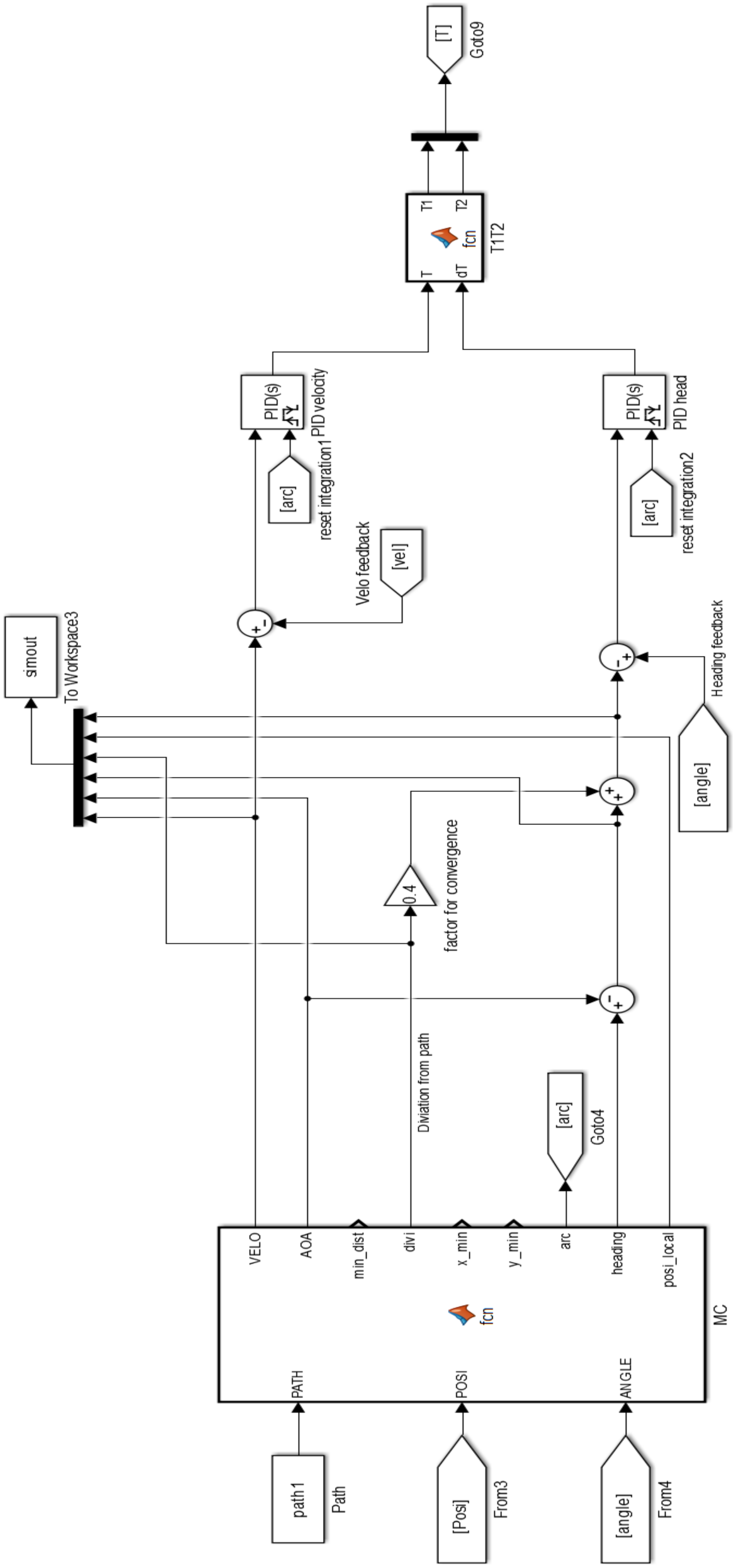

Figure B.1: Guidance and control system

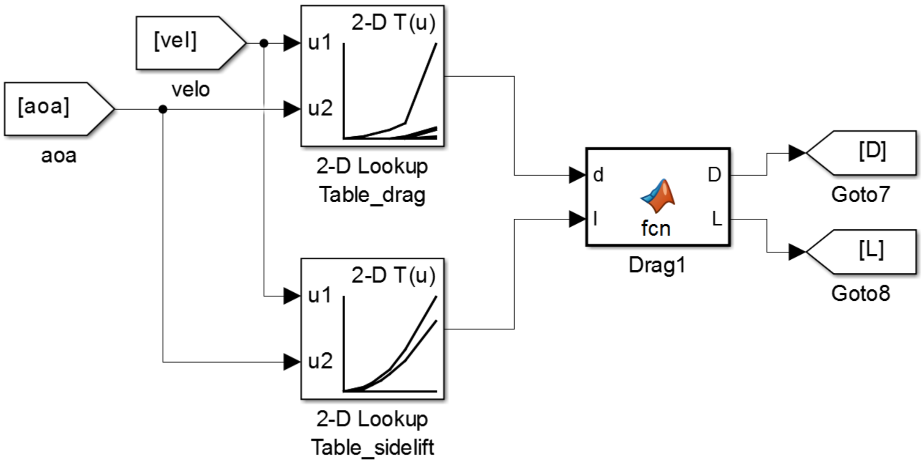

Figure B.2: Lift and drag calculation

The AUV kinematics and state space model are illustrated in Figure B.3. It can be seen that all forces are converted into the global frame, along with moments, and are fed into the state space model of the AUV body. Moreover, the real time sideslip angle and speed of the AUV are calculated using the AUV responses from the state space model. The angle and speed are then fed into the subsystem in Figure B.2 to calculate the lift and drag forces.

The steady state criterion for the Monte Carlo analysis is illustrated Figure B.4. As mentioned in Chapter 4, this criterion is used to establish when the system reaches its steady state under the given thrusts. The real time turning radius is compared with the value of 3 seconds later. The system is assumed to achieve the steady state if the difference between the two is less than 0.01 m.

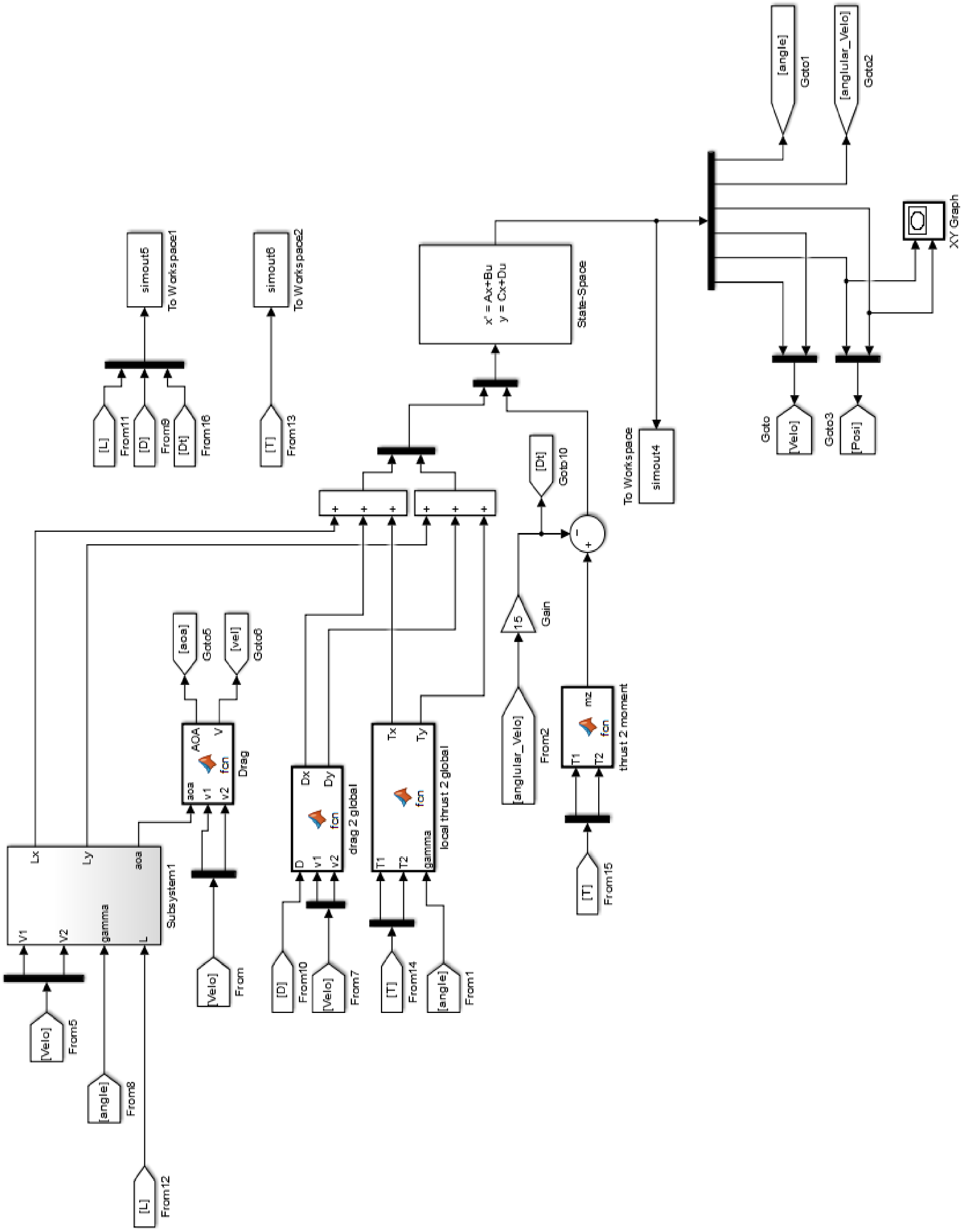

Figure B.3: AUV kinematics and the state space model

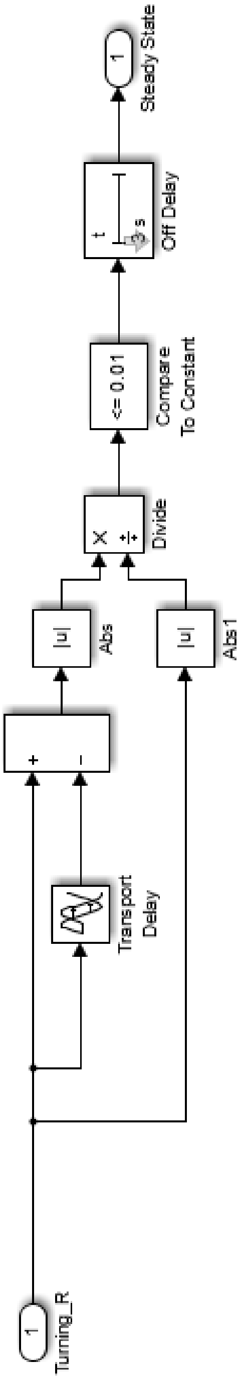

Figure B.4: Steady state criterion in Monte Carlo Analysis.

Appendix C

Thruster specifications

The thrusters used on the prototype AUV are SeaBotix BTD150, and the specifications are given in Table C.1.

Table C.1: Thruster specifications (SeaBotix Inc., 2016)

Voltage	± 19.1 V DC $\pm$ 10%
Power	110 W Max. (depending upon RPM or Drag)
Max. Amperage	5.8 A (30 Second duration)
Weight	705 g
Peak thrust	2.9 kgf = 28.45 N

Appendix D

Path continuity

Geometric continuity is used to describe the smoothness of the path, which is usually denoted by G^n. Examples of paths with continuity of G^0, G^1 and G^2 are demonstrated in Figure D.1.

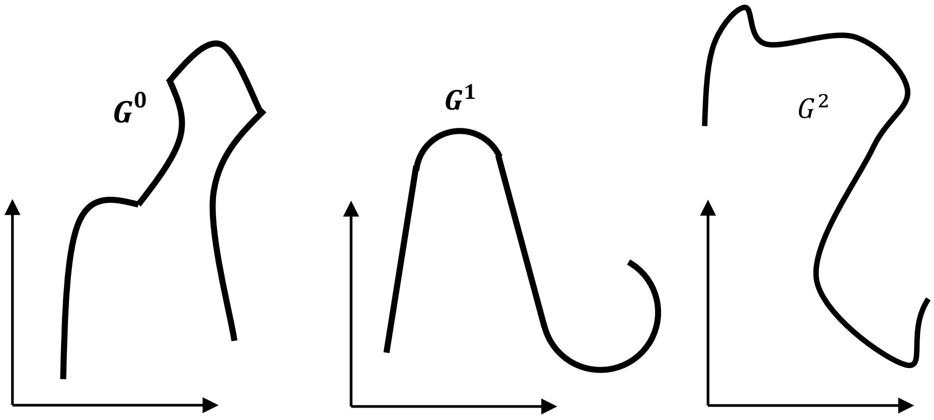

(a) (b) (c)

Figure D.1: Geometric continuity (based on Haugen, 2010). In (a), G^0 represents paths consisting of connected curves. And paths are G^1 if their unit tangential vector is continuous, as shown in (b). A G^1 path consists of several tangentially connected curves and/or lines, while G^2 paths have continuous curvature, in which case there is no instant change in the curvature, as the example given in (c).

Parametric continuity is represented by C^n. This is usually applied when the path is parameterized with a set of functions. If a curve has C^n

continuity, it means that the function of the path is n times differentiable, in other words, the path can be represented with a function of n-th order since the order of functions represents their differentiability (Barsky and DeRose, 1993). As in Equation (2.7), the order of the polynomials reflects the differentiability of the curve/path, which also defines the parametric continuity of C^k.

The lawn mower paths have good geometric smoothness/continuity of G^1; however, such a pattern is only a C^0 path from a parametric continuity point of view. Therefore, it is considered infeasible for the conventional fin-manoeuvred AUVs, and the path needs to be modified into curvature continuous ones. In Haugen's work (2010) as mentioned in Chapter 2, the lawn mower paths were constructed into feasible paths using clothoids. Three examples of lawn mower paths are demonstrated in Figure D.2.

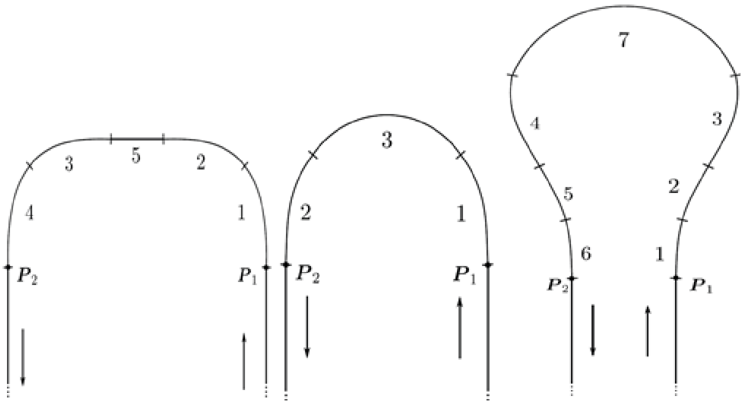

(a) (b) (c)

Figure D.2: Three path modifications for lawn mower paths with different curvatures using clothoids (based on Haugen, 2010). $\boldsymbol{P}_1, \boldsymbol{P}_2$ are the intersection points between lines and curves.

In Figure D.2, the U-turn section is modified in three ways using clothoids to connect the arc and the line, since the curvature of clothoids varies continuously. The one in Figure D.2 (a) applies Clothoids 1, 2, 3 and 4, achieving a gradual curvature change within the U-turn, and Section 5 is a straight line. This method is suitable when the distance between the parallel lines is sufficiently large. Otherwise, the other two methods are used. In Figure D.2 (b), the Clothoids 1 and 2 are connected to Arc 3, forming a complete turn. The method in Figure D.2 (c) is applied for very narrow distances between parallel lines by using Clothoids 1 to 6 and Arc 7. This is intuitive when placed in the context of an analogy with driving behaviour; the driver steers in the opposite direction first to manage a tight turn.

Appendix E

Publications